D.2.1.1 – Slope analysis report

PP1 LP-UNIURB

Document Control Sheet

Project number:	ITHR0200175
Project acronym	RESONANCE
Project Title	impRoving landslidE riSk preventiOn aNd mAnagement iN Coastal arEas
Start of the project	March 2024
Duration	30 months

Project activity	2.1 Slope analisys
Deliverable number & name	D.2.1.1 Slope analysis report
Type of deliverable	Report
Language	English
Work Package Number and Title	WP2 - Slope analysis and risk definition
Work Package Leader	PP3-GRADRI

Status	Final
Author(s)	Mirko Francioni, Mariagiulia Annibali Corona, Paolo Stocchi, Stefano Morelli, Simone Galeotti, Giulio Pappafico – **LP-UNIURB**; Igor Ružić, Josip Peranić, Martina Vivoda Prodan, Željko Arbanas – **PP3-GRADRI**.
Version	1

Index

1. Conero Regional Park

1.1. Introduction

The Monte Conero promontory (572 m a.s.l.) is located along the coastal sector of Ancona (Marche Region, Central Italy) and extends for approximately 15 km along the Adriatic coastline, between the city of Ancona and the village of Numana. This coastal stretch is characterised by steep sea cliffs, generally exceeding 100 m in elevation. The study area is illustrated in Figure 1.

Monte Conero constitutes one of the most important tourist destinations in Central Italy, attracting thousands of visitors from across Europe and beyond. However, due to the frequent occurrence of slope instability phenomena affecting several coastal sectors, some beaches are classified as high-risk areas for tourists.

Figure 1 - The Monte Conero promontory.

Given their significant economic value and tourist importance, these beaches are subject to continuous monitoring by local and regional authorities, particularly with regard to instability processes and coastline retreat and erosion dynamics.

From a geological standpoint, the coastal cliffs are carved into a variety of lithologies, including calcareous rocks, marls, clays, sandstones, and gypsum. The geological framework of the study area is shown in Figure 2. Structurally, Monte Conero is characterised by an open, NE-verging asymmetric anticline intersected by E–W oriented strike-slip faults (Cello & Coppola, 1989; Pierantoni et al., 2013). The northeastern limb exhibits steep dips (70–85°), whereas the southwestern limb is characterised by gentler inclinations of approximately 20°. Within this structural setting, both bedding planes and fracture systems exert a primary control on slope stability conditions.

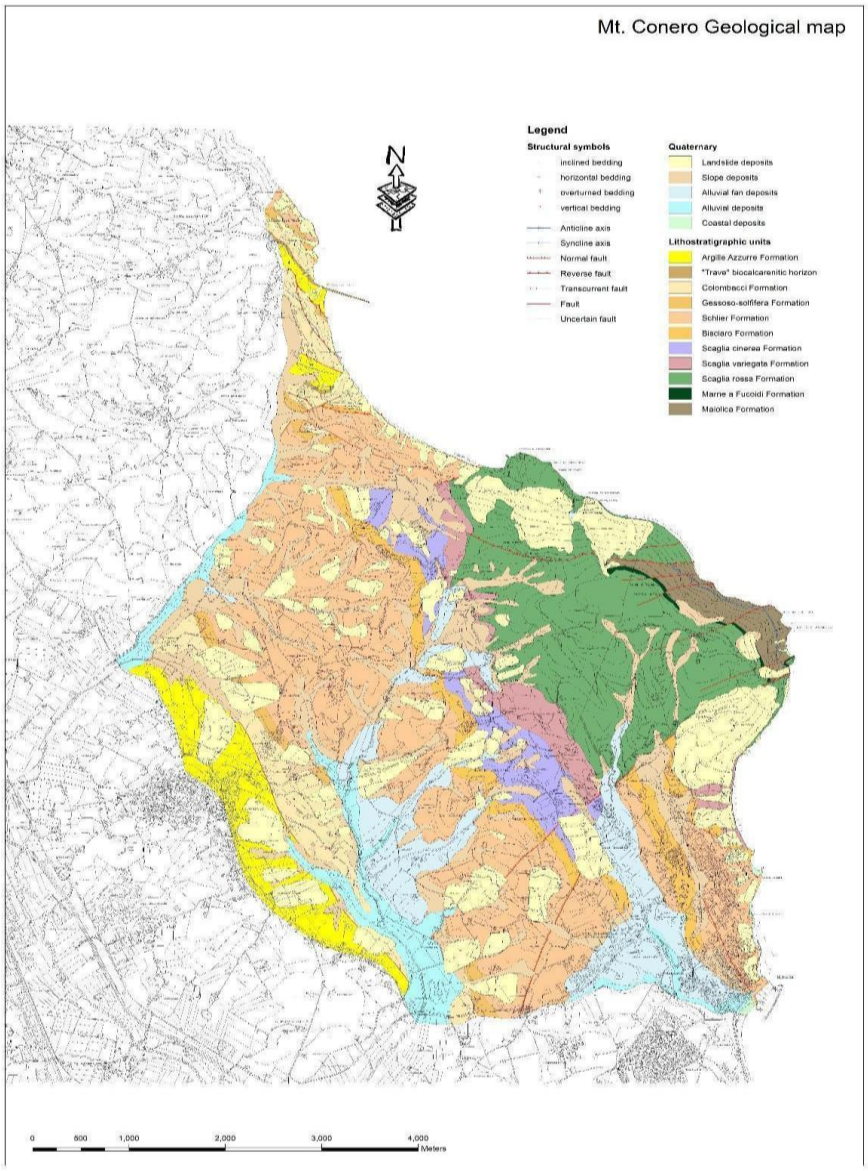

Figure 2 - Geological map of Monte Conero.

The investigation focused on two main sectors: the Mezzavalle area and the Piangrande cliff (Figure 3). Mezzavalle beach is considered one of the most hazardous areas within the Conero Regional Park, as slope failures occur frequently, often posing a threat to visitors. In this sector, the cliffs are particularly high and steep and are mainly composed of marls and marly limestones.

The Piangrande cliff, located a few kilometres south of Mezzavalle beach, is characterised by recurrent large-scale slope failures that have affected the Portonovo coastal zone since at least medieval times (Montanari et al., 2016). Unlike Mezzavalle, the dominant lithology in this sector consists of Eocene marly limestones belonging to the Scaglia Rossa Formation, which form the steep rocky escarpments.

Figure 3 - The Mezzavalle beach and the Piangrande promontory in the Conero Regional Park.

1.2. Existing data retrieval and new monitoring data acquisition

The available dataset for Monte Conero mainly consists of orthophotos and geological information, with no pre-existing data related to monitoring systems or geotechnical investigations. Nevertheless, orthophotos and LiDAR datasets proved fundamental for identifying and analysing past slope failures. The LiDAR dataset was acquired in 2012, while orthophotos span the period between 1978 and 2021. The 2012 LiDAR data were used to generate the Digital Elevation Model (DEM) and the thematic maps shown in Figures 4 and 5. These datasets provided the topographic and geomorphological basis for the subsequent field surveys and slope stability analyses.

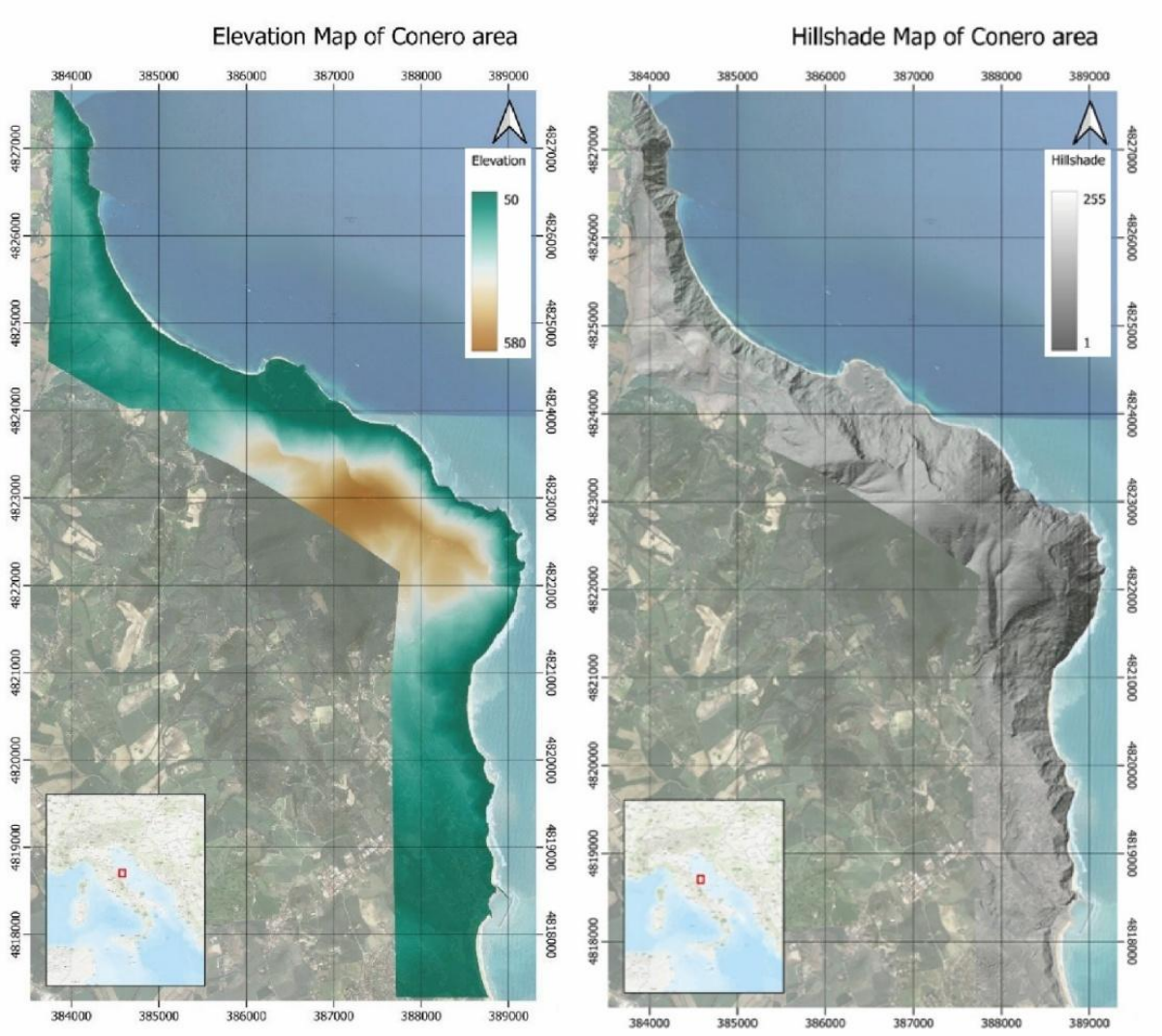

Figure 4 - DEM and hillshade maps of the Conero Regional Park.

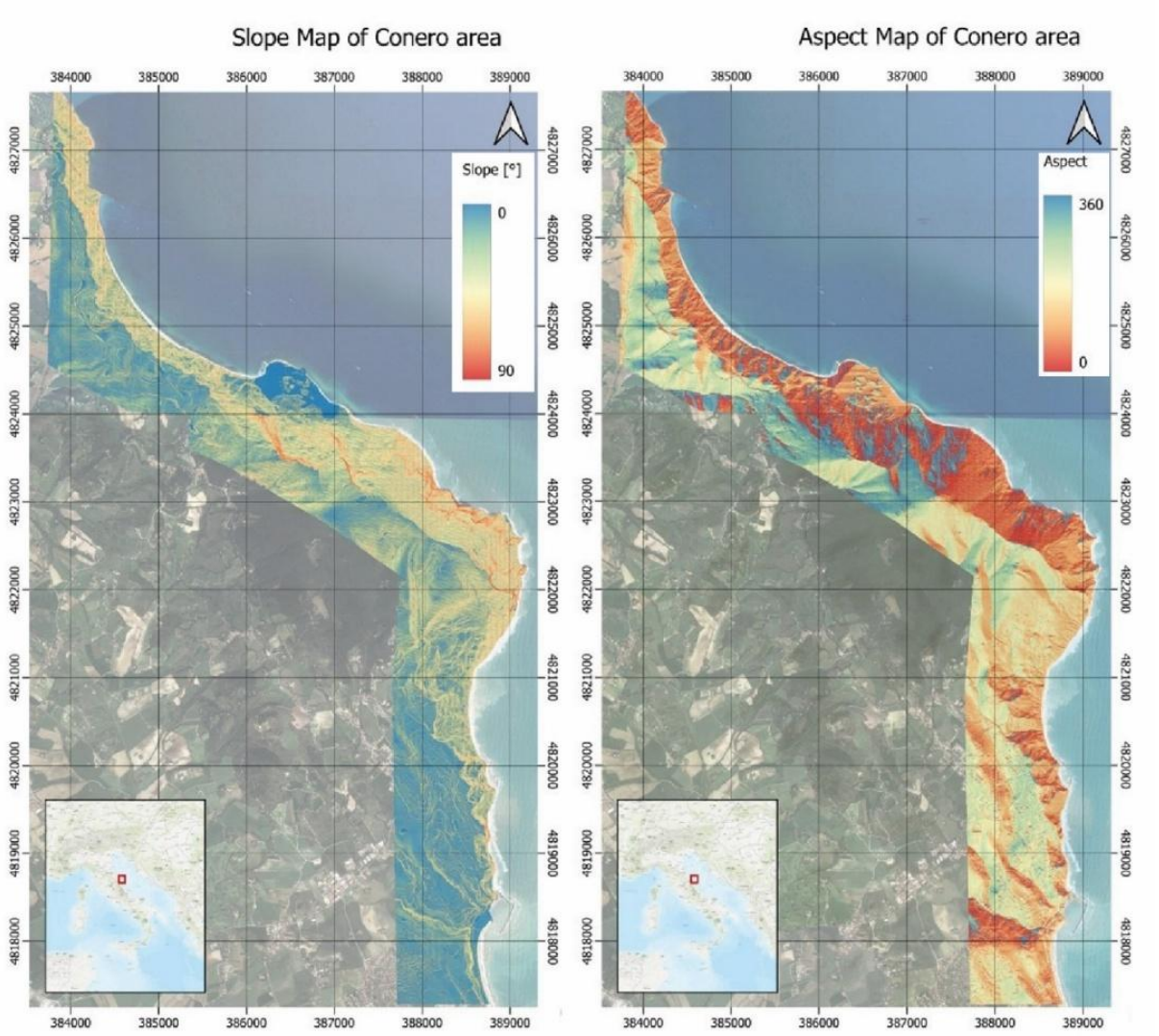

Figure 5 - Slope and aspect maps of the Conero Regional Park.

1.3. Field and remote sensing surveys – Piangrande area

Field-based geomorphological and geomechanical surveys were carried out to identify landforms related to past landslide activity and to characterise the geomechanical properties of the Piangrande rock mass.

Three representative survey sites within the Scaglia Rossa Formation were selected to investigate rock mass characteristics and local morphological conditions (Figure 6). Survey Area 1 (SA1, Poggio Quarry) is an abandoned quarry with well-exposed rock outcrops. Survey Area 2 (SA2, Riparo dello Speco) is located along the mid-slope of a southeast-facing cliff sector and corresponds to a cave recently identified in the study area. Survey Area 3 (SA3, Piangrande cliff) corresponds to the main coastal cliff sector investigated in this work and is characterised by pronounced structural complexity and active instability processes.

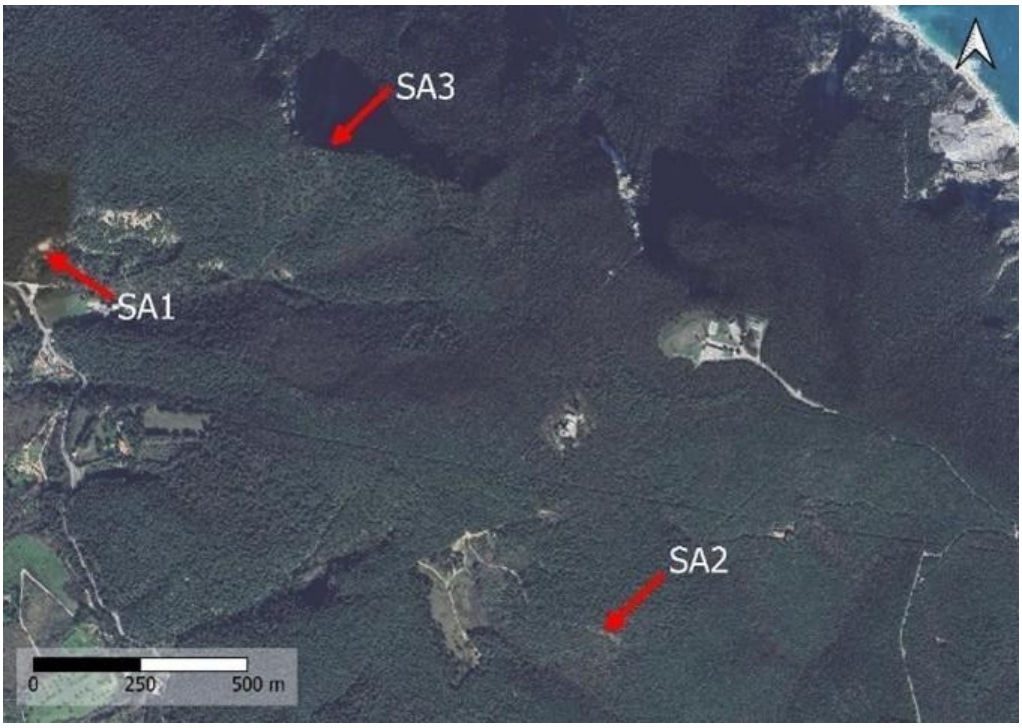

Figure 6 - Geographical location of geomechanical surveys.

Due to the inaccessibility of the cliff face, conventional geomechanical investigations were carried out only in the accessible sectors SA1 and SA2, following the recommendations of the International Society for Rock Mechanics (ISRM, 1978). These surveys included lithological descriptions and systematic scanline measurements of discontinuity parameters, including orientation, spacing, persistence, aperture, roughness, and infilling.

At SA3, geomechanical characterisation was performed exclusively through remote sensing techniques because the cliff face was inaccessible. In this area, both UAV LiDAR and UAV photogrammetric surveys were carried out. The LiDAR survey collected 1,827 acquisition frames and allowed the generation of a DTM with a resolution of 0.5 × 0.5 m. The photogrammetric survey consisted of 715 images processed in Agisoft Metashape through a Structure-from-Motion workflow. The resulting model, used for structural mapping, consists of 3,075,528 faces and 161,657,934 points.

The UAV photogrammetric surveys at SA1 and SA3 were performed using a DJI Mavic 3E equipped with a 4/3 CMOS sensor with 20 MP effective resolution and an 84° field of view. The camera aperture ranges from f/2.8 to f/11, the focus range is from 1 m to infinity, and the ISO sensitivity ranges from 100 to 6400. Surveys were carried out in manual mode with approximately 80% frontal and lateral overlap between consecutive images. The acquired images were processed in Agisoft Metashape using a Structure-from-Motion workflow,

allowing the generation of point clouds and three-dimensional models suitable for structural analysis.

For the quarry site (SA1), UAV surveys were performed using the same platform and acquisition protocol adopted for the Piangrande cliff. At SA2, the conventional geomechanical survey was integrated with a LiDAR survey performed using an iPad Pro equipped with an integrated LiDAR sensor, capable of measuring distances up to approximately 5 m. This system provides an estimated accuracy of about 2 cm for a single pass and proved effective for the acquisition of large surfaces and wall geometries, as in the present case. The cave was scanned through multiple passes starting from the entrance and progressively covering the entire internal surface.

The resulting 3D models from the three sites are shown in Figure 7. For SA1 and SA3, the models were derived from UAV photogrammetry, whereas for SA2 the model was derived from LiDAR acquisition with an iPad Pro.

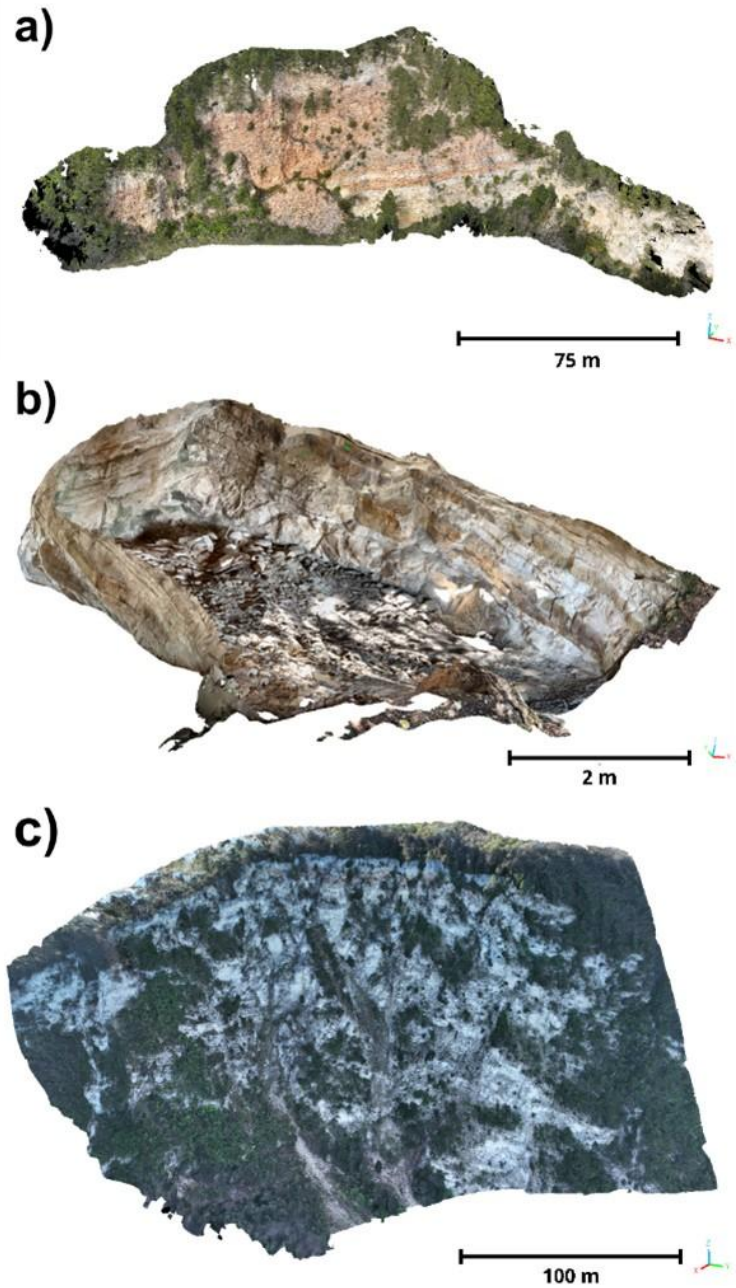

Figure 7 - Three-dimensional models used for structural and geomorphological analyses: (a) UAV-based photogrammetric model of the Cava Poggio quarry; (b) LiDAR-derived 3D model of the Riparo dello Speco cave acquired with an iPad Pro; (c) UAV-based photogrammetric model of the Piangrande coastal cliff.

Discontinuity orientations were extracted from these models using the Plane and Trace tools within the Compass plugin of CloudCompare, allowing integration between remotely acquired data and field measurements (Figure 8).

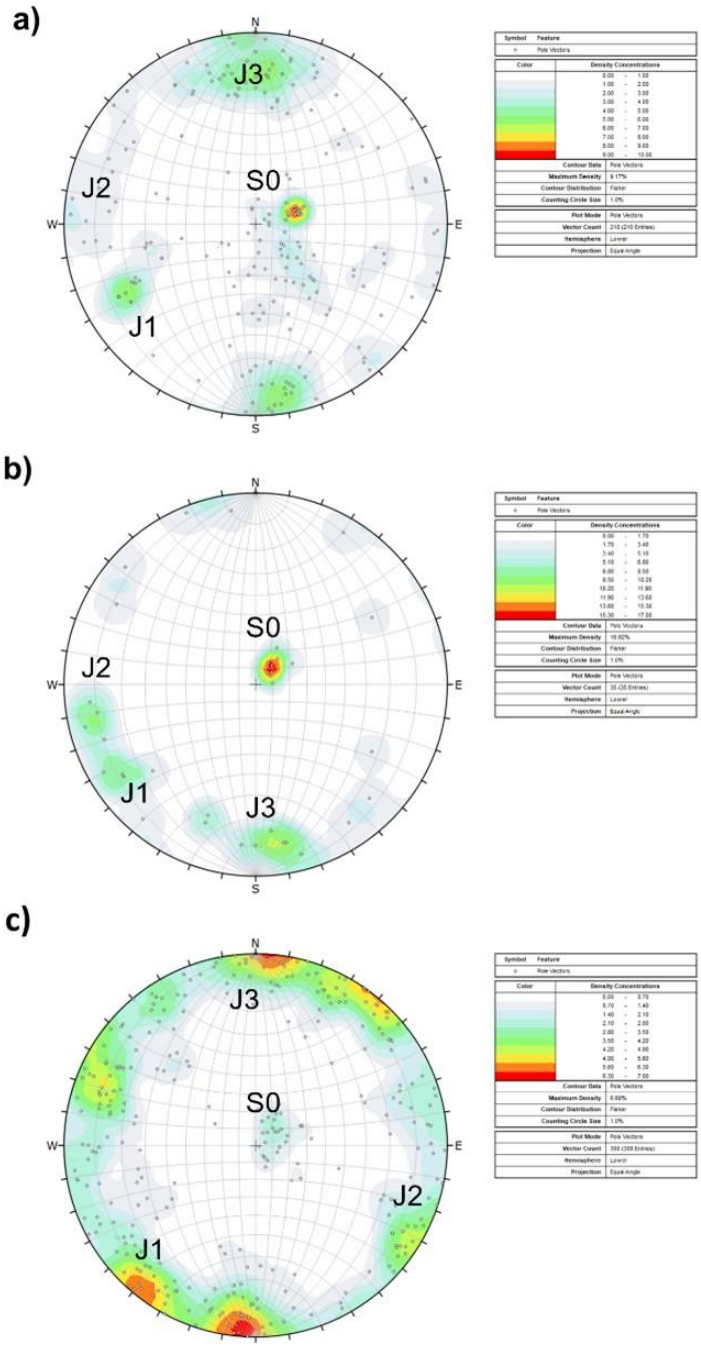

Figure 8 - Lower-hemisphere, equal-angle stereographic projections of discontinuity poles measured at (a) SA1, (b) SA2 and (c) SA3.

The integration of field surveys and remote sensing techniques enabled the acquisition of high-quality structural and geomorphological data in areas that are otherwise difficult or unsafe to access.

Structural analysis revealed the presence of a gently dipping bedding plane (S0), associated with multiple steeply dipping joint sets (J1–J3), defining a structurally complex rock mass (Table 1).

Table 1 - Mean orientation and selected geomechanical properties of the principal discontinuity sets identified in the Monte Conero coastal cliff. Pers. = persistence; Spac. = spacing; Aper. = aperture; Fill. = infilling material; Weath. = weathering degree; Rough. = surface roughness; D = dry conditions; NC = non-cohesive; SW = slightly weathered; MW = moderately weathered; HW = highly weathered; R = rough; S = smooth.

Set	Type	Dip / Dip dir. (°)	Spac. (m)	Pers. (m)	Aper. (mm)	Weath.	Rough.	Fill.	Flow
S0	Bed	18 / 235	0.1	–	5.0	MW	R	NC	D
J1	J	88 / 050	0.2	0.6	1.2	SW	R	NC	D
J2	J	87 / 116	0.2	0.3	2.5	MW	S	NC	D
J3	J	88 / 003	0.1	2.1	3.0	HW	R	NC	D

This discontinuity pattern is consistent with previous studies in the Conero coastal sector (Mammoliti et al., 2022; Fullin et al., 2023), reflecting a regionally persistent structural framework locally influenced by deformation and weathering processes. Preliminary geomechanical assessment indicates that the rock mass quality ranges from moderate to good. On the basis of surface geomechanical conditions alone, instability appears more likely to occur through localized detachment of individual rock blocks than through widespread large-scale failures.

The geomechanical characterisation of the Piangrande cliff was further refined through the application of the Slope Mass Rating (SMR) classification. The SMR analysis was carried out considering two representative slope orientations (Sector 1: 72/005 and Sector 2: 72/064). The results indicate comparable conditions for both sectors, with rock mass quality ranging from good (Class II) to moderate (Class III). Most discontinuity sets (S0, J1 and J2) show SMR values higher than 60, corresponding to stable conditions and suggesting a limited instability potential mainly associated with the detachment of isolated rock blocks. In contrast, the J3 discontinuity set shows lower SMR values (54–58), corresponding to Class III conditions and indicating a higher susceptibility to structurally controlled failure mechanisms.

Table 2 - SMR classification of the main discontinuity sets at the Piangrande Cliff for planar sliding and toppling conditions. The table reports SMR values, corresponding stability classes, qualitative stability conditions, and associated failure mechanisms. Results are identical for both analysed slope sectors.

Failure type	Discontinuity set	SMR value	Class	Stability condition	Failure mechanism
Planar sliding	S0	66.8	II	Good – stable	Failure of individual blocks
Planar sliding	J1	73.2	II	Good – stable	Failure of individual blocks
Planar sliding	J2	66.8	II	Good – stable	Failure of individual blocks
Planar sliding	J3	58.0	III	Moderate – partially stable	Involvement of planes, joints and wedges
Toppling	S0	70.4	II	Good – stable	Failure of individual blocks
Toppling	J1	69.4	II	Good – stable	Failure of individual blocks
Toppling	J2	63.1	II	Good – stable	Failure of individual blocks
Toppling	J3	54.3	III	Moderate – partially stable	Involvement of planes, joints and wedges

1.4. Conventional and numerical slope analyses of Piangrande cliff

Since the SMR classification provides only a preliminary assessment based on discontinuity orientation and rock mass quality, a kinematic analysis was subsequently carried out to evaluate the geometrical feasibility of the main failure mechanisms.
Kinematic analysis was performed using stereographic projection techniques implemented in DIPS, following the Markland approach and assuming a friction angle of 35°. The analysis considered the same representative slope orientations adopted for the SMR classification and evaluated the potential occurrence of planar sliding, wedge sliding, and toppling mechanisms (Table 3; Figure 9).

Table 3 - Summary of kinematic analysis results.

Failure mechanism	Dataset / Discontinuity set	72/005 (%)	72/064 (%)	Interpretation
Planar sliding	All data	1.95	2.92	Very low
	All data (no lateral limits)	3.25	5.52	Low
Wedge sliding	All intersections	0.00–1.31	0.00–3.73	Negligible to low
	J1–J3 intersection	4.06	6.04	Local condition
Direct toppling	All data	4.87	3.57	Low
	S0	20.83	–	Local condition
Flexural toppling	All data	11.36	8.77	Moderate
	J1	45.61	–	High
	J3	8.20	18.03	Moderate

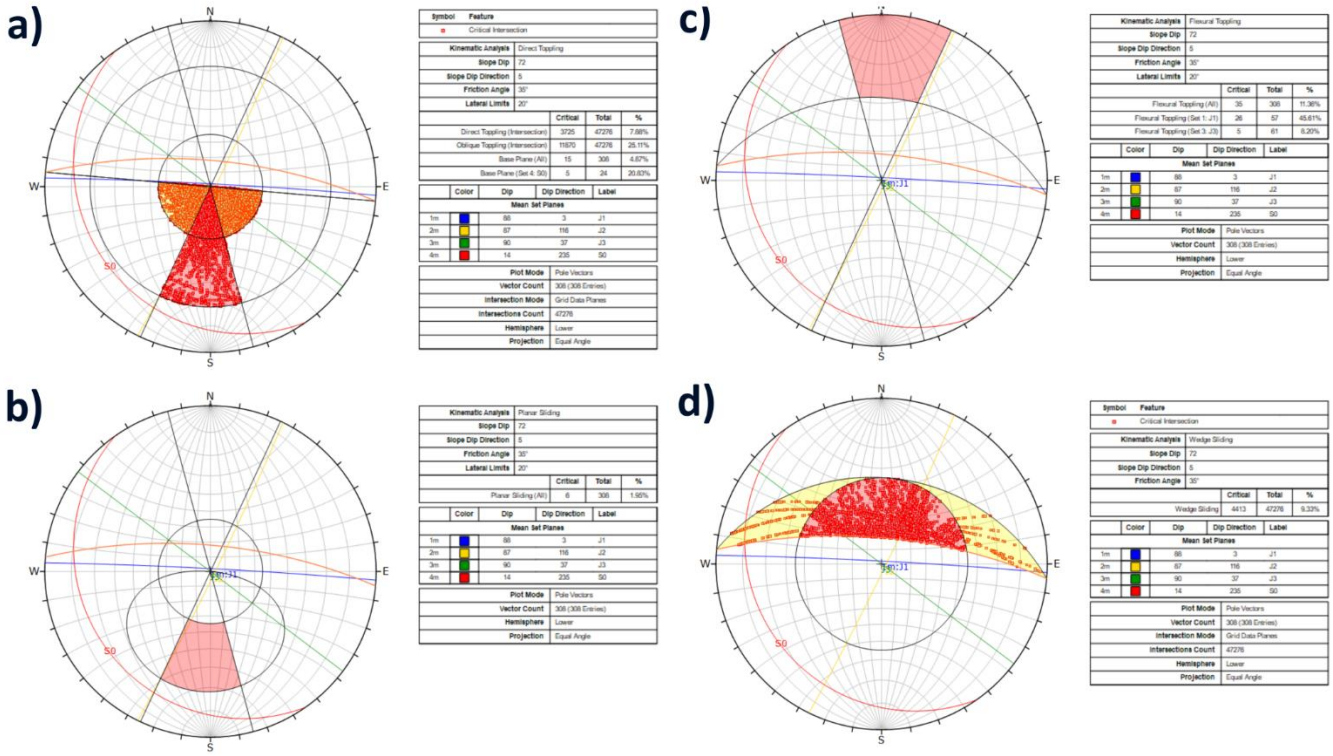

Figure 9 - Kinematic analysis results obtained using DIPS for the Piangrande Cliff assuming a friction angle of 35°. Stereographic projections show the kinematic conditions for (a) direct toppling, (b) planar sliding, (c) flexural

toppling, and (d) wedge sliding. The diagrams refer to the slope orientation 72/005 and are shown as a representative example of the kinematic analysis performed for the study area.

The results indicate that planar sliding is negligible, as shown by very low critical percentages. Wedge sliding also exhibits limited susceptibility, with only a few localized discontinuity intersections potentially leading to instability conditions. In contrast, flexural toppling emerges as the most significant potential failure mechanism, showing moderate critical percentages and a predominant contribution from the J1 discontinuity set. These results are generally consistent with the SMR classification, although they provide a more detailed representation of the role of flexural toppling.

Because kinematic analysis only assesses the geometric compatibility of failure mechanisms, three-dimensional limit equilibrium analyses were then performed to evaluate the actual stability conditions of blocks defined by the cliff geometry and discontinuity network. For SA3, both LiDAR-derived and photogrammetry-derived three-dimensional models were tested in the stability analyses in order to evaluate the influence of acquisition geometry on block detection and computed FoS values.

Three-dimensional limit equilibrium analyses were performed using RocSlope3 to evaluate the stability conditions of the Piangrande cliff and to identify potentially unstable rock blocks. Two three-dimensional slope models were generated from the UAV-derived datasets, namely the LiDAR-derived model and the photogrammetry-derived model. The models were initially processed through a MATLAB-based workflow and subsequently refined in Rhinoceros using the Griddle plugin before being imported into RocSlope3.

Due to computational constraints, only the two main discontinuity sets identified during the structural analysis were included in the simulations, both assigned a spacing value of 2 m. The RocSlope3 algorithm identifies rock blocks generated by the intersection between the slope surface and discontinuity planes and evaluates their potential mobility by computing the Factor of Safety (FoS) through three-dimensional limit equilibrium calculations. Mechanical parameters were assigned based on both field observations and literature values (Mandaglio et al., 2024). The modelling procedure identified a total of 14,350 potential blocks. Most of these blocks show stable conditions, with 321 blocks characterised by FoS values between 3 and 4. However, three blocks exhibit FoS values lower than 1, indicating localized instability (Figure 10).

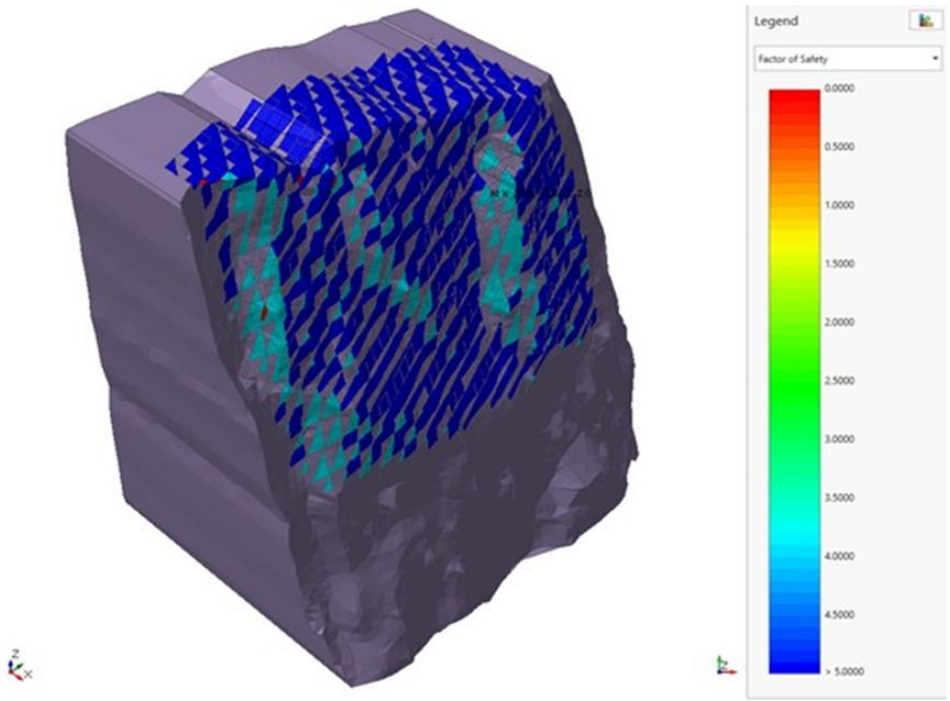

Figure 10 - Results of the RocSlope3 three-dimensional limit equilibrium analysis. Most detected blocks are stable, whereas three blocks show FoS values lower than 1.

These unstable blocks are located in steep or locally overhanging sectors of the slope, which were more accurately reconstructed through the photogrammetric survey due to the oblique and frontal acquisition geometry adopted during UAV data collection.

The results of the limit equilibrium and numerical analyses vary depending on the three-dimensional model adopted. When the LiDAR-derived model is used, the slope appears globally stable and only small potentially unstable blocks can be identified. In contrast, the photogrammetry-derived model highlights a higher instability potential, including blocks located in the steepest and locally overhanging portions of the cliff. This difference is mainly related to the acquisition geometry of the two surveys. The LiDAR survey, acquired mainly in nadiral view, provided a reliable reconstruction of the general slope geometry but was less effective in capturing overhanging sectors. Conversely, the photogrammetric survey, thanks to the combined nadiral, oblique, and frontal image acquisition, allowed a more detailed reconstruction of the sub-vertical rock face and locally overhanging sections. These sectors play a key role in block kinematics and significantly influence the stability analyses, leading to lower FoS values and a clearer identification of potentially unstable blocks.

To further investigate block behaviour and validate the results obtained from the limit equilibrium approach, additional numerical simulations were carried out using the discontinuum code 3DEC. To reduce computational demand, the analyses were conducted along two-dimensional sections extracted from the three-dimensional models through a MATLAB-based workflow. These sections were subsequently refined in Rhinoceros and imported into the 3DEC environment. The mechanical behaviour of the rock mass was simulated using a Mohr–Coulomb constitutive model, while the orientation of the discontinuity sets was defined according to the results obtained from the kinematic and geomechanical analyses.

The simulations based on the photogrammetry-derived geometry highlight the presence of unstable small rock blocks located within steep or overhanging portions of the slope (Figure

11). The numerical results are consistent with those obtained from the limit equilibrium analyses, confirming that instability is mainly associated with localized detachment phenomena affecting small blocks in the steepest sectors of the cliff.

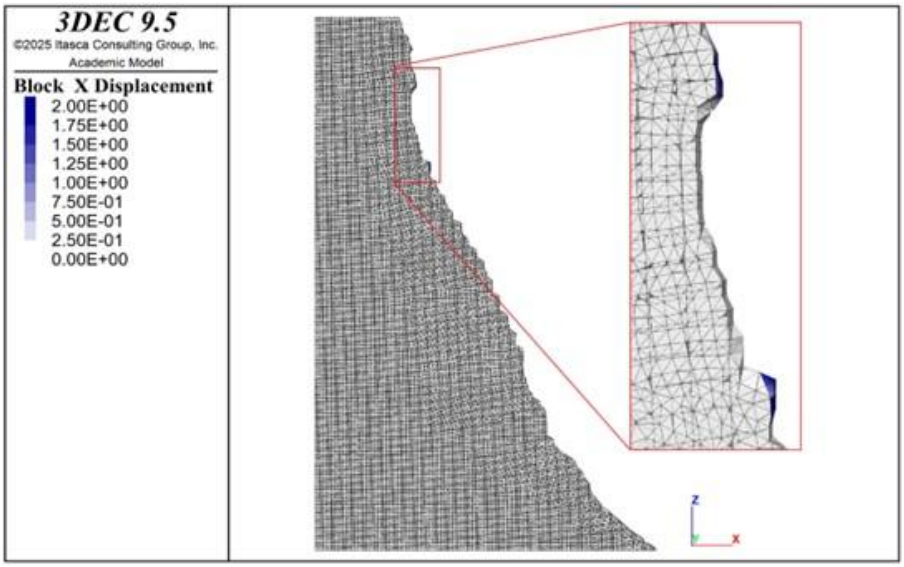

Figure 11 - 3DEC numerical simulation highlighting instability of small blocks in overhanging sectors.

1.5. Slope behaviour and method limitations

The integrated analysis carried out for the Piangrande cliff indicates that slope stability is primarily controlled by the structural configuration of the rock mass and by the geometric relationships between discontinuity sets and slope orientation. The identified framework, characterised by a gently dipping bedding plane (S0) and multiple sub-vertical joint sets (J1–J3), defines a structurally complex slope predisposed to kinematically controlled instability mechanisms.

The SMR classification indicates overall good to moderate rock mass conditions and suggests a limited instability potential mainly associated with the detachment of isolated blocks. The kinematic analysis, however, provides a more refined interpretation, showing that planar and wedge sliding are negligible, whereas flexural toppling represents the most relevant potential failure mechanism. This difference highlights an important limitation of the SMR approach, which is based on averaged discontinuity orientations and does not explicitly account for flexural toppling, while the kinematic analysis considers the full set of measured discontinuities.

A further distinction emerges when comparing the results of limit equilibrium and numerical analyses performed on LiDAR-derived and photogrammetry-derived models. The LiDAR-based model indicates globally stable conditions, whereas the photogrammetric model reveals a higher instability potential in steep and locally overhanging sectors. This discrepancy is mainly related to the acquisition geometry of the two datasets. The LiDAR survey, predominantly acquired in nadiral configuration, provides a reliable reconstruction of the general slope morphology but is less effective in capturing overhanging geometries. In contrast, the photogrammetric survey, integrating nadiral, oblique, and frontal acquisitions, allows a more accurate reconstruction of sub-vertical and overhanging rock faces, which play a key role in block kinematics and slope instability.

The combined interpretation of geomorphological evidence and modelling results suggests that two main types of failure mechanisms may occur at the Piangrande cliff. The first is associated with the detachment of individual rock blocks from steep or overhanging sectors, as identified by limit equilibrium and numerical analyses. The second involves progressive fracture propagation within the rock mass, potentially leading to larger-scale slope failures.
This second mechanism is supported by geophysical investigations carried out by the project partner (CNR of Lecce). In particular, the 2D electrical resistivity survey performed at the top of the cliff (Figure 12) allowed the identification of subsurface discontinuities not directly observable at the surface. These features are interpreted as fracture zones propagating at depth and potentially contributing to the progressive isolation of larger rock volumes.
The conceptual model derived from the integration of geophysical and geological evidence (Figure 13) shows how these deep-seated discontinuities may interact with the existing structural framework, potentially leading to failure mechanisms involving much larger rock masses than those identified by numerical modelling alone. This interpretation is consistent with field geomorphological observations, which indicate the occurrence of larger-scale instability processes affecting the slope.
The conceptual model derived from the integration of geophysical and geological evidence (Figure 13) shows how these deep-seated discontinuities may interact with the existing structural framework, potentially leading to failure mechanisms involving much larger rock masses than those identified by numerical modelling alone. This interpretation is consistent with field geomorphological observations, which indicate the occurrence of larger-scale instability processes affecting the slope.

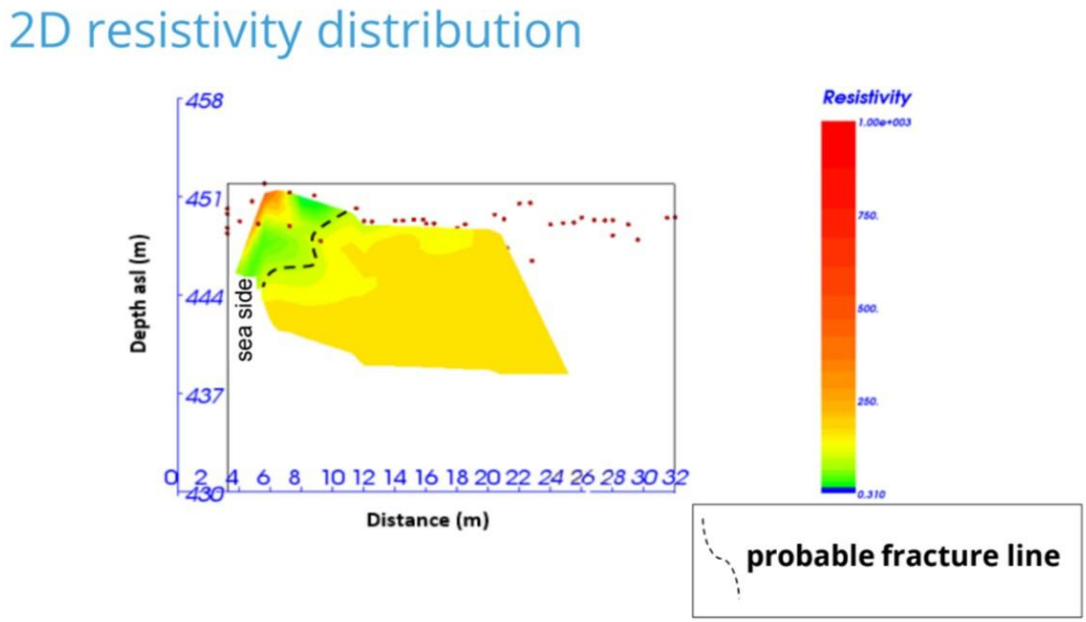

Figure 12 - 2D electrical resistivity tomography (ERT) section acquired at the top of the Piangrande cliff. The distribution of resistivity values highlights zones of lower resistivity interpreted as fractured or more weathered sectors. The dashed line indicates a probable subsurface fracture zone, suggesting the presence of discontinuities not directly observable at the surface.

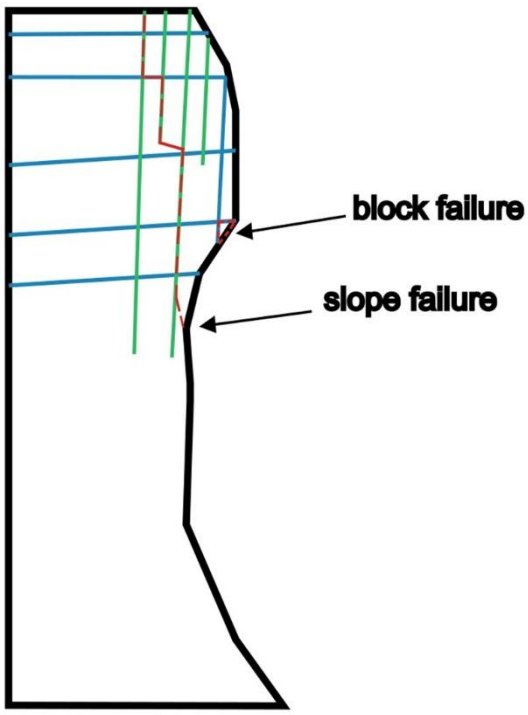

Figure 13 - Conceptual geological model of the Piangrande cliff showing the main discontinuity sets and the inferred deep-seated fracture zones identified through geophysical investigations. The scheme illustrates two potential failure mechanisms: (i) localized block failure associated with overhanging geometry, and (ii) larger-scale slope failure related to fracture propagation and progressive rock mass detachment.

While the detachment of small blocks is effectively captured by the adopted modelling approaches, progressive failure mechanisms are not reproduced by either limit equilibrium or discontinuum numerical simulations. This reflects the intrinsic difficulty of modelling fracture propagation processes, which require more advanced hybrid approaches (e.g. FEM–DEM) and, above all, a strong geological and geomorphological interpretation.
Overall, the results show that no single method is sufficient to fully describe slope behaviour in structurally complex coastal cliffs. A reliable stability assessment must therefore be based on the integration of geomechanical classification, kinematic analysis, numerical modelling, geophysical investigations, and detailed geological interpretation. Only through this combined approach is it possible to identify both localized instabilities and larger-scale failure processes, while also properly understanding the strengths and limitations of each method.

1.6. Field and remote sensing surveys – Mezzavalle area

In the Mezzavalle area, the analysis primarily focused on coastline evolution and cliff retreat processes.
Fieldwork was performed to collect and map information regarding geological and mechanical characteristics of the exposed lithotypes.
Rock mass quality was expressed through the Geological Strength Index (GSI) value and Uniaxial Compressive Strength (UCS).
A revised geological-geomorphological setting of the study area was generated based on the field survey findings (Figure 14). The Portonovo sector is characterised by the Schlier Fm. mostly covered by landslides deposits. The height of the cliffs in this sector span from few

meters to a maximum of 30-40 m. Here the cliff top retreat is mainly determined by landslides in the upper portion of the slope, with vertical or sub-vertical slope faces corresponding to the crown of the landslides (Figure 15a).

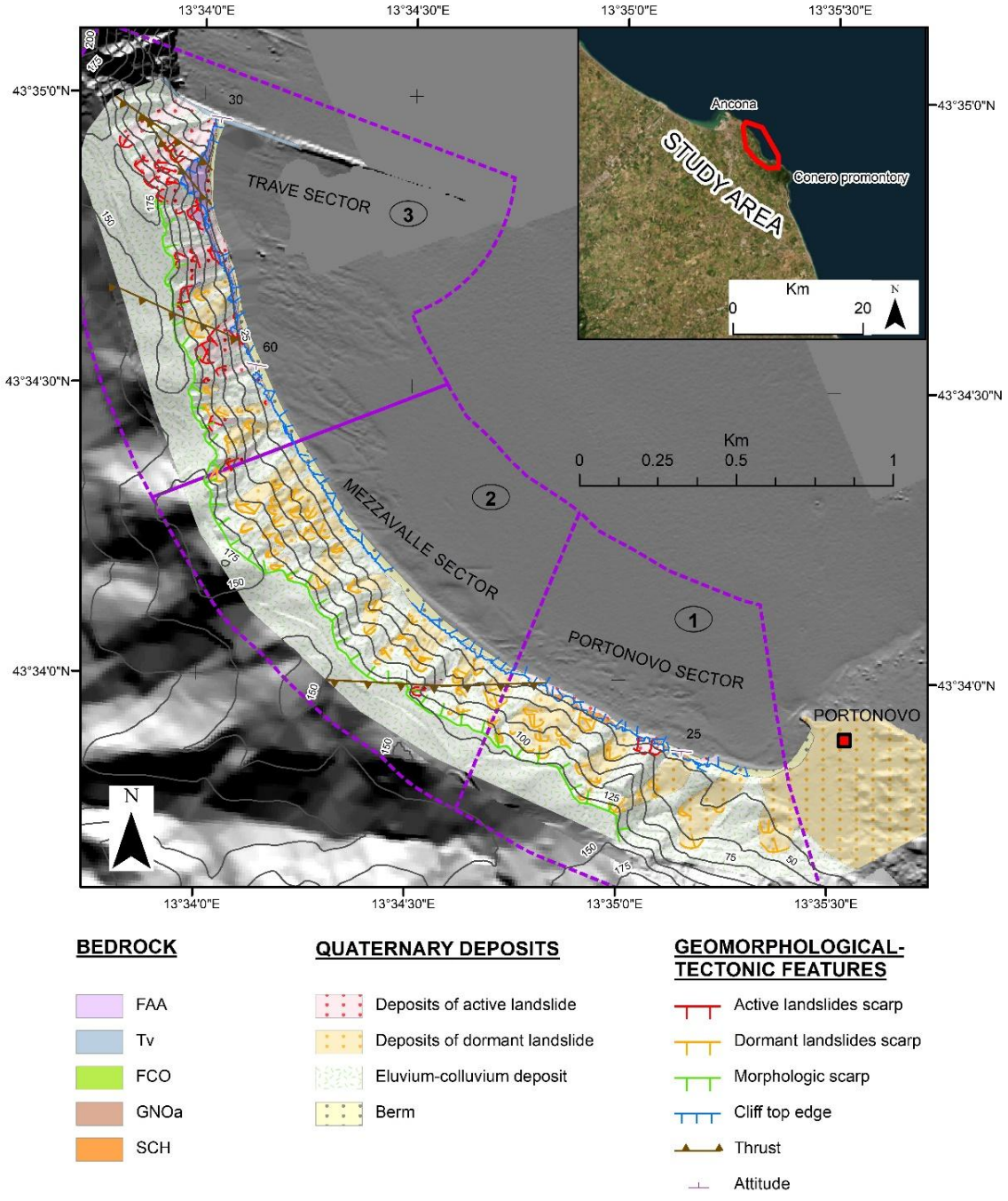

Figure 14 - Geological-geomorphological setting of the study area and "Sectors": 1) Portonovo; 2) Mezzavalle; 3) Trave. Bedrock legend: SCH (Schlier Fm., Lower Miocene-Upper Miocene), GNOa (Sapigno Fm. Upper Miocene), FCO (Colombacci Fm., Upper Miocene), Tv (Trave horizon, Lower Pliocene), FAA (Argille Azzurre Fm., Lower Pliocene-Lower Pleistocene).

The Mezzavalle sector is principally composed by landslide deposit (Figure 15b), with the bedrock outcropping only in the upper and steepest part of the slopes (representing landslides scars). The Trave sector presents the higher numbers of active landslides of different types

(rock falls, block toppling, earth flow and complex landslides). An important feature that characterises this sector is the high fracturing degree of the rock mass (Figure 15c), especially in proximity of the thrusts outcropping in this sector.

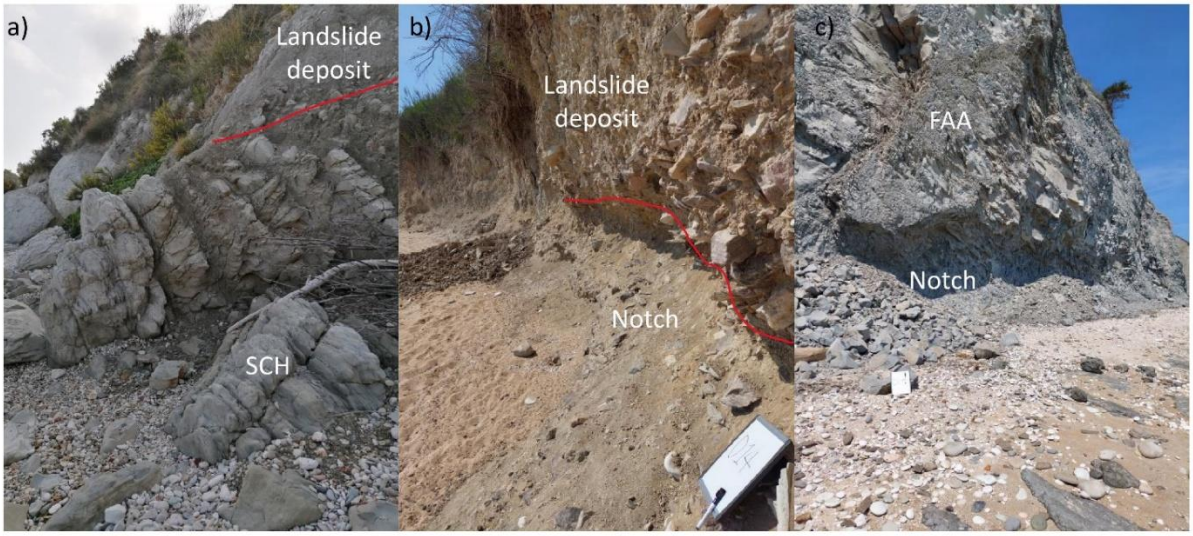

Figure 15 - Pictures portraying the different configurations of the cliff base. a) Portonovo sector b) Mezzavalle sector c) Trave sector.

The UCS values gathered through pocket penetrometer and Schmidt hammer are reported in Table 4. Because weak rock masses consist of alternating layers of marls and layers of calcareous marls, an average UCS value was computed across various levels in order to obtain a single representative value for each site

Table 4 - Range of GSI and UCS values for the 3 sectors according to different transects.

SECTOR	TRANSECTS	GSI	UCS (MPa)
PORTONOVO	1-79	50	35
MEZZAVALLE	80-184	0	5
	185-215	0	1
TRAVE	216-227	45	30
	228-265	35	25
	266-276	25	20
	277-290	35	25
	291-310	45	30

Regarding the remote sensing survey and analysis, a multitemporal comparison was conducted between LiDAR datasets acquired in 2012 (airborne LiDAR) and 2024 (UAV-based LiDAR) to quantify geomorphological changes affecting the coastal slope. The 2012 dataset was provided by the Marche Region, while the 2024 survey was performed using a DJI Matrice 350 equipped with a Zenmuse II LiDAR sensor.
The comparison highlights a marked retreat of the coastal cliff, particularly in the sector north of Mezzavalle beach. Differences between the two DEMs indicate a coastline retreat of approximately 10 m over a 12-year period (Figure 16).

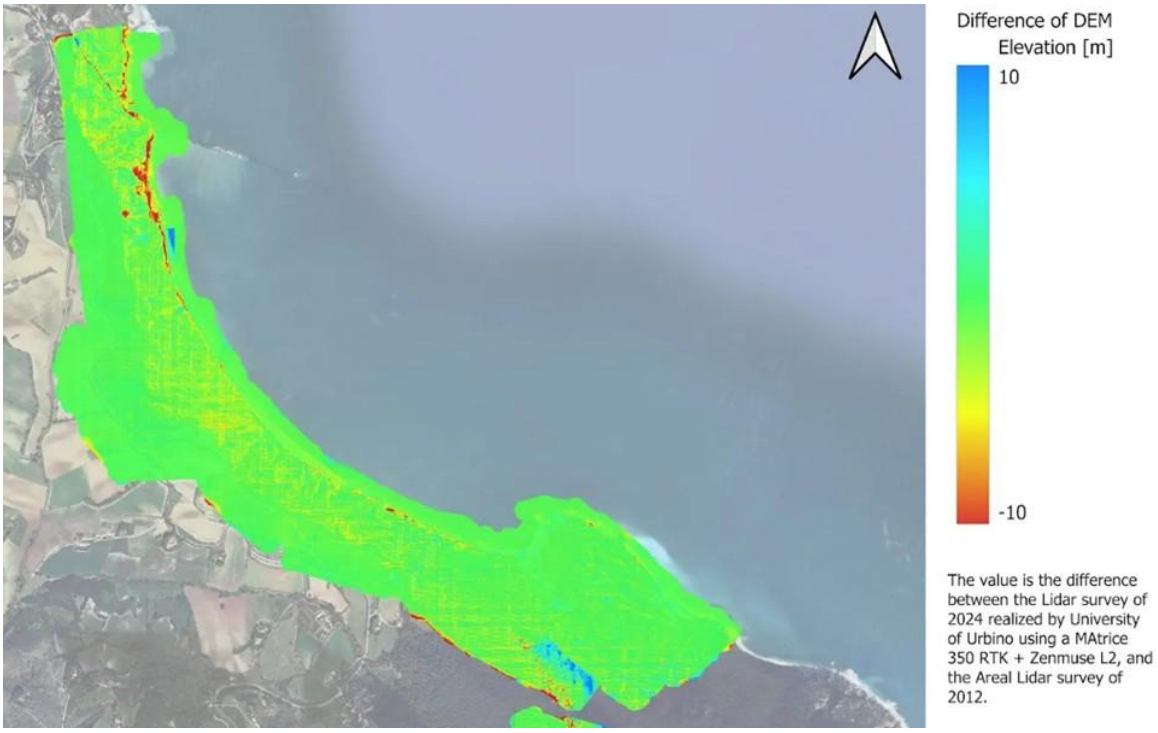

Figure 16 - Elevation changes detected from the comparison between the 2012 and 2024 LiDAR-derived DEMs, highlighting shoreline retreat along the Mezzavalle area.

1.7. Conventional and numerical slope analyses of Mezzavalle area

Two-dimensional limit equilibrium analyses were carried out along three representative topographic sections extracted from the Mezzavalle coastal slope. The location of the sections is shown in Figure 17.

Figure 17 - Location of the three analysed topographic sections within the Mezzavalle area. The sections were selected to capture the main variations in slope geometry and near-surface conditions along the analysed coastal sector.

For each section, two modelling configurations were considered: a conventional slope geometry and a modified geometry including a superficial buffer representing the effects of marine erosion and weathering processes. The analyses were performed using Slide2 (RocScience), which evaluates slope stability by comparing resisting and driving forces acting along potential failure surfaces. The software automatically searches for critical slip surfaces

within the defined slope geometry and stratigraphy and computes the corresponding Factor of Safety (FoS) as the ratio between available shear strength and mobilized shear stress.
The geotechnical parameters assigned to the different units were derived from literature sources for the Conero area and from field observations carried out during the surveys.
The results of the analyses (Figure 18) illustrate the three investigated profiles without the weathering and marine erosion buffer (a, c, e) and with the inclusion of the buffer (b, d, f). All simulations indicate limit equilibrium conditions in several portions of the slope, with FoS values generally ranging between 1.04 and 1.23 depending on the analysed section and modelling scenario.
A key outcome of the analysis is the significant influence of the weathering buffer on slope behaviour. In the models without weathering (a, c, e), failure surfaces are characterised by deeper, circular slip mechanisms. In contrast, in the models including weathering effects (b, d, f), failure surfaces are shallower and more superficial, reflecting processes associated with material degradation and coastal erosion.
These results are consistent with both the multitemporal LiDAR analysis and field observations, which indicate that slope instability in the Mezzavalle area is predominantly controlled by surface processes rather than deep-seated mechanisms.

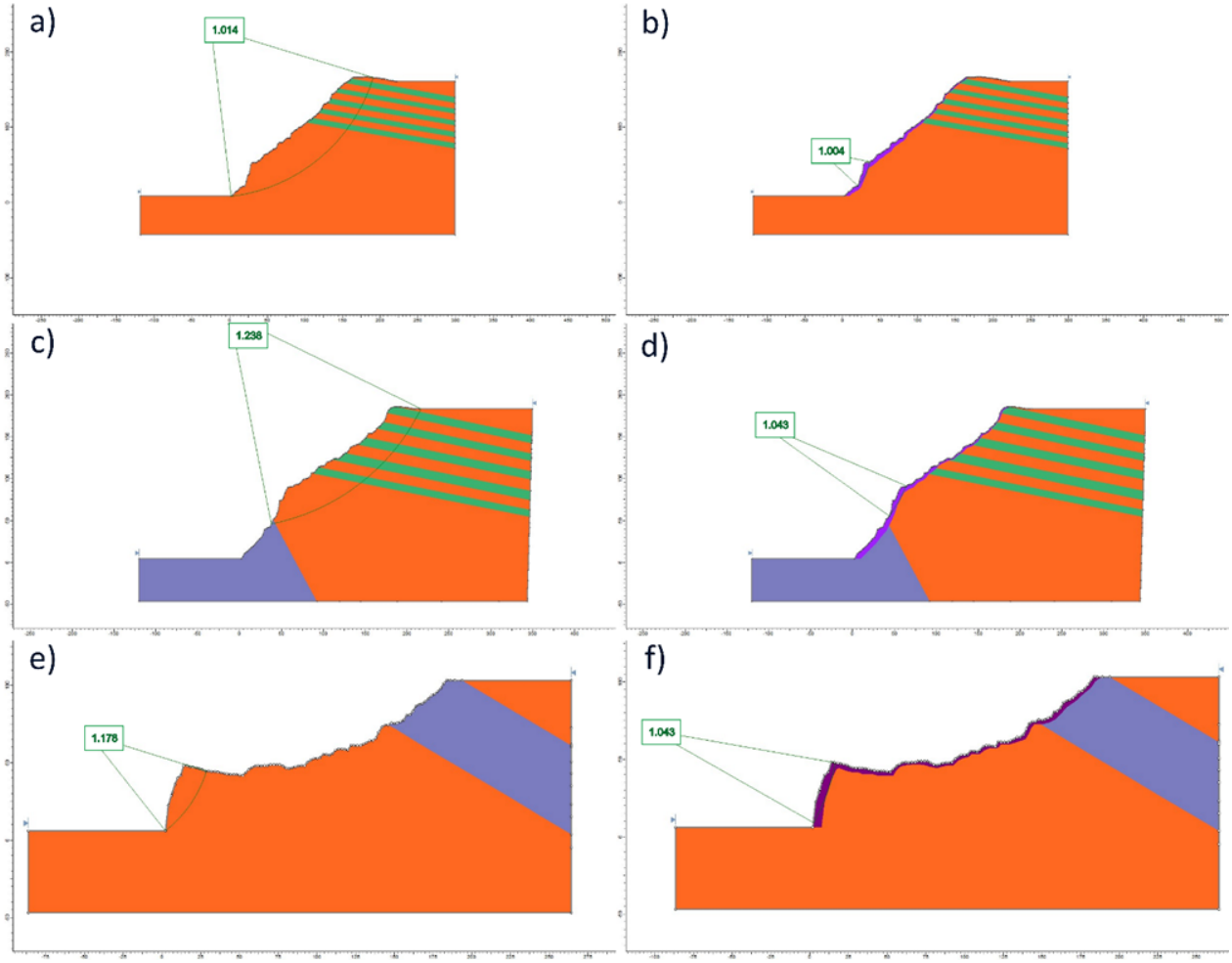

Figure 18 - Two-dimensional limit equilibrium analyses along three representative sections, with and without weathering and marine erosion effects.

2. Roca Vecchia Coastal Cliff

2.1. Introduction

The Roca Vecchia coastal cliff is located in the central sector of the Salento Peninsula, along the Adriatic coast of the Province of Lecce, in southern Italy (Figure 19).
Roca Vecchia represents one of the most significant coastal sites in the Salento region because of its high historical, archaeological, geomorphological, and touristic importance. This relevance is linked to the long-term occupation of the area since the Bronze Age, its role within Adriatic and Aegean exchange networks, the presence of the Grotta della Poesia, and the preservation of a coastal landscape of remarkable environmental and cultural interest.
From a geomorphological point of view, the coastline is characterised by a predominantly tabular morphology with gentle undulations, rarely exceeding a few tens of metres above mean sea level. The coastal sector includes Quaternary marine terraces and low-relief coastal plains, locally interrupted by marked shoreline incisions. These morphostructural features reflect long-term morphotectonic processes initiated during the Pleistocene and still active under the present geological framework. The interaction between tectonic and marine processes controls the retreat of the coastal escarpments and contributes to the ongoing geomorphological evolution of the area.

This geological and geomorphological complexity makes Roca Vecchia a representative site for the investigation of coastal evolution and cliff instability. Furthermore, the coexistence of geological fragility and important cultural heritage makes the area particularly relevant for the assessment of coastal erosion processes and related hazards.

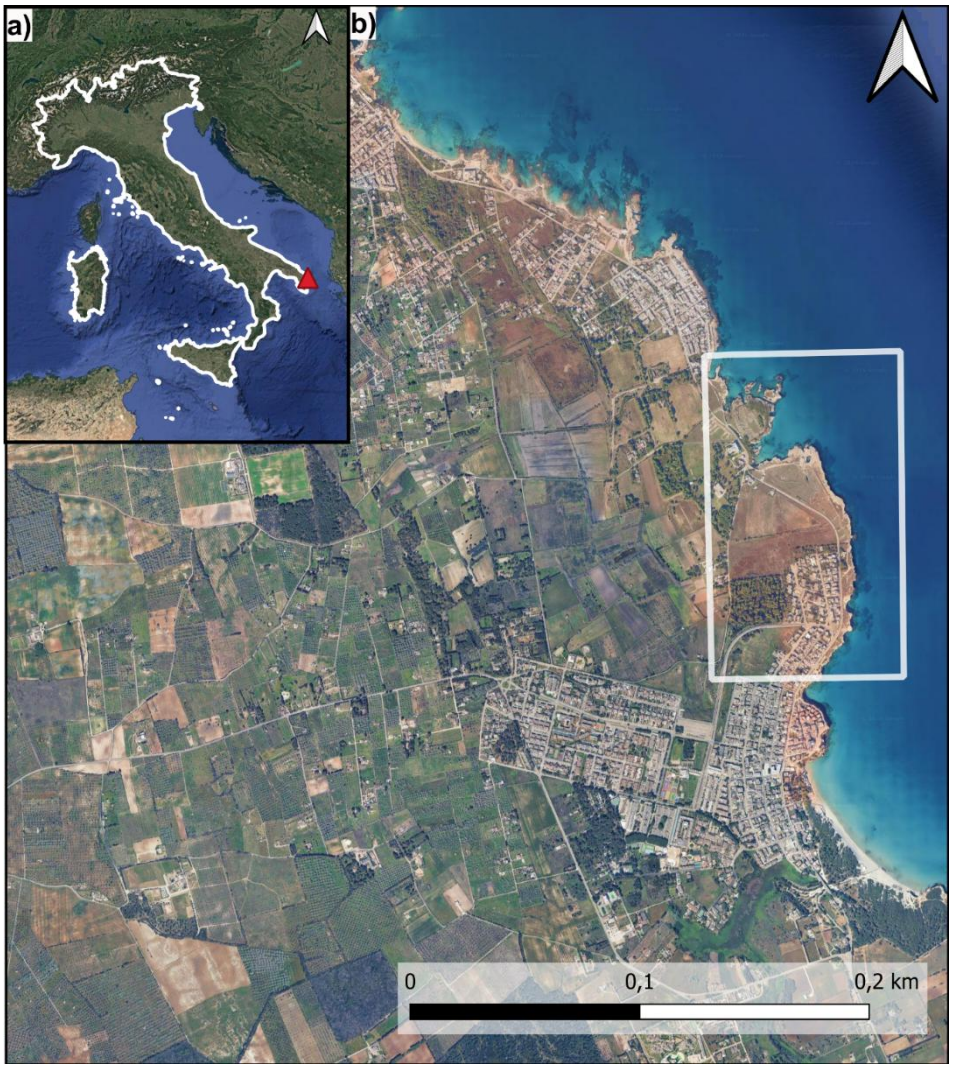

Figure 19 - Geographical localisation of the study area and aerial view of the area surrounding Grotta della Poesia, Roca Vecchia (LE).

From a geological point of view, Roca Vecchia belongs to the Apulian carbonate platform, which forms the structural basement of the Salento Peninsula. The evolution of the area has been strongly influenced by tectonic activity associated with the convergence between the African and Eurasian plates. The bedrock mainly consists of Mesozoic to Cenozoic carbonate lithologies, including limestones, calcarenites, and calcilutites, deposited within an epicontinental carbonate platform setting. These successions, mainly of Cretaceous age and subsequently affected by Miocene and Pleistocene tectonic phases, are intensely fractured. The discontinuity systems promoted karstification processes and contributed significantly to the instability of the coastal sectors.

Structurally, the area is characterised by joint and fault systems predominantly oriented NW–SE and NE–SW, consistent with the regional extensional tectonic regime active during the Cenozoic. Cliff instability processes at Roca Vecchia, including block toppling and rockfall

phenomena, are mainly controlled by the intersection of these discontinuity sets and by progressive karst dissolution affecting the carbonate rocks.
The hydrogeological setting is also influenced by tectonic structures, with deep confined aquifers hosted in Cretaceous limestones and shallower water tables developed in younger carbonate units. Marine intrusion into these aquifers contributes to coastal erosion and to the ongoing morphological evolution of the cliff system.
In recent decades, the area has experienced a considerable increase in tourism due to its scenic value, clear waters, and accessible caves, which are widely recognised as important geoheritage and geotourism elements along the Adriatic coast of Salento. However, the increase in anthropogenic pressure, particularly during the summer season, together with persistent natural erosion processes, has raised concerns regarding the preservation of both geological and archaeological heritage. The sectors most exposed to cliff instability are therefore of particular concern, and the observed geomorphological and structural conditions highlight the need for careful and sustainable site management.

2.2. Existing data retrieval and new monitoring data acquisition

The study of the Roca Vecchia coastal cliff was based on the integration of conventional engineering geological surveys and UAV-based remote sensing techniques. The adopted approach combined field observations with datasets derived from UAV photogrammetry, thermal surveying, and LiDAR acquisitions, with the aim of characterising the rock mass and assessing the stability conditions of the coastal sector. The integrated survey strategy was designed both to characterise the structural framework of the cliff and to assess the suitability of different UAV-derived datasets for stability analysis.
The workflow was designed to identify the most suitable point cloud products for the generation of three-dimensional meshes and for their application to engineering geological characterisation and stability analysis. Photogrammetric surveys were carried out using a DJI Mavic 3E equipped with an RGB camera. Thermal surveys were performed using a DJI Mavic 3T, whereas LiDAR data were acquired using a DJI Matrice 350 RTK platform equipped with a Zenmuse L2 LiDAR system. These datasets were used to identify geological features, derive structural parameters, and characterise the rock mass conditions of the study area.
Two different georeferencing strategies were adopted for the photogrammetric datasets: direct georeferencing through the onboard RTK system and indirect georeferencing based on Ground Control Points (GCPs). The models obtained using these two approaches were subsequently compared to evaluate their relative accuracy. The UAV-based products were then analysed together with conventional field data collected according to ISRM suggested methods for rock mass characterisation.
To support the photogrammetric processing, six reference markers were installed within the study area with a homogeneous spatial distribution. Each marker measured 60 × 60 cm and consisted of a high-contrast black-and-white target to ensure clear recognition in aerial images. Their coordinates were surveyed using a differential GNSS receiver (Emlid RS2), and the measured positions were used as GCPs during the photogrammetric processing.

2.3. Field and remote sensing surveys

Field and remote sensing surveys were carried out to characterise the geomorphological and geomechanical features of the Roca Vecchia coastal cliff and to evaluate the suitability of different UAV-derived products for engineering geological applications.
The photogrammetric survey was performed using a DJI Mavic 3E platform equipped with a DJI-RTK system. The UAV includes a 4/3 CMOS sensor with 20 effective megapixels and a field of view of 84°. The camera aperture ranges from f/2.8 to f/11, with a focus range from 1 m to infinity and ISO sensitivity ranging from 100 to 6400.
The survey was carried out at a constant flight altitude of 60 m above the take-off point, with 70% side overlap and 80% frontal overlap (Figure 20). The mission was conducted in automatic mode following a nadir-oriented flight plan, and a total of 909 images were acquired. To improve the reconstruction of vertical cliff faces, which were only partially represented by nadir imagery, an additional manual survey was performed. During this phase, two photogrammetric strips were acquired: one with the camera in a sub-horizontal position for frontal acquisition of the cliff, and one with a camera tilt angle of -45° in order to improve overlap between nadir and frontal images. Also in this case, frontal and side overlap were maintained at approximately 70% and 80%, respectively. The distance from the cliff was approximately 30 m. The integration of nadir and oblique images allowed the generation of a complete and detailed three-dimensional model of both sub-horizontal surfaces and near-vertical rock faces.

Figure 20 - DJI Mavic 3E vertical flight plan for the study area.

The LiDAR survey was carried out using a DJI Matrice 350 RTK platform equipped with a Zenmuse L2 LiDAR system. The sensor provides a vertical accuracy of about 4 cm and a horizontal accuracy of about 5 cm and supports multi-return acquisition, improving vegetation filtering and terrain detection.
The acquisition was performed at a constant altitude of 70 m above ground level, corresponding to an average ground sampling distance of approximately 2.66 cm. For data management purposes, the exported LiDAR point cloud was resampled to a point spacing of 10 cm. As in the photogrammetric survey, both nadiral and oblique sensor configurations were

adopted, with the oblique acquisition set at 45°. This acquisition geometry was fundamental for adequately describing both flat sectors and steep or vertical cliff faces.
To reduce shadowing effects related to the complex morphology of the cliff, two different flight missions were carried out, oriented NW–SE and NE–SW, respectively (Figure 21). In the first configuration, the cliff was scanned from the northwest, whereas in the second it was scanned from the northeast. The integration of these two LiDAR datasets produced a high-quality point cloud with improved coverage and greater reliability on the vertical rock surfaces.

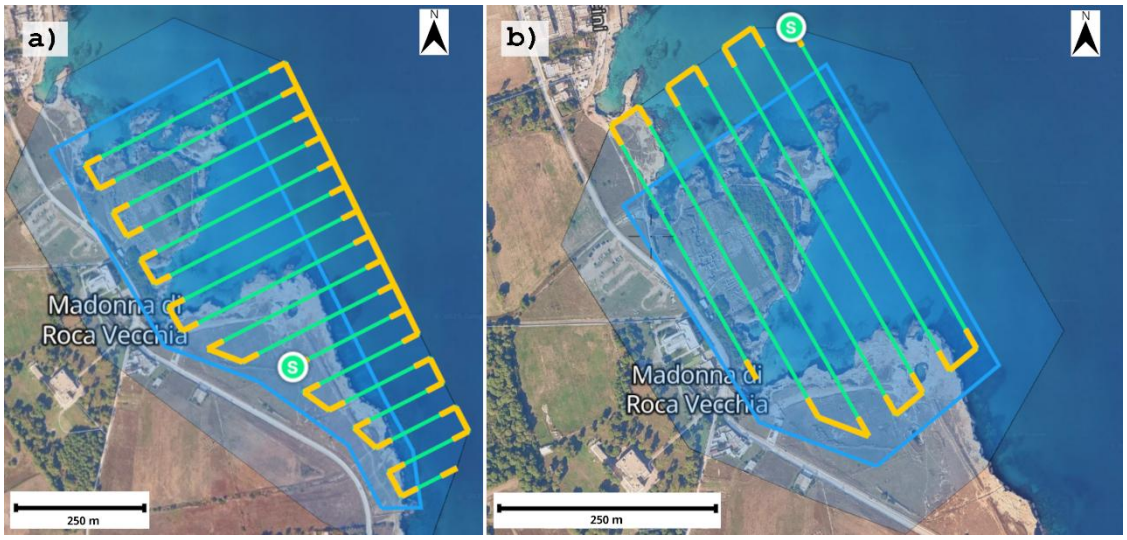

Figure 21 - Flight plans of the Matrice 350 RTK for data acquisition using an inclined gimbal, targeting the NW–SE oriented cliff (A) and the SW–NE oriented cliff (B).

Thermal data were acquired using a DJI Mavic 3T equipped with a DJI-RTK system and an uncooled VOx microbolometer thermal sensor. The thermal camera operates at 30 Hz, with a sensitivity of ≤50 mK at f/1.1, a temperature range between −20 °C and 150 °C, and an infrared wavelength range of 8–14 µm. Measurement accuracy is ±2 °C or ±2% of the measured value. The thermal survey was aimed at improving the recognition of weathered, fractured, and moisture-affected discontinuity surfaces. For this reason, the acquisition was carried out in manual flight mode under uniform solar illumination conditions and was limited to non-vegetated outcrops where bedrock was directly exposed.
Thermal image processing followed a four-step workflow: extraction of temperature data from each image, preprocessing through Python scripts to normalise and standardise the colour scale, generation of the point cloud in Agisoft Metashape, and post-processing through Python scripts to assign temperature values to each point on the basis of RGB colour-scale interpretation. This workflow enabled the generation of thermally attributed point clouds (Figure 22) suitable for both qualitative and quantitative geological and structural interpretation.

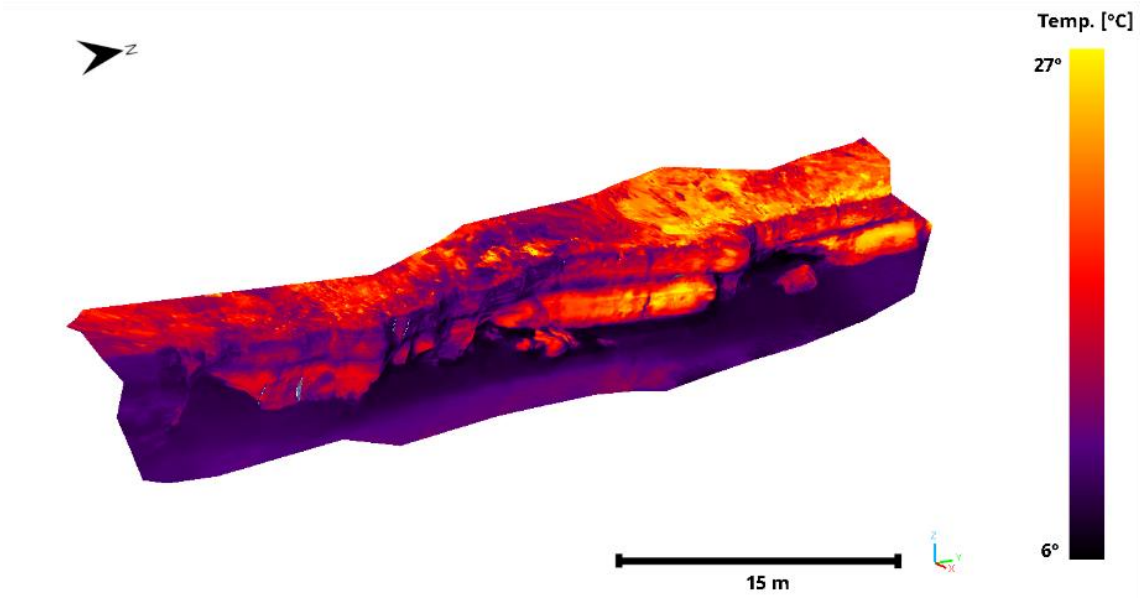

Figure 22 - RGB thermal point cloud visualised in CloudCompare using the Iron colour palette.

The thermal acquisition parameters, including distance, humidity, emissivity, and reflected temperature, were maintained constant throughout the survey.

2.4. Geomechanical characterisation

All UAV systems used in the study were equipped with DJI RTK modules, allowing centimetre-level positioning accuracy when connected to a network RTK correction service. In this study, real-time corrections were obtained through the Leica SmartNet ItalPoS network. Photogrammetric and thermal datasets were processed in Agisoft Metashape, whereas LiDAR data were processed in DJI Terra.
Photogrammetric processing was carried out using both RTK-based and GCP-based georeferencing approaches. The resulting models were compared in order to assess their positional consistency and to identify the most reliable dataset for engineering geological analysis. The thermal survey was also processed to generate a three-dimensional point cloud with temperature attribution, while the LiDAR survey provided the most detailed and reliable point cloud of the study area, particularly in sectors affected by vegetation and complex cliff geometry (Figures 22 and 23).

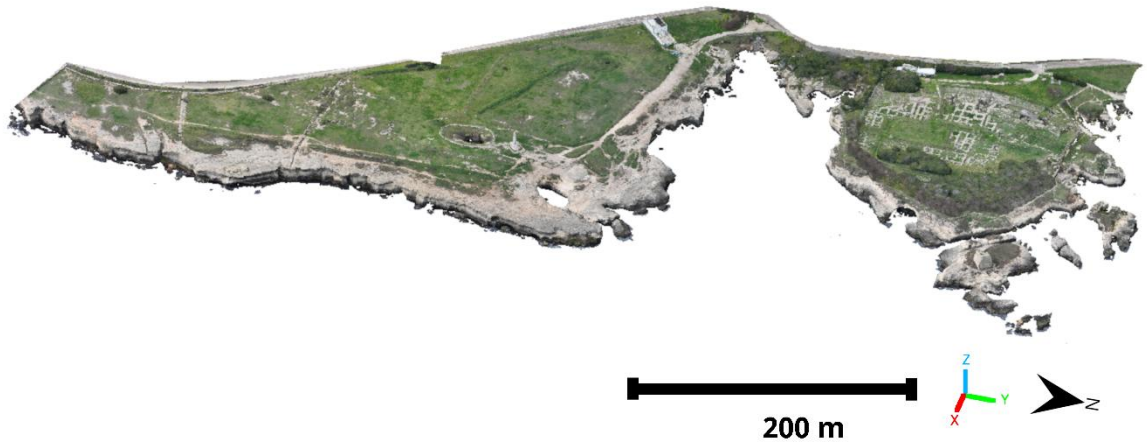

Figure 23 - LiDAR point cloud final product.

A comparison between the RTK-based and GCP-based photogrammetric products highlighted generally limited discrepancies in the horizontal component, whereas larger differences were observed along the vertical one. Additional point cloud and cloud-to-mesh comparisons carried out using the LiDAR model as reference confirmed that the GCP-based photogrammetric model provides a better overall agreement than the RTK-based solution. Nevertheless, both products proved suitable for the reconstruction of the coastal cliff and for the extraction of structural information.

A geomechanical characterisation of the Roca Vecchia coastal cliff was carried out through a virtual survey based on UAV-derived three-dimensional models. The structural analysis was performed in CloudCompare, while the extracted discontinuity data were subsequently analysed and clustered using Dips. The LiDAR-derived model was adopted as the main reference dataset due to its higher geometric accuracy and point density.

Discontinuity mapping was performed manually on the three-dimensional models, allowing the identification of the principal structural features affecting the coastal cliff. Geological and structural elements were mapped on both the LiDAR and thermal point clouds, while stereographic projections were used to analyse the orientation of discontinuity sets and bedding surfaces (Figures 24–25).

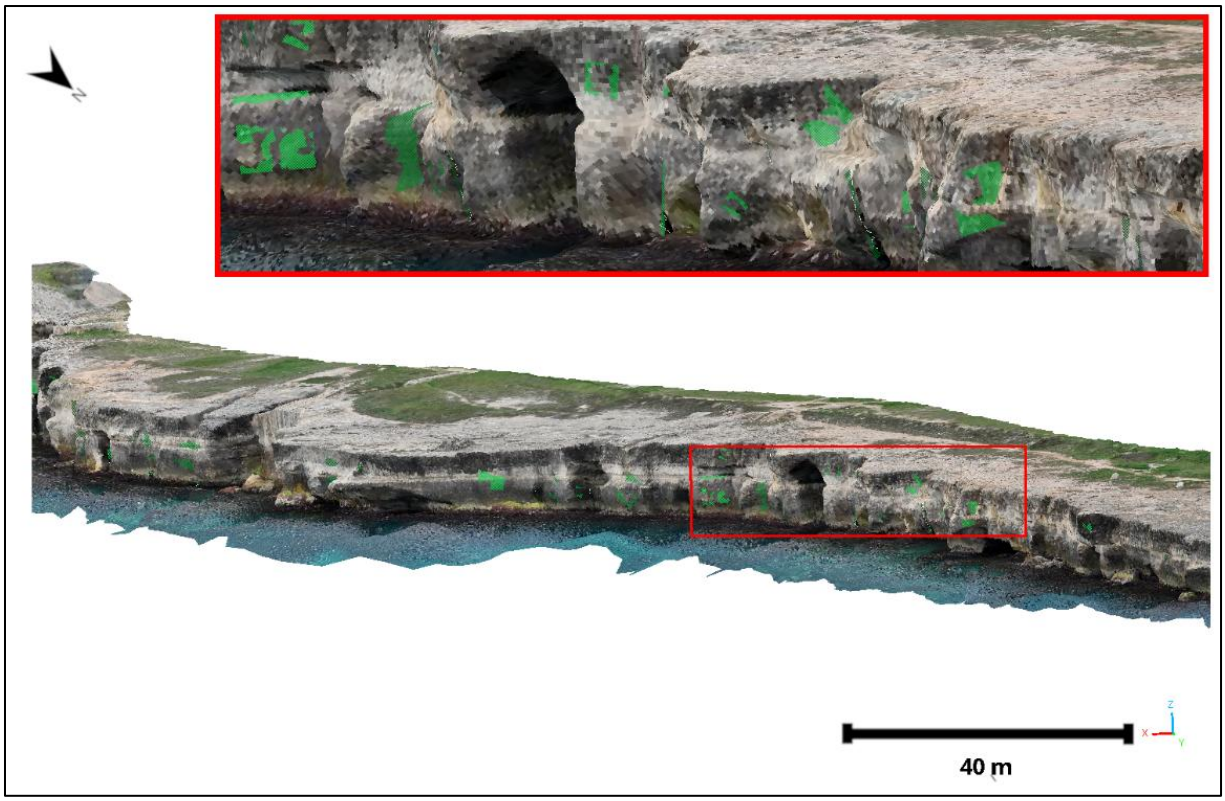

Figure 24 - Block and joint mapping on the LiDAR point cloud.

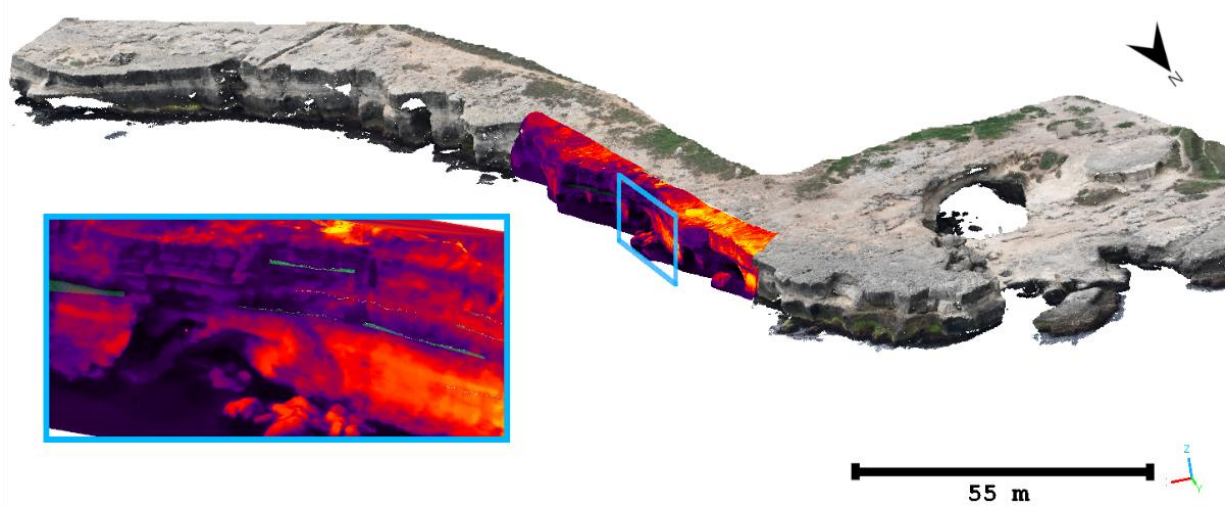

Figure 25 - Geological features mapped on the thermal point cloud.

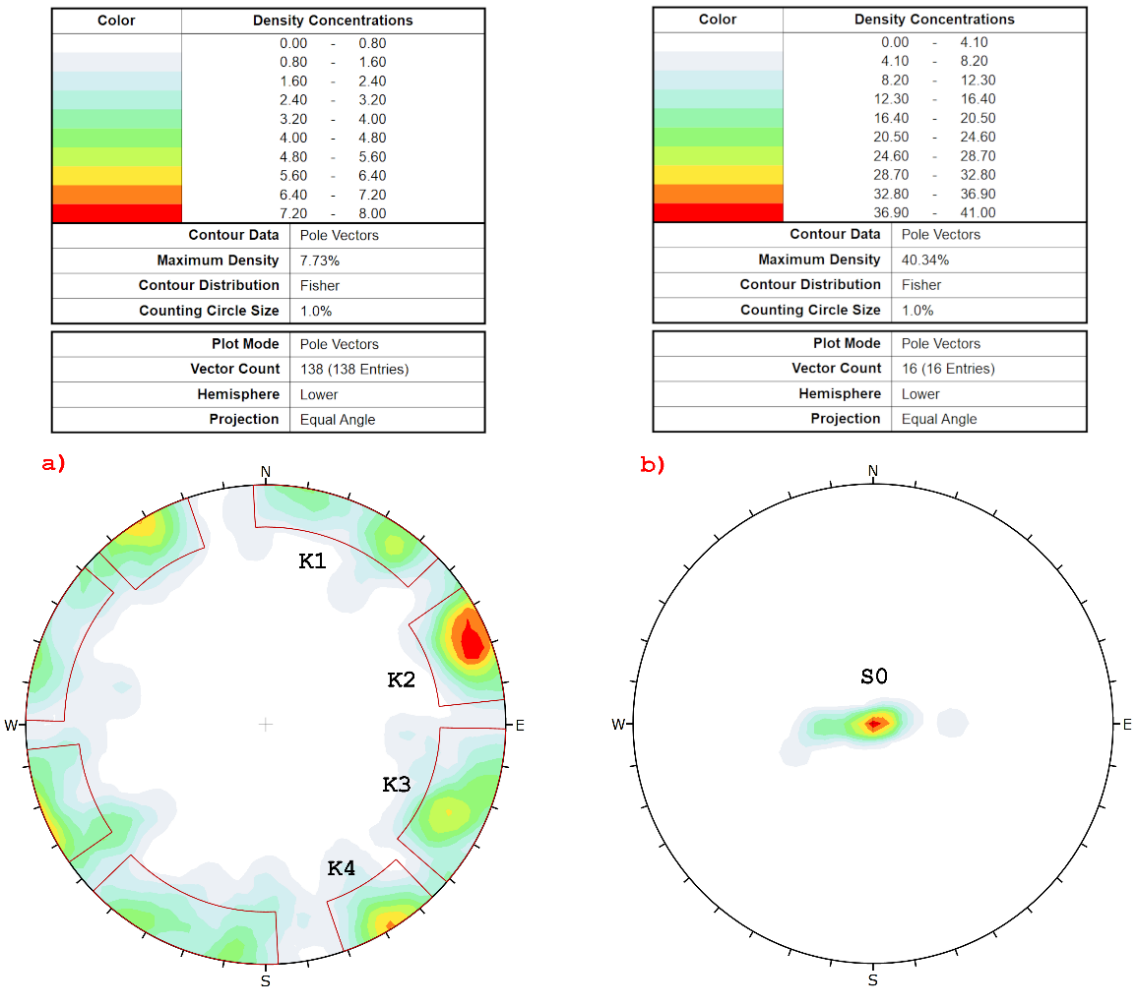

Figure 26 - Stereographic projections of the virtual geomechanical survey.

The structural analysis highlights the presence of four main sub-vertical discontinuity sets (K1–K4), characterised by dip directions ranging approximately between 20° and 170° and near-vertical dips. In addition, a sub-horizontal bedding plane (S0), dipping between 0° and 20°, was identified.

A good correspondence is observed among the discontinuity orientations derived from the LiDAR model, thermal data, coastline trends, and field geomechanical survey measurements. This agreement confirms the reliability of the identified structural framework and indicates a consistent structural pattern across the different datasets.

The comparison between discontinuity orientations and coastline trends suggests a strong structural control on cliff geometry. In particular, the coastline orientation appears to be closely related to the main discontinuity sets, highlighting the role of structural features in the morphological evolution of the coastal sector.

Further validation was obtained through the analysis of orthophoto-derived lineaments and preliminary gravimetric results related to karst caves and subsurface channels. These independent datasets show a good correspondence with the discontinuity pattern identified in the virtual geomechanical survey, confirming the influence of geological structures on both coastal development and karst evolution (Figure 27).

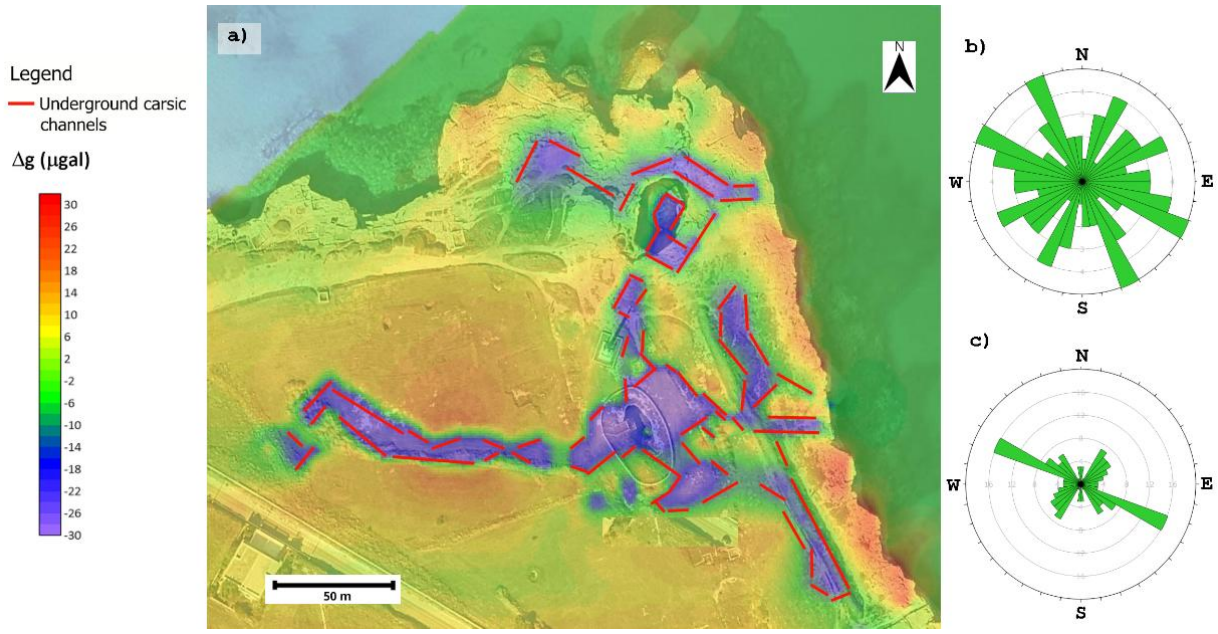

Figure 27 - Karst channels identified through gravimetric analysis and comparison with the main discontinuity orientations.

A comparative evaluation of selected discontinuity planes extracted from the GCP-based, RTK-based, thermal, and LiDAR-derived models indicates that the GCP-based and RTK-based datasets provide structural orientations generally consistent with those obtained from the LiDAR model. In contrast, the thermal point cloud shows lower reliability for the detailed measurement of steep discontinuities, although it proves particularly effective for the identification of sub-horizontal bedding planes and weathered sectors.
Overall, the integration of field observations and UAV-derived datasets allowed the definition of a consistent and reliable geomechanical framework of the coastal cliff, which represents the basis for the subsequent stability analyses.

2.5. Conventional and numerical slope analyses

To assess the stability conditions of the Roca Vecchia coastal cliff, the products derived from the integrated UAV surveys were used for a preliminary block stability analysis.
Based on the previous model comparisons, the GCP-based and LiDAR-derived point clouds were selected for merging, as they showed the highest degree of similarity. The objective of this operation was to improve point cloud quality and reduce shadow areas in the selected coastal sector used for the stability analyses.
The selected sector includes 186,967 points in the GCP-based point cloud and 2,995,932 points in the LiDAR-derived point cloud. The adopted workflow included fine registration through the Iterative Closest Point algorithm, merging of the two point clouds into a single dataset, subsampling to 0.5 m, weighted averaging based on point density and proximity, spatial distribution control, and denoising through Statistical Outlier Removal. The final integrated point cloud contains 25,635 points.
The integrated point cloud was then processed using an ad hoc MATLAB code developed to generate a three-dimensional mesh suitable for use in rock slope stability software. The code is available in a GitHub repository.

A preliminary rock slope stability analysis was subsequently performed using RocSlope3. The discontinuity sets used in the simulations were K1, K2, K3, K4, and the bedding plane S0, with orientations derived from the virtual geomechanical survey. Cohesion was set to 0 kPa, while the friction angle ranged from 20° to 50°.
The intersection between cliff geometry and discontinuity sets generated 16,709 blocks. These blocks were analysed through a Monte Carlo probabilistic approach using 200 simulations in order to obtain a preliminary estimate of instability conditions. The results are expressed in terms of Probability of Failure and allowed the identification of potentially rockfall-prone sectors. A total of 619 potentially unstable blocks were identified (Figure 28).

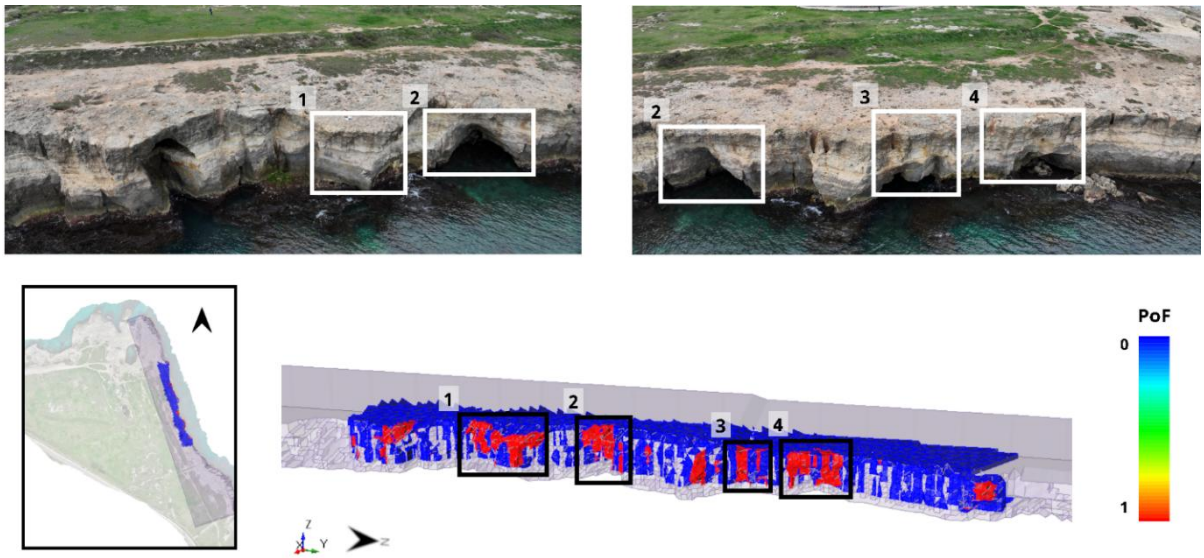

Figure 28 - Block Stability Analysis. The highlighted blocks indicate the unstable areas identified in the UAV images and in the RocSlope3 simulations. The legend represents the Probability of Failure (PoF).

The analyses indicate that LiDAR provides the most reliable dataset for the reconstruction of morphologically complex, vegetated, and sub-vertical coastal environments. Photogrammetric products, particularly those based on GCPs, represent an effective alternative where the required accuracy is moderate and operational costs must be reduced. The RTK-based photogrammetric approach also constitutes a practical solution where GCP installation is not feasible, although a reduction in vertical accuracy was observed in this case study.
The comparison among the different products shows that variations in point cloud quality directly influence the geometric quality of the derived models. However, for geomechanical purposes, the orientations of discontinuities extracted from the GCP-based, RTK-based, and LiDAR-derived models are generally comparable, with angular differences commonly below 5°. The thermal point cloud proved less reliable for the precise mapping of steep structural features, but useful for the recognition of sub-horizontal bedding planes and weathered sectors.
Overall, the integration of LiDAR and GCP-based photogrammetric data improved point cloud quality, reduced shadow areas, and enabled the generation of a three-dimensional mesh suitable for slope stability analysis. The adopted workflow allowed the preliminary identification of unstable sectors and proved effective in supporting hazard assessment and future monitoring activities.

Surveys and stability analysis pointed out that discontinuity orientations and coastline trends are closely related, suggesting a strong structural control on cliff geometry. In particular, the coastline orientation appears to be closely related to the main discontinuity sets, highlighting the role of structural features and karst in the morphological evolution of the coastal sector.

3. Havišće bay

3.1. Introduction

This document reports on the field and laboratory activities performed within the RESONANCE project, aimed to provide input data for the slope stability analyses as one of the main deliverables of the Project. First part provides an overview of activities on assessment of strength properties of sandstone rock samples and the influence of moisture content on strength changes. Second part deals with field and laboratory activities performed to obtain characterization of the colluvial soil covering the slope in the central part of the bay, as well as on the establishment of the field monitoring system that provides an insight into the soil moisture and pore water pressure conditions. Together with previously performed physical surveys at the neighbouring location, these provided valuable input data for the slope stability analyses that asses global and local stability conditions at selected profiles. The results of limit equilibrium and finite element - based slope stability analyses are reported in the final part of the report.

3.1.1. Overview of prior activities, conclusions and the purpose of the report

The previous report presented the results of testing three groups of sandstone samples from Havišće Bay (Jadranovo, in the western part of the Vinodol channel) on the north-eastern Adriatic coast (Figure 29), which were tested in their natural state, dry and after 24 hours of wetting. The location is one of the pilot areas in the project “Improving landslide risk prevention and management in coastal areas (RESONANCE)”, financed by the EU cross-border cooperation program Interreg Italy - Croatia 2021 - 2027. These results indicated on the basic strength properties of sandstones at three locations in the bay, after that it was concluded that more samples need to be tested in order to draw conclusions about the influence of the marine environment on the mechanical characteristics of the surface materials in parts of the bay that are more or less exposed.

New sandstone samples were taken in October from the same two locations as in previous testing. Testing results will be used in multidisciplinary coastal research, in order to potentially predict future processes dependent on climate variations, and to create vulnerability and risk maps of the analysed areas. Investigation reported in this document includes more sampling and laboratory testing, interpretation of the overall results and their implementation in the stability analyses.

3.1.2. Location and geological context of the Havišće site

As previously reported, according to the geological map of the Republic of Croatia (HGI, 2009), the pilot area is built in Liburnian deposits, foraminiferal limestones and transitional deposits (Figure 29b, mark number 39). The red circle on the map indicates the Havišće Bay location where new samples were taken for further laboratory testing.

Liburian deposits and foraminiferal limestones occupy a significant part of the Croatian part of the Dinarides, in a zone that extends more or less continuously from Istria to Konavle. These deposits are transgressive onto older deposits (predominantly Upper Cretaceous limestones). Transitional deposits are composed of clayey limestones, calcitic marls and marls which, in addition to a fine-grained carbonate and siliciclastic matrix, contain individual bioclasts of benthic organisms and planktonic foraminifera (Vlahović i Velić, 2009). Rudist limestones are clearly visible on the western side of the bay.

Slope instability has been evidenced on the field (tilted trees, cracks, collapsed tress walls and sunken stairs). Slope stability analyses were performed around this area, with the known geophysics data.

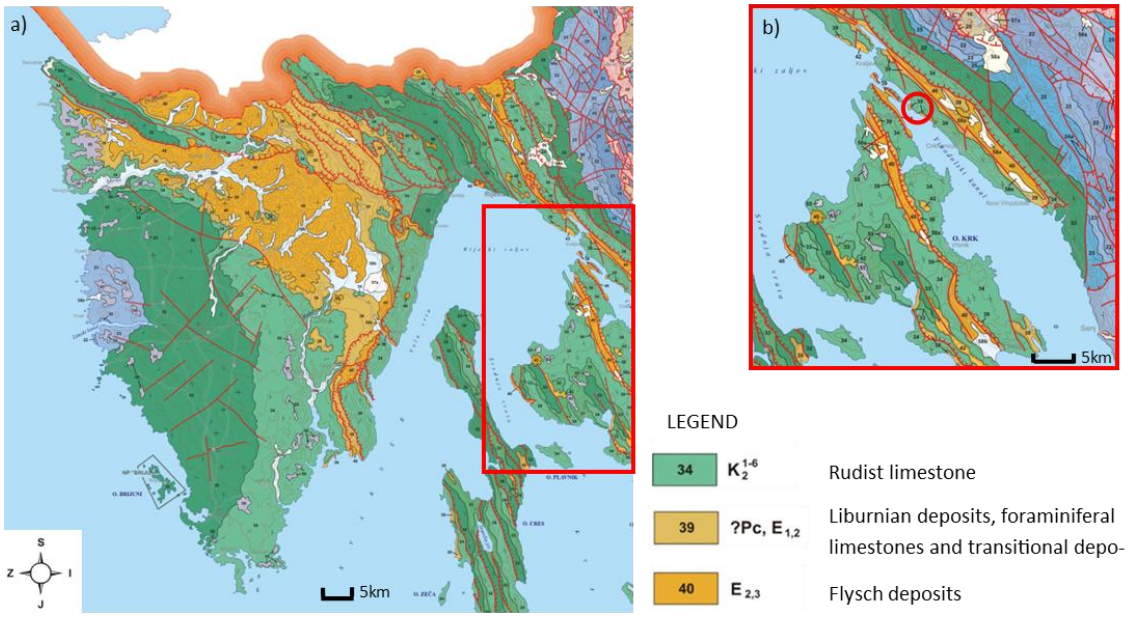

Figure 29 - Havišće Bay location on the geological map of the Republic of Croatia Scale 1:300,000 (Croatian Geological Institute, 2009).

3.2. Sandstone rock sampling and testing

Sandstone rock samples were collected in October 2025 at the same locations in Havišće bay, as in the previous testing (reported in the last report) and shown in Figure 30. Location 1 samples were mostly taken from the unstable slope where they were poorly bound or had already separated from the rest of the rock mass. The samples from Location 2 were taken underneath the slope.

a) b)

Figure 30 - Sandstone rock sampling locations in Havišće Bay: a) Location 1 (on the slope that collapsed); b) Location 2 (behind the coastal wall and under the slope).

Samples present mostly homogeneous sandstones, superficially orange to yellowish brown colour, while inside they are mostly grey. All the samples were transported in plastic bags to the laboratory and protected from changes in humidity, kept in laboratory conditions, until the testing. Since there are no homogeneous sandstone outcrops on the site on which field strength testing could be conducted, only Point Load testing of different moisture conditions was performed in the laboratory for the purpose of his report.

3.2.1. Laboratory testing

In the laboratory, uniaxial compressive strength testing was carried out on a PLT device and the moisture content of the tested samples was determined (in situ water content, water content after 24h wetting process, and water content after one week wetting). First PLT testing was carried out on samples of natural humidity, for the two group of samples. After 24 hours of drying, the natural humidity of the samples was determined.

The sample is placed in a drying oven at 105–110 °C for 24 hours. After cooling in a desiccator (to avoid reabsorption of moisture from the air), the sample is weighed again. The moisture content is determined from the equation:

$$w = \frac{m_{wet} - m_{dry}}{m_{dry}} x100\%$$

The samples were then submerged for 24 hours and PLT testing was performed again to determine the effect of the water content on the change in strength. The same procedure was repeated, but with the 7 days wetting process and afterwards testing. Also, the PLT testing after 7 days wetting process was performed on two groups of samples, one going through the procedure first time, and the other group that undergone two cycles of drying and wetting before this cycle. It is important to mention that the samples were not surface dried before testing, but they were only left for several minutes to drain.

3.2.2. Point Load Strength Index Test (PLT)

A in the previous testing reported in the last document, the PLT was performed in accordance with the ISRM (1985) standardized procedure for irregular sample testing. Digital Point Load test apparatus, from the Geotechnical laboratory was used for PLT of the rock samples (Figure 31).

Figure 31 - Point Load test testing at the Geotechnical Laboratory, University of Rijeka, Faculty of Civil Engineering.

At least 10 tests per each group of rock material were performed on irregular specimens. The load was increased so the failure occurred within 10-60s and the failure load P is recorded. At the end of the test, 4 values needed for the calculation were obtained: sample size (D, W_1, W_2) [mm] and failure load P [kN], where D corresponds to the sample hight at the breaking point, and W_1 and W_2 are the corresponding widths of the sample cross-section.
Value of the effective diameter D_e was calculated from the equation:

$$D_e = \sqrt{\frac{4 * W * D}{\pi}}$$

The strength index is determined from the equation:

$$I_{s(50)} = F * \frac{P}{D_e^2}$$

Where F corresponds to the size correction factor calculated from the equation:

$$F = (D_e/50)^{0.45}$$

The mean value of $Is_{(50)}$ was calculated by deleting the two highest and lowest values from 10 or more valid tests, and calculating the mean of the remaining values. When fewer than 10 values were tested, only the highest and lowest values are deleted and the mean calculated from those remaining. Used index-to-strength conversion factor (β) is 21.9 (Singh et al. 2012).

3.2.3. Interpretation of the testing results

All the performed test were valid, and none of the specimens cracked irregularly during the PLT testing. The results obtained on sandstones samples from Havišće Bay are given in Table 5 (samples with *in situ* water content), Table 6 (after 24h wetting), and Table 7 and 8 (after 7 days of wetting). The 7 days wetting was performed for the two groups of samples from Location 1 and Location 2. One group of samples had 2 cycles of drying and wetting (Table 7) and the other was exposed to 7 days wetting starting from the natural condition (Table 8).

Table 5 - Point Load testing results of samples with *in situ* water content.

	No.	De [mm]	D [mm]	W [mm]	P [N]	$I_{s(50)}$ [MPa]	UCS [MPa]	Mean v UCS [MPa]
location 1- natural humidity	1	75,55	46,5	96,40	2040	0,43	9,43	55,00
	2	73,53	37,5	113,25	11320	2,49	54,54	
	3	70,29	60,02	64,65	5170	1,22	26,71	
	4	71,89	46,1	88,05	14900	3,39	74,35	
	5	69,31	51,4	73,40	7570	1,83	39,97	
	6	59,69	33,1	84,55	15720	4,78	104,63	
	7	80,75	54,8	93,45	19020	3,62	79,26	
	8	62,07	65,7	46,05	12300	3,52	77,07	
	9	41,91	28,3	48,75	1150	0,60	13,24	
	10	63,58	37,4	84,90	5480	1,51	33,08	
	11	45,91	28,4	58,30	10720	4,89	107,17	
location 2- natural humidity	1	84,96	59,4	95,45	22930	4,03	88,31	68,70
	2	57,50	45,6	56,95	4730	1,52	33,36	
	3	58,11	46,2	57,40	7530	2,39	52,26	
	4	74,01	63,6	67,65	11610	2,53	55,37	
	5	77,36	57,6	81,60	16440	3,34	73,22	
	6	65,94	63,3	53,95	11090	2,89	63,26	
	7	58,66	36,5	74,05	8460	2,64	57,85	
	8	67,71	51,3	70,20	5500	1,37	30,11	
	9	81,27	54,2	95,70	15190	2,86	62,68	
	10	58,06	33,6	78,80	2730	0,87	18,97	

Table 6 - Point Load testing results after 24h wetting.

	No.	De [mm]	D [mm]	W [mm]	P [N]	$I_{s(50)}$ [MPa]	UCS [MPa]	Mean v UCS [MPa]
location 1- after 24h wetting	1	56,89	31,6	80,45	11920	3,90	85,47	68,70
	2	65,81	58,9	57,75	10050	2,63	57,51	
	3	58,68	32,8	82,45	4270	1,33	29,19	
	4	62,92	36,6	84,95	14050	3,94	86,19	
	5	73,03	45,7	91,65	6420	1,43	31,26	
	6	53,88	40,5	56,30	4330	1,54	33,78	

	7	61,63	34	87,75	12840	3,71	81,33	
	8	68,01	36,6	99,25	14880	3,69	80,92	
	9	60,95	42,2	69,15	11550	3,40	74,43	
	10	63,48	31,2	101,45	13920	3,85	84,22	
location 2- after 24h wetting	1	66,24	36,8	93,65	7150	1,85	40,50	67,41
	2	70,12	59,5	64,90	15830	3,75	82,10	
	3	86,83	72,7	81,45	6130	1,04	22,83	
	4	60,81	49,6	58,55	17900	5,29	115,78	
	5	72,82	58,7	70,95	12140	2,71	59,38	
	6	59,15	33,8	81,30	6880	2,12	46,45	
	7	67,77	33,6	107,35	8810	2,20	48,17	
	8	55,65	46,6	52,20	15340	5,20	113,82	
	9	52,72	33,2	65,75	6760	2,49	54,55	
	10	54,58	46,2	50,65	18580	6,49	142,07	

Table 7 - Point Load testing results after 7 days wetting of samples that undergone the 2 cycles of drying and wetting.

	No.	De [mm]	D [mm]	W [mm]	P [N]	$I_{s(50)}$ [MPa]	UCS [MPa]	Mean v UCS [MPa]
location 1- after 7 days wetting	1	38,90	29,2	40,70	7750	4,57	100,18	86,61
	2	42,24	29,6	47,35	9090	4,72	103,41	
	3	50,94	35,6	57,25	8030	3,12	68,34	
	4	37,82	34,1	32,95	6610	4,08	89,24	
	5	38,58	34,9	33,50	4500	2,69	58,91	
	6	44,68	42,1	37,25	3000	1,43	31,28	
	7	38,90	27,6	43,05	6630	3,91	85,72	
	8	38,03	32,5	34,95	8390	5,13	112,33	
	9	41,85	25,1	54,80	3550	1,87	40,98	
	10	34,45	27,3	34,15	7760	5,53	121,08	
	11	38,86	30,1	39,40	8750	4,59	100,48	
location 2- after 7 days wetting	1	59,39	31,3	88,50	10880	2,68	58,71	66,94
	2	56,85	35,2	72,10	6310	2,07	45,31	
	3	41,92	34,5	40,00	5130	2,70	59,06	
	4	36,26	31,3	33,00	4730	3,11	68,17	
	5	41,13	32,6	40,75	4980	2,70	59,05	
	6	49,99	38,6	50,85	14750	5,90	129,24	
	7	44,17	28,7	53,40	6890	3,34	73,13	
	8	53,49	56,4	39,85	13390	4,82	105,64	
	9	41,16	36,4	36,55	4340	2,35	51,40	
	10	50,54	41,7	48,10	8840	3,48	76,17	
	11	57,74	55,3	47,35	12820	4,10	89,85	
	12	39,87	29,3	42,60	2750	1,56	34,22	

Table 8 - Point Load testing results after 7 days wetting of samples that didn't go through 2 cycles of drying and wetting.

	No.	De [mm]	D [mm]	W [mm]	P [N]	Is(50) [MPa]	UCS [MPa]	Mean v UCS [MPa]
location 1- after 7 days wetting	1	47,72	27,9	64,10	3400	1,46	32,02	74,55
	2	47,72	41,5	43,10	10940	4,70	103,02	
	3	47,34	27,4	64,25	10400	4,53	99,15	
	4	46,12	20,1	83,10	5310	2,41	52,73	
	5	47,64	32,8	54,35	9630	4,15	90,92	
	6	44,12	26,7	57,25	6070	2,95	64,56	
	7	53,39	32,4	69,10	7710	2,79	61,01	
	8	41,22	25,2	52,95	2530	1,37	29,90	
	9	51,98	32,8	64,70	11190	4,21	92,30	
	10	50,45	43,7	45,75	9230	3,64	79,73	
	11	50,09	40,8	48,30	9600	3,68	80,63	
location 2- after 7 days wetting	1	41,42	31,7	42,50	5710	5,14	112,60	54,30
	2	42,89	35,5	40,70	3930	1,99	43,66	
	3	37,38	27,1	40,50	4850	3,04	66,68	
	4	71,57	40,7	98,85	8920	2,05	44,82	
	5	50,33	32,3	61,60	1870	0,74	16,21	
	6	40,42	31	41,40	5010	2,79	61,02	
	7	58,04	45	58,80	4710	1,50	32,74	
	8	46,56	38,7	44,00	3720	1,66	36,39	
	9	56,49	48,1	52,10	7550	2,50	54,74	
	10	38,23	35,7	32,15	4170	2,53	55,38	
	11	60,94	57,3	50,90	7940	2,34	51,19	
	12	56,95	42,7	59,65	9340	3,05	66,88	

Red values of the UCS were the two minimum and the two maximum values that were not taken into account for the mean value calculation.

The variations of the Point Load Strength with the water content are particularly pronounced for the water saturation below 25%. We wanted to determine how wetting affects strength, after a 24-hour draying and wetting process and after the same cycle repeated on the same samples and wetting during 7 days. Another thing that we were interested in was the influence of two drying and wetting cycles on the results.

Point Load Test results for samples with in situ water content, considering the corresponding conversion factor gave the mean UCS value of 55,00MPa at location 1 and the mean 68,70 MPa at the location 2. Table 6 shows the result after PLT testing after 24h wetting. The results show that the UCS values increased at location 1 compared with the previous to the value 68,70 MPa at location 1 and value 67,41 MPa at the location 2. It is expected that the failure likely initiated through the saturated zone, where the intergranular bonding is reduced, contributing to reduced Point Load Strength Index under wet conditions, however, the observations and the results (especially at the Location 1) did not confirm these expectations. The sandstone specimens show a clearly defined darker zone, indicating water penetration after wetting (Figure 32). The penetration front is irregular but well delineated, forming a lens-

shaped to asymmetric saturated zone. Water ingress is partial, not fully saturating the specimen, which suggests heterogeneous cementation or grain packing and capillary-controlled flow through the intact rock pores. Considering the obviously short wetting period, the corresponding irregular and mostly surface water penetration may be the cause of the results which are effectively corresponding to the two similar moisture states. It can be seen that the cone contact and load direction pass through the dry specimen area.

Another possible cause of such results can be the period of sampling and the corresponding natural water content. The samples were taken in October after a rainy period, unlike the sampling in June 2025, when the first group of samples was tested. In this case natural specimens were already fairly moist. The natural humidity of the samples at location 1 was 1,68%, while the natural humidity on the location 2 was 1,41%. The moisture content of the samples after 24 hours of wetting increased, and was 2,19% for the location 1 and 2,23% for the location 2. After 7 days of wetting the moisture content for location 1 increased to 2,64% and for the location 2 it was 2,70%. In comparison with the testing performed in June, the natural water content in October at location 1 was 73% larger than in the case of the specimens tested in summer period, and 85% larger at location 2 (Table 9). The samples collected in June show the changing in water content after the 24h wetting in 136% and 175% for location 1 and 2, while the samples collected in October show significantly lower water content change after 24h wetting 30% and 58% for location 1 and 2 correspondently. Since only the group of samples collected in October was exposed for the 7 day wetting, it cannot be compared to sampling in June, and it can be concluded that the water content after 7 days of wetting increased from the natural state for 57% and 91% for location 1 and 2 (Table 9).

Another reason for the unexpected increase in strength results, is that the wetting can increase apparent strength in point-load due to suction effects.

Table 9 - Changes in water content during different periods and wetting processes.

Sampling location	**w (%)-natural**		**w (%)-24h wetting**		**w (%)-7 days wetting**
	June	October	June	October	October
1	0,97	1,68	2,29	2,19	2,64
2	0,76	1,41	2,09	2,23	2,70

Figure 32 - Sandstone sample after testing: different water penetration patterns.

Point-load results are also sensitive to mineralogical composition, lamination orientation, grain-size bands, iron-oxide cemented layers and the pre-existing microcracks. All this can influence the moisture penetration and effects as well at the strength results. On some of the samples, after braking, more worn brownish areas inside the sample were visible (Figure 33). Dark brown zone is probably mineralogically distinct layer (iron-oxide–rich or more fine-grained), with higher porosity and/or water retention capacity, possibly behaving as a moisture reservoir. It can be concluded that these layers affect the resulting strength of the material.

Figure 33 - Dark brownish areas inside the sample.

Considering all data sets and testing results, from June and October 2025, at Location 1 and Location 2 in Havišće Bay, the following arises:

- seasonal effect (June vs October) is significant-

Different pre-test moisture histories, temperature and humidity effects during sampling show, as previously mentioned, considerable effect on the results. Seasonal variations between June and October further indicate that “natural moisture content” represents a variable reference state rather than a strictly dry condition.

- water penetration is heterogeneous –

The penetration front is irregular but well delineated, forming a lens-shaped to asymmetric saturated zone. Water ingress is partial, not fully saturating the specimen, which suggests heterogeneous conditions, allowing the breaking path through the dry area.

- wetting does not systematically reduce strength-

After 24 h wetting (June samples) UCS decreases relative to natural condition. Short-term wetting (24 h) has shown classical weakening effect, as predicted in the rock mechanics theory. These results confirm that sandstone is water sensitive in the conditions of relatively low water content in the natural conditions, and considerable water content increase (up to 175%).
Samples tested in October after 24 h /7 days wetting show UCS equal to or higher than the natural condition. Sandstone behaves as a structurally stable framework (quartz-dominated), well interlocked and not affected by water content.
Wetting/drying cycles usually reduce sandstone strength (microcracking, cement degradation etc.), so you'd expect the samples that undergone 2 cycles of drying/wetting to be weaker than the "natural condition" ones. The results of testing on few samples from this site doesn't confirm this assumption. The reason to explain such results, is that sandstones are not sensitive to only 2 wetting–drying cycles. Only 2 cycles are not significant to notice the decrease in strength, or the strength can even rise if moisture state effects dominate.
Table 10. Shows the Comparison of strength properties for the samples tested in June and October, considering the same testing procedures, and the same conversion factor.

Table 10 - Comparison of strength properties for the samples tested in June and October.

Sampling location	**UCS (MPa)- natural w**		**UCS (MPa)- 24h wetting**		**UCS (MPa) - 7 days wetting (2 cycles of drying and wetting)**	**UCS (MPa) - 7 days wetting (one cycle of drying and wetting)**
	June	October	June	October	October	October
1	75,10	55,00	59,82	68,70	86,61	74,55
2	66,21	68,70	49,34	67,41	66,94	54,30

Different specimen slenderness (D/W) or size effect, for all tested samples in June and October (same location and wetting conditions) was analysed (Table 11, Figure 34). Increase of the mean UCS value with the increase of the D/W ratio is shown in Table 11. Ratios less than 0.3 and greater than 1.0 were not considered (according to the ISRM recommendations).

Table 11 - Comparison of mean UCS values for all tested samples considering different D/W ratio.

Sampling location	**UCS (MPa) -natural w**		**UCS (MPa) - 24h wetting**		**UCS (MPa) - 7 days wetting (2 cycles of drying and wetting)**		**UCS (MPa) - 7 days wetting (one cycle of drying and wetting)**	
	D/W (0.3-0.6)	D/W (0.7-1.0)	D/W (0.3-0.6)	D/W (0.7-1.0)	D/W (0.3-0.6)	D/W (0.7-1.0)	D/W (0.3-0.6)	D/W (0.7-1.0)
1	32,95	22,36	35,95	53,57	42,63	83,29	34,89	52,68
2	63,02	66,04	30,59	70,45	25,42	68,19	30,51	31,70

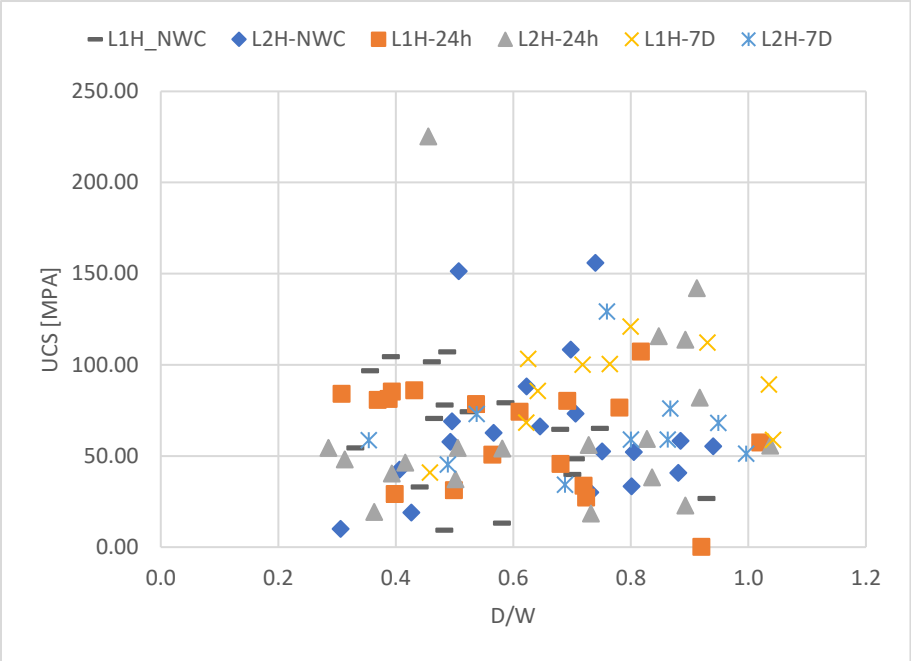

Figure 34 - Sandstone mean UCS values considering different D/W ratio.

3.2.4. Concluding remarks on the sandstones strength properties

The conducted testing indicate the basic strength properties of sandstones at the pilot location Havišće Bay, taken from the cover at two locations. The preliminary results indicate on heterogeneous water penetration and saturation conditions and significant seasonal effect i.e. reference natural water content as possible key parameters influencing strength properties.

The sandstones collected and tested in June, have shown the increased in UCS values after 24h of drying and expectedly decreased UCS values after 24h of wetting. Considering all data sets and testing results, from June and October 2025, at both locations in Havišće Bay, the following conclusions arise: (i) wetting does influence strength; (ii) water penetration is heterogeneous and (iii) seasonal effect (June vs October) is possible. The penetration front is irregular but well delineated, forming a lens-shaped to asymmetric saturated zone. Water ingress is partial, not fully saturating the specimen, which suggests heterogeneous conditions, allowing the breaking path through the dry area. As mentioned, short-term wetting (24 h) of samples taken in June has shown classical weakening effect, as predicted in the rock mechanics theory, what was surprising, samples tested in October after 24 h /7 days wetting show UCS equal to or higher than in the natural condition. Factors, that have not been considered systematically in this analysis, and that might have influence on the Point Load Strength results, are mineralogical composition, lamination, grain-size bands, iron-oxide cemented layers, microcracks and suction effects. It can be concluded that sandstones are not sensitive to only 2 wetting–drying cycles, and that more samples with systematic consideration of all influencing factors should be considered to draw further conclusions about the influence of the marine environment on the mechanical characteristics of the surface materials in parts of the bay that are more or less exposed to drying and wetting process.

3.3. Field monitoring establishment and surficial soil characterization

During December 2025, January and February 2026, additional field investigations and laboratory testing were carried out at a site adjacent to the area where geophysical surveys had been conducted during the previous project phase. The site is characterized by a colluvial soil cover overlying bedrock at an approximate depth of 5 m, as identified by earlier geophysical investigations. The objective of this study was to establish a hydrological and meteorological monitoring point, perform soil sampling and laboratory characterization of collected intact and disturbed soil samples, which would provide an input data needed to conduct both global and local slope stability analyses under varying groundwater conditions.
The location shown in Figure 35, situated adjacent to the previous geophysical survey lines and known to have been affected by numerous local instability events in the past (Figure 36), was identified as suitable both for the installation of a monitoring point and for conducting soil characterization to support representative slope stability analyses.

Figure 35 - Monitoring and soil sampling location (45.219882, 14.616521), indicated by a red arrow, next to the geophysical survey location (indicated by a dashed yellow line).

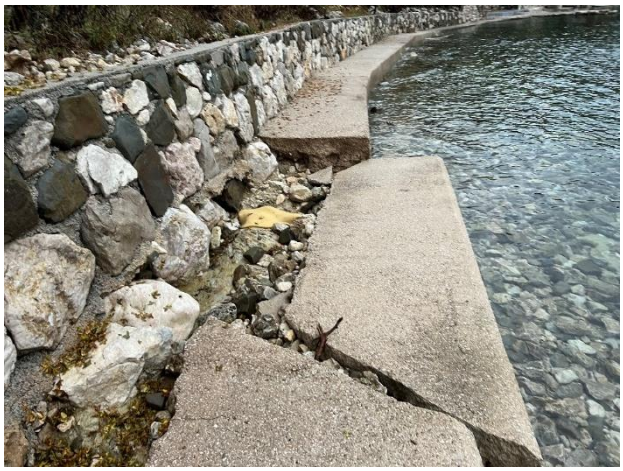

Figure 36 - Examples of past local instabilities at the sampling location due to the slope's toe erosion.

During sampling activities, information on soil conditions, groundwater, and other relevant site characteristics was documented.

3.3.1. Establishment of the field monitoring system

The monitoring equipment was procured within the project from METER Group. The sensors used include standard field tensiometers TEROS 32, soil moisture profile probe TEROS 54, TEROS 21 soil water potential sensors, and the ATMOS 41 Gen 2 weather station. The devices were connected to the zL-6 data logger to provide a continuous monitoring data. All sensors were tested under laboratory conditions prior to field installation (Figure 37).

Figure 37 - Testing of the monitoring equipment under laboratory conditions prior to field installation.

The TEROS 54 sensor is used for measuring volumetric water content at four depths: 15, 30, 45, and 60 cm. Installation was performed in accordance with the manufacturer's manual, using a sliding hammer attached to the sensor head. The hammer was removed after the sensor was driven into the ground (Figure 38).
TEROS 32 sensors were installed at three different depths of 15, 30 and 60 cm and they are used to measure both positive and negative pore water pressure (Figure 39). Setting up TEROS 32 required on-field filling of sensor with syringe of demineralized and deaired water.
TEROS 21 was placed at 15 cm of depth to measure water suction at the dry measurement range, when due to limitations in direct measurement of soil suction, TEROS 32 could not provide relevant readings. Every sensor was connected to data logger that uploads data on cloud service, ZENTRA Cloud (Figure 40).

Figure 38 - a) Installation process of the TEROS 54 sensor; b) TEROS 54 sensor; c) Installed TEROS 54 sensor.

Figure 39 - a) TEROS 32; b) Drilling the hole with auger; c) Pushing TEROS 32 into drilled hole; d) Filling TEROS 32 with water syringe.

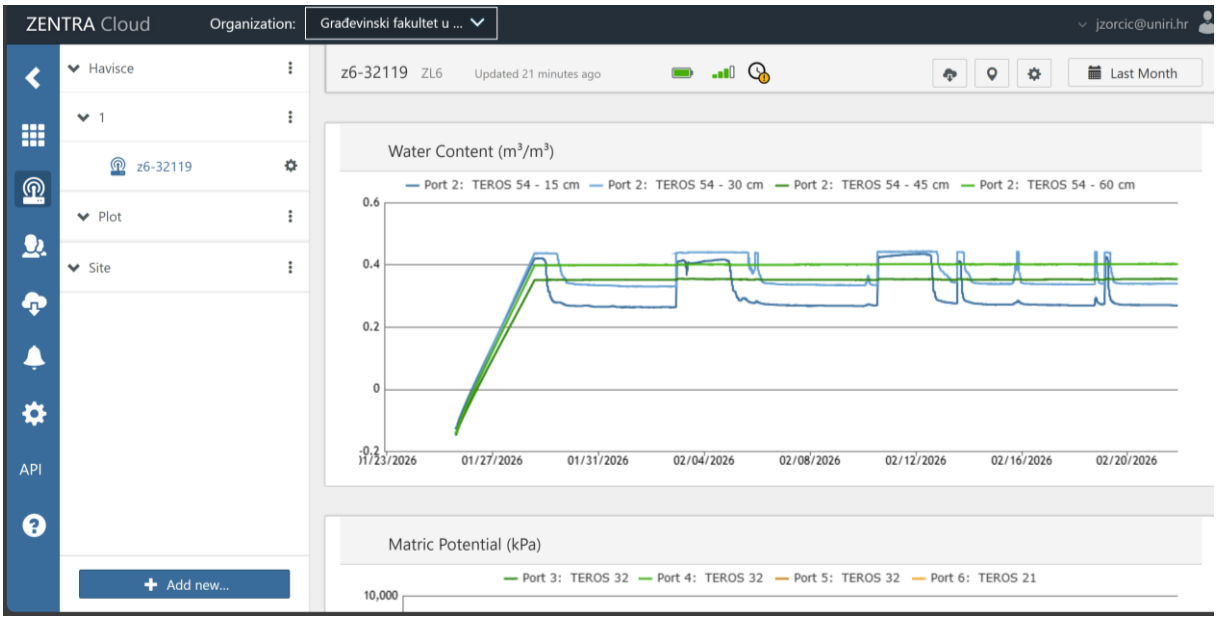

Figure 40 - Data on soil moisture content changes, as seen on ZENTRA Cloud service (top); and data logger ZL6 with all the instruments connected (bottom).

With the monitoring system installed (Figure 41), soil sampling for laboratory characterization was carried out in close proximity to the monitoring location. A soil auger for use in soil including stone fragments and soil sampling ring kit (C53 model) by Eijkelpkam were used to check soil conditions in the first 1m depth and to collect intact and disturbed soil samples for further laboratory tests for basic geotechnical soil characterization.
The samples were taken at the same depths as the TEROS 32 sensors were set at, 15,30 and 60 cm, in order to ensure consistency between field measurements and laboratory analyses. Some details on sample collection are reported in Figure 42.


Figure 41 - Sampling and monitoring location in Havišće Bay.

Figure 42 - Some details on collection of soil samples.

3.3.2. Laboratory testing

In the laboratory, soil characterization tests were carried out. Natural water content was determined immediately after the sampling, using the previously provided equation. Grain size distribution was determined by sieving and hydrometer method. Furthermore, the Atterberg limits (the plastic limit and the liquid limit) of the sampled soil were determined. The specific gravity was also determined using a pycnometer method.

3.3.2.1. Grain Size Distribution Analysis

The grain size distribution of the soil was determined by sieve analysis using the wet method with sieves of 32, 16, 8, 4, 2, 1.18, 0.8, 0.6, 0.425, 0.2, 0.1, and 0.063 mm openings. Representative sample was washed through the sieve stack to remove fine particles adhering to coarser grains. The material retained on each sieve was then dried in an oven overnight at constant temperature of 104°C and its mass was determined after. The percentage retained and percentage passing were calculated for each sieve, and the grain size distribution curve was constructed. The results obtained are provided in Tables 12 to 14 for the soil samples collected at 15, 30 and 60 cm depth, prespectively.

Table 12 - Grain size distribution for sample at 15 cm depth.

Sieve opening *(mm)*	**Weight of soil retained on sieve** *(g)*	**Weight of soil passing through sieve** *(g)*	**Percent passing** *(%)*
32	0	303,1	100,00
16	19,23	283,87	93,66
8	26,73	257,14	84,84
4	14,74	242,4	79,97
2	9,3	233,1	76,91
1,18	4,76	228,34	75,33
0,8	1,98	226,36	74,68
0,6	1,56	224,8	74,17
0,425	1,76	223,04	73,59
0,2	8,16	214,88	70,89
0,1	9,23	205,65	67,85
0,063	7,98	197,67	65,22

Table 13 - Grain size distribution for sample at 30 cm depth.

Sieve opening *(mm)*	**Weight of soil retained on sieve** *(g)*	**Weight of soil passing through sieve** *(g)*	**Percent passing** *(%)*
32	0	270,03	100,00
16	84,66	185,37	68,65
8	12,62	172,75	63,97
4	6,68	166,07	61,50
2	4,71	161,36	59,76
1,18	2,32	159,04	58,90
0,8	2,08	156,96	58,13
0,6	1,68	155,28	57,50
0,425	2,72	152,56	56,50
0,2	6,04	146,52	54,26
0,1	6,74	139,78	51,76
0,063	4,88	134,9	49,96

Table 14 - Grain size distribution for sample at 30 cm depth.

Sieve opening *(mm)*	**Weight of soil retained on sieve** *(g)*	**Weight of soil passing through sieve** *(g)*	**Percent passing** *(%)*
32	0	269,02	100,00
16	0	269,02	100,00
8	8,4	260,62	96,88
4	3,45	257,17	95,60
2	3,87	253,3	94,16
1,18	2,7	250,6	93,15
0,8	1,98	248,62	92,42
0,6	0,97	247,65	92,06
0,425	0,78	246,87	91,77
0,2	1,69	245,18	91,14
0,1	2,68	242,5	90,14
0,063	2,4	240,1	89,25

For particles under 63 microns (0,063 mm) method of hydrometer analysis was used. The test is based on the principle of sedimentation, where soil particles suspended in water settle at different velocities depending on their size. Soil is mixed with dispersing agent and water to form a suspension in a cylinder. Hydrometer readings are taken at predetermined intervals to measure the density of the suspension. As particles settle density of the suspension decreases. From these measurements fine portion of grain size distribution are calculated, and complete grain size distribution curve can be constructed. Cumulative grain size distribution curves are shown in Figure 43.

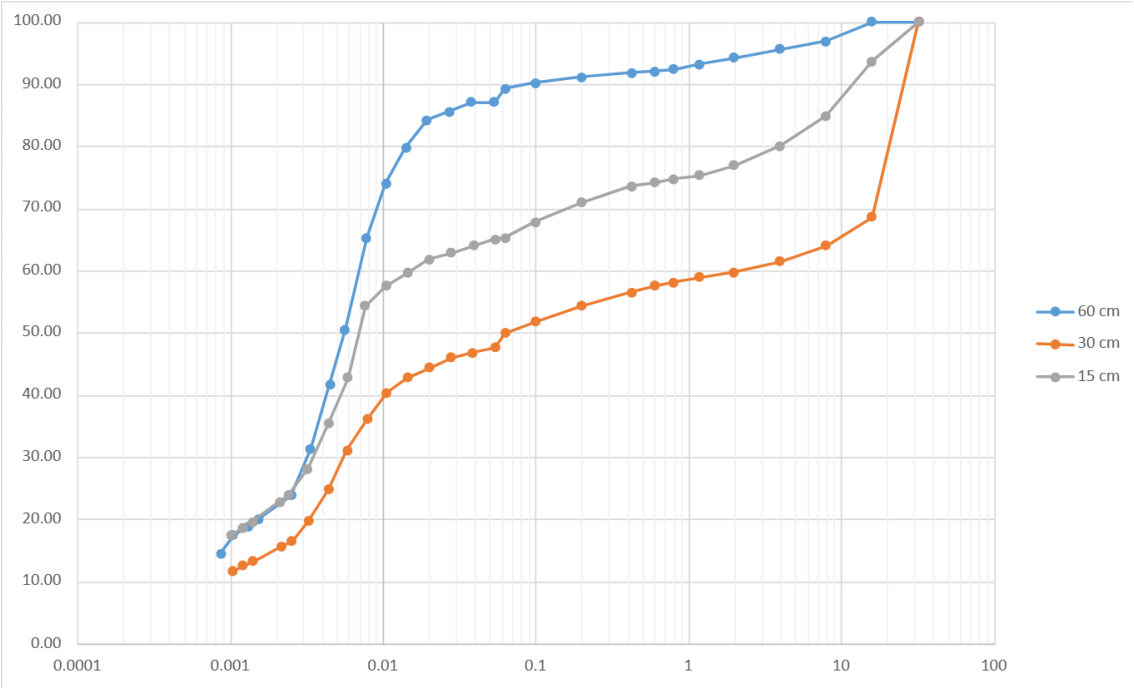

Figure 43 - The cumulative grain size distribution curves.

3.3.2.2. Atterberg limits

Liquid limits were determined using liquid limit device shown in Figure 44. Procedure was done following ASTM standard D 4318 – 05. Soil paste is prepared from soil that passed through 0,425 mm sieve and applied to the cup using a spatula after which groove is formed in the soil by drawing the grooving tool through the middle of the soil. Cup is lifted and dropped by the device at rate of 2 drops per second until the two halves of the soil come in contact along a distance of 13 mm.


Figure 44 - The liquid limit device.

Number of drops, *N*, required to close the groove is recorded and slice of soil is sampled, weighted and oven dried overnight to determine the water content. Procedure was repeated total of 5 times for different number of blows required to close the groove, between 15 to 30 blows. Relationship between the water content, *W*, and number of drops, *N*, is plotted on a

semilogarithmic graph. Straight line is drawn through the plotted points. Water content value at 25-drops is taken as a liquid limit of the soil and rounded to the nearest whole number. According to the liquid limit graphs reported in Figures 45 to 47, the liquid limits is 45% for the soil at 15 cm depth, 44% for 30 cm depth, while at 60 cm depth, the soil's liquid limit of 42% was determined.

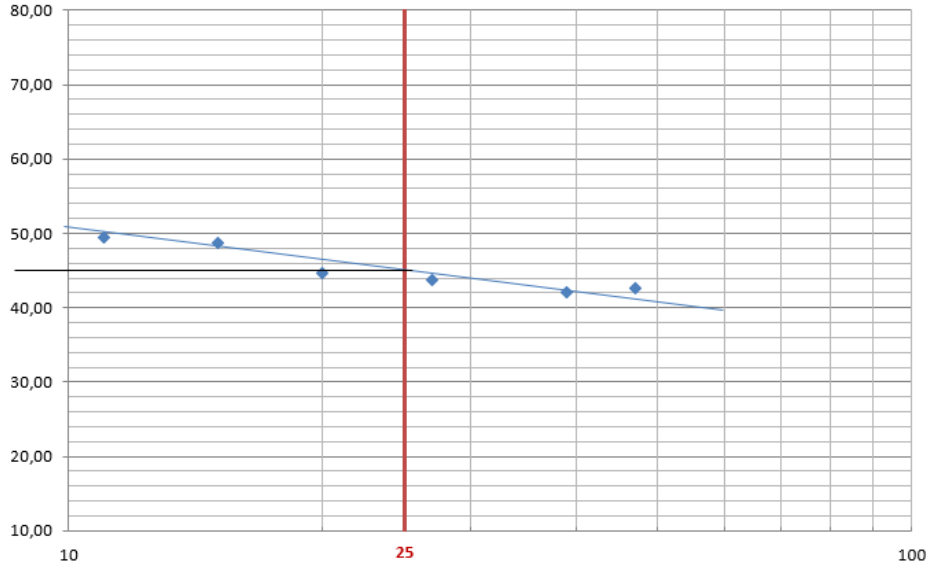

Figure 45 - Liquid limit graph for soil at 15cm depth.

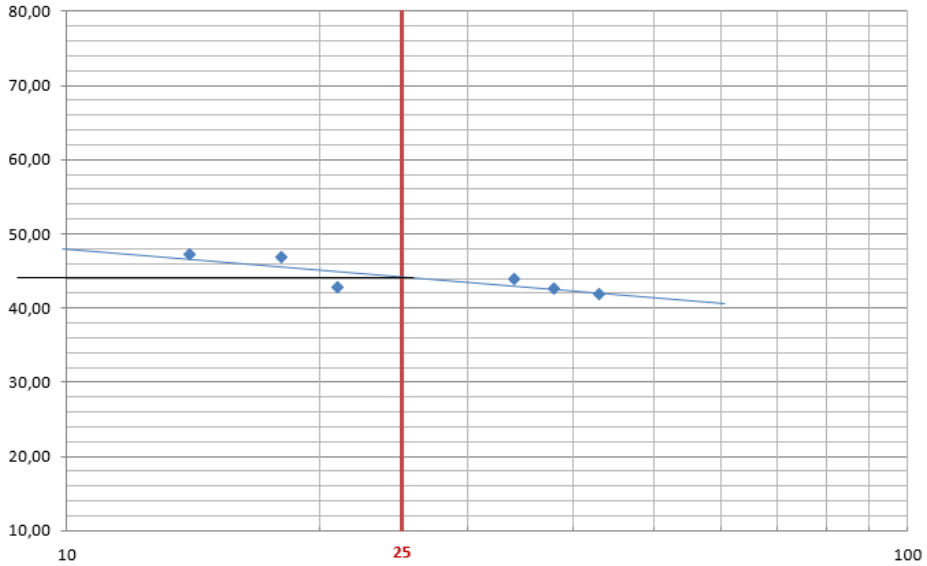

Figure 46 - Liquid limit graph for soil at 13cm depth.

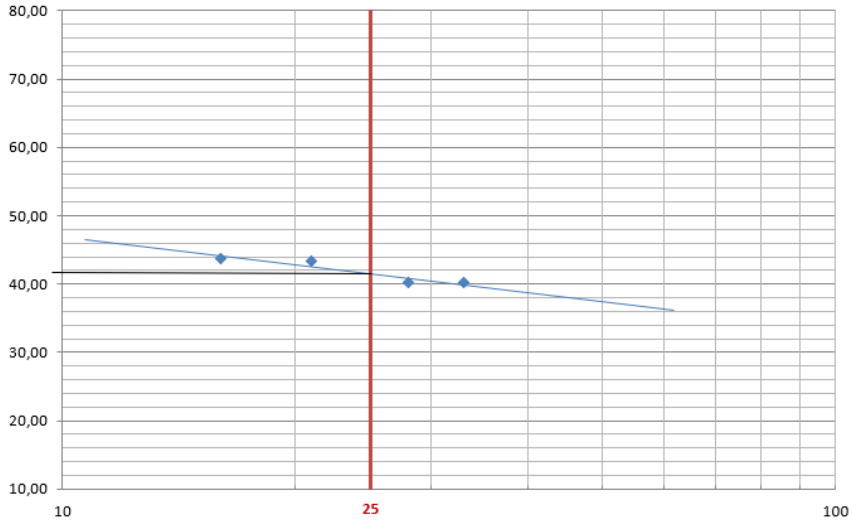

Figure 47 - Liquid limit graph for soil at 60cm depth.

Plastic limits were determined following again ASTM D4318 – 05 procedure. Soil mass was rolled using hand method between palm and glass pane with enough pressure to deform it so that its diameter reaches 3.2 mm. Procedure was repeated until thread of soil broke at 3,2 mm diameter and couldn't be rolled further (Figure 48), procedure was repeated for five samples with two of those, representing the minimum and maximum values, being excluded from the analysis. Plastic limits for soils at each depth are as follows: for 15 cm depth 26%, for 30cm depth 20% and for 60 cm depth 22%.


Figure 48 - Rolling of soil mass thread for plastic limit determination.

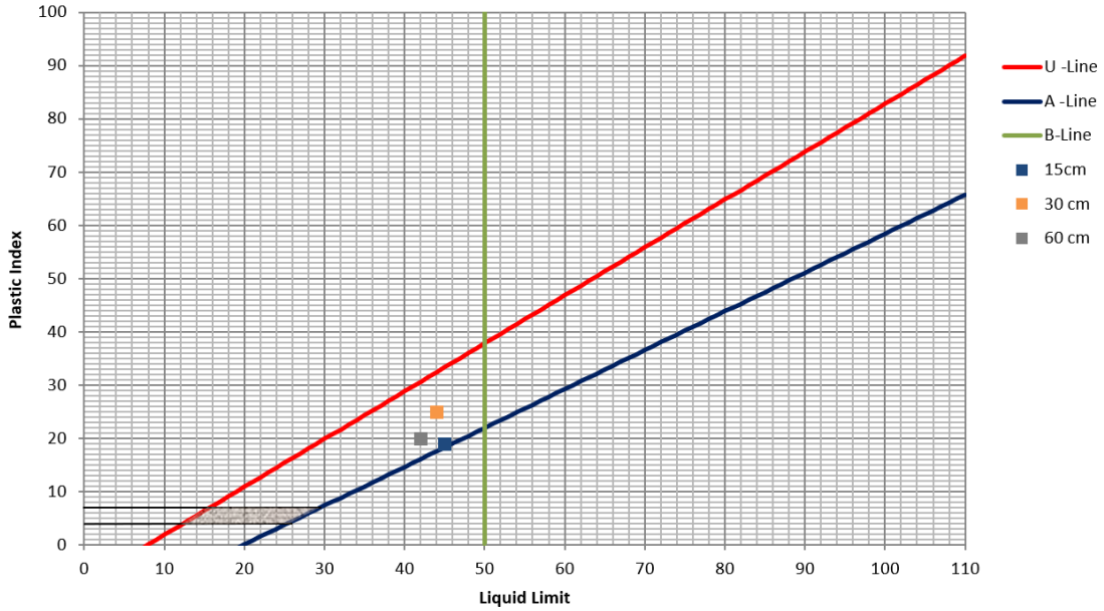

Figure 49 - Casagrande's plasticity chart.

With liquid and plastic limits determined, plasticity index was calculated and the points were added to the Casagrande's plasticity chart (Figure 49). Plasticity index for samples taken at depth of 15 cm is 19, at depth of 30 cm is 24 and at depth of 60 cm is 20.

Table 15 - Atterberg limits for tested soil depths.

Depth*(cm)*	**LL**	**PL**	**PI**
15	45	26	19
30	44	20	24
60	42	22	20

3.3.2.3. Specific gravity

The specific gravity was determined, in accordance with ASTM standard D854 – 23, by water displacement method using pycnometer. Prior to testing, the pycnometers used were calibrated using the vacuum method for deairing the test water. Representative test specimen was 50 g of oven-dry soil for each soil sampling depth. Material used was passed through a sieve with 0,425 mm openings. Some test details are provided in Figure 50.

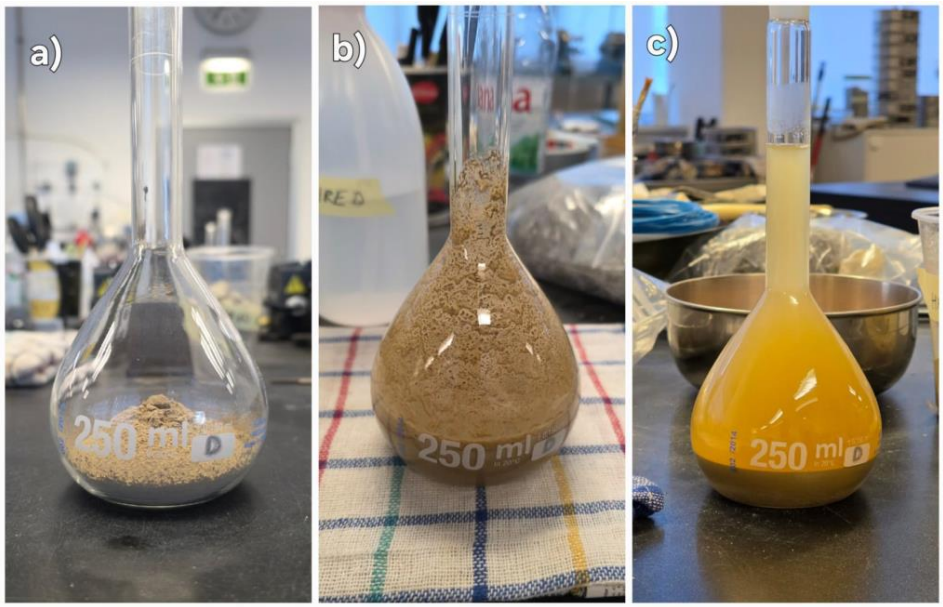

Figure 50 - a) Dry sample in pycnometer; b) Preparing the soil slurry; c) Deaired slurry and equilibrated to constant temperature.

The specific gravity of the solid particles was calculated to be 2.55 for 15 cm depth, 2.58 for 30 cm depth and 2.60 for 60 cm, showing an increasing trend with depth. This trend may indicate minor variations in soil composition within the profile, such as reduced organic content at greater depths.

3.4. Slope stability analyses for the Havišće test site

Slope stability analyses were performed using the GeoStudio software suite (GeoStudio 2023, GeoStudio by Seequent, a Bentley company). The analyses incorporated two modules:

- SLOPE/W – for Limit Equilibrium Method (LEM) analyses, and
- SIGMA/W – for Finite Element Method (FEM) and Shear Strength Reduction (SSR) analyses.

The representative cross-section used for modelling corresponds to the profile along which detailed geophysical investigations were conducted, indicated in Figure 35. The depth to the contact between the competent bedrock and the overlying weathered colluvial soil was determined from geophysical survey results (found to be approximately at 5 m depth) and introduced explicitly into the model geometry.
The phreatic surface was defined in accordance with field monitoring data obtained from soil moisture sensors and pore water pressure transducers installed within the slope. Several groundwater scenarios were analysed in order to simulate seasonal variability.
The soil and rock mass properties assigned in the numerical model were derived from laboratory testing results presented earlier in this report, and/or adopted based on documented experience with similar lithological units in nearby locations. Values of the key parameters assigned to each material are reported in Table 16.

Table 16 - Material properties assigned in LEM slope stability analyses.

Color	Name	Slope Stability Material Model	Unit Weight (kN/m³)	Effective Cohesion (kPa)	Effective Friction Angle (°)	Phi-B (°)	Piezometric Surface
	Bedrock	High Strength	26				1
	Soil cover	Mohr-Coulomb	18,5	10	28	15	1

In addition to the previously reported material properties, a initial void ratio of 0.15 and 0.15, Effective elastic modulus of 10 and o.02 GPa were adopted in SSR analyses for the bedrock and soil cover materials, respectively.
Unsaturated soil conditions representing dry scenarios were simulated by defining phreatic lines corresponding to lower groundwater levels and by incorporating increased apparent cohesion values to account for matric suction effects. As soil moisture increases under transient wetting conditions, matric suction is expected to dissipate progressively. Therefore, in the wet scenarios, the contribution of suction-induced apparent cohesion to shear strength was neglected, and only the effective shear strength parameters (c' and ϕ') were assumed to defined the available total soil's shear strength.

3.4.1. Global Stability Analysis – Limit Equilibrium Method (SLOPE/W)

Slope stability was assessed under a range of groundwater conditions representing seasonal variability, as shown in Figure 51.

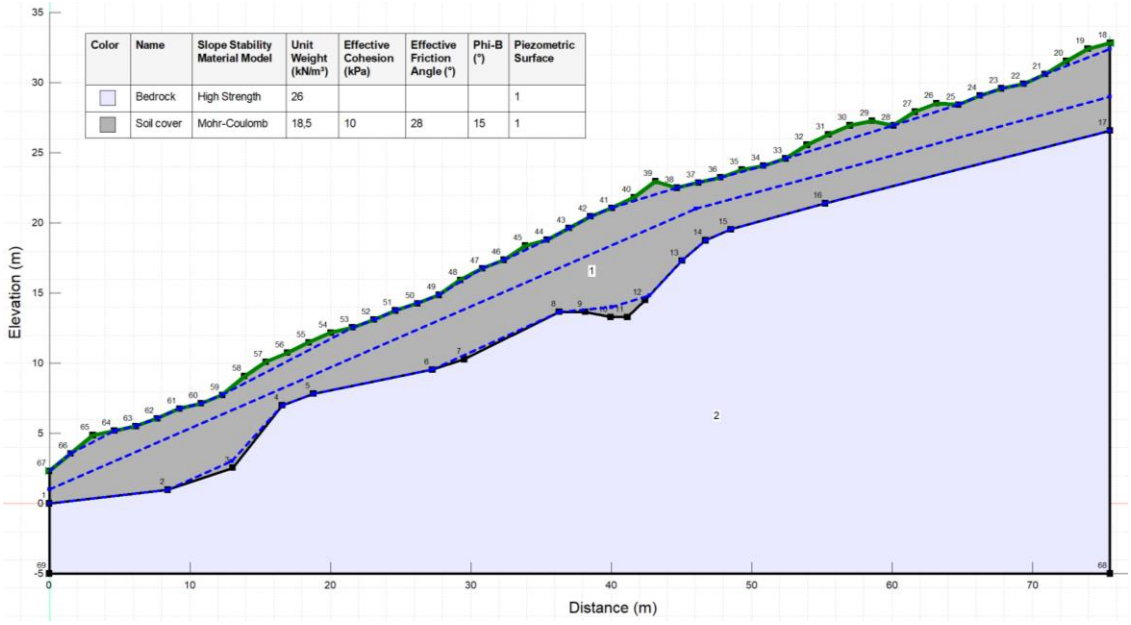

Figure 51 - Piezometric surfaces representing three distinct hydraulic regimes within the slope: dry, intermediate, and wet-season conditions.

The dry season condition is modelled by assuming low groundwater level representative of summer dry periods. The intermediate condition represents the moderately elevated phreatic surface, while the high groundwater level is representative of wet-season conditions and high-intensity and/or prolonged rainfall events, as observed from monitoring data. The phreatic line position was adjusted accordingly in the SLOPE/W and SIGMA/W models to reflect pore water pressure distributions consistent with field measurements.

3.4.2. Results

The LEM analyses were conducted using the Morgenstern–Price calculation method to determine the critical slip surface and corresponding factor of safety (FoS). The results obtained for three different groundwater level scenarios are presented in Figures 52 to 54.

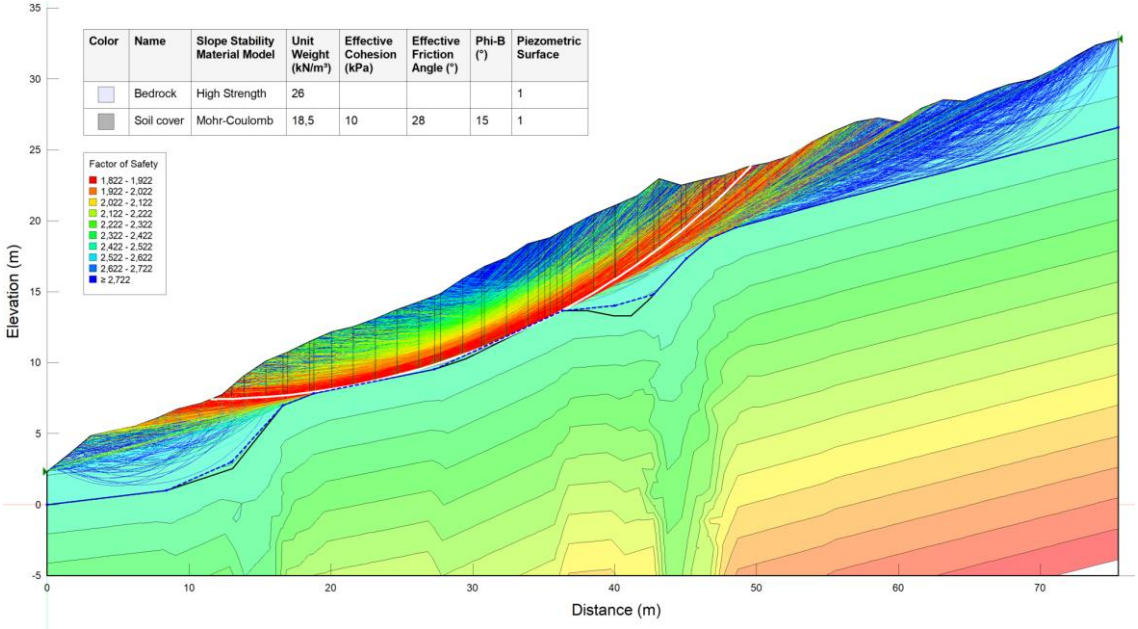

Figure 52 - LEM-based slope stability results for the dry scenario with the critical sliding surface and the corresponding global minimum factor of safety, FoS_{min}=1.82.

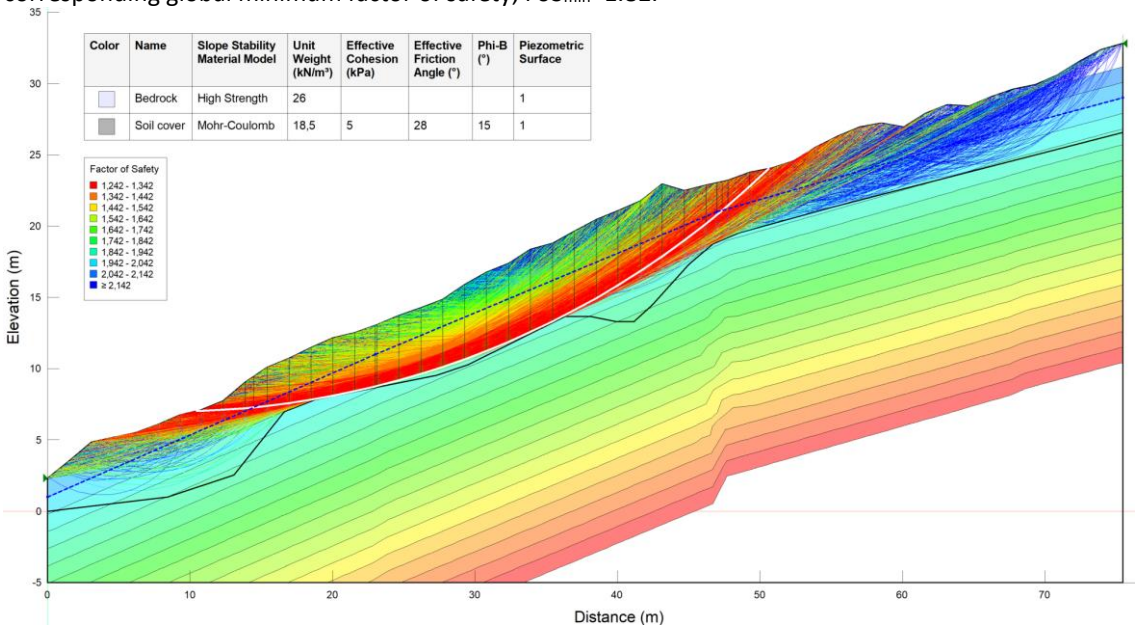

Figure 53 - LEM-based slope stability results for the intermediate scenario with the critical sliding surface and the corresponding global minimum factor of safety, FoS_{min}=1.24.

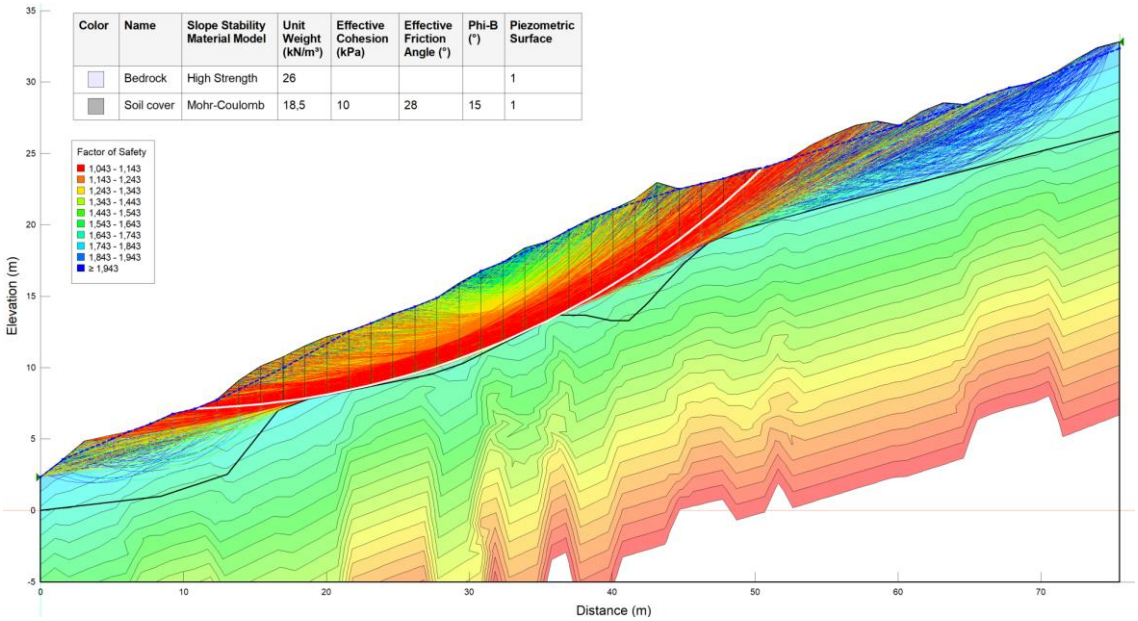

Figure 54 - LEM-based slope stability results for the wet scenario with the critical sliding surface and the corresponding global minimum factor of safety, FoSmin=1.04.

As expected, the results indicate higher FoS values under dry-season conditions due to lower pore water pressures and higher effective stress contributing to the material's shear strength. The results indicated rrogressive reduction of FoS with increasing groundwater level, with a lowest FoS value obtained under fully saturated conditions, corresponding to the wet season and high-intensity rainfall events. However, on the global scale, the slope remains stable even under the most adverse loading condition of high groundwater level and no seismic action.

3.4.3. Shear Strength Reduction Analysis – SIGMA/W

To further assess slope behaviour and failure mechanisms, finite element analyses were performed using the module SIGMA/W and the application of the Shear Strength Reduction (SSR) technique. The method progressively reduces the shear strength parameters (c' and tanϕ') by a predefined Strength Reduction Factor (SRF) until numerical non-convergence is achieved. The SRF at failure is interpreted as the global factor of safety and the result indicate the area where strain localization occurs within the calculation domain, thus outlining the failure mechanism and enabling the estimation of the potential sliding mass volume.
The discretization mesh, applied boundary conditions, and adopted material properties used in the analyses are shown in Figure 55.

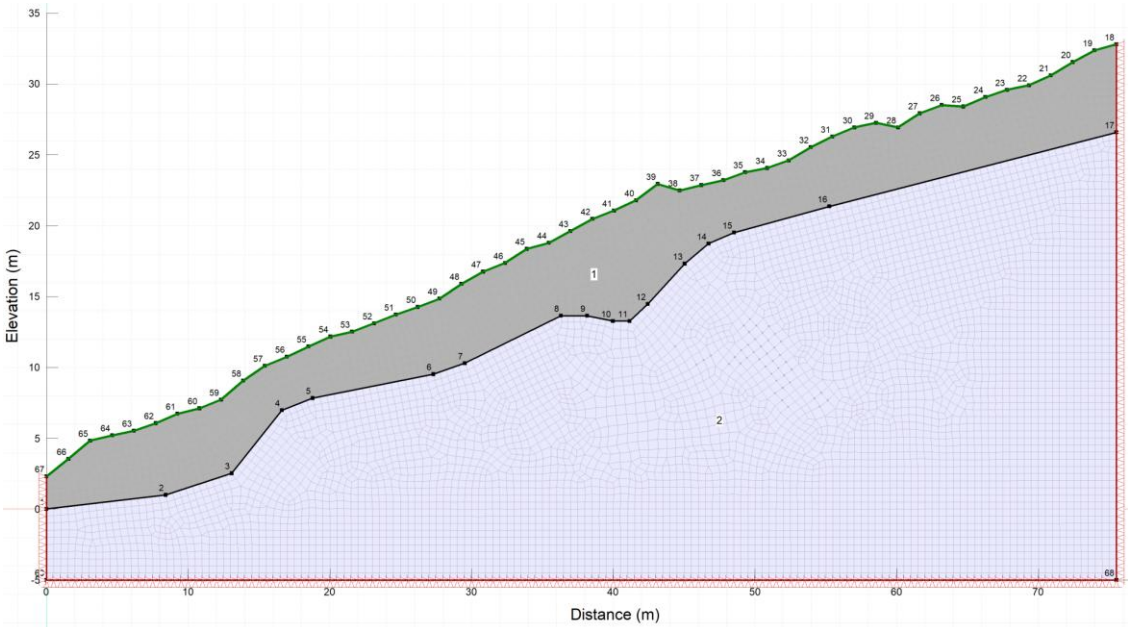

Color	Name	Stress Material Model	Initial Void Ratio	Unit Weight (kN/m³)	Response Type	Effective Elastic Modulus (kPa)	Effective Poisson's Ratio	Effective Cohesion (kPa)	Effective Friction Angle (°)	Dilation Angle (°)	Tensile Strength (kPa)	K0 Type	K0	Sat Kx (m/sec)
	Bedrock	Mohr-Coulomb	0,15	26	Drained	10.000.000	0,21	2.000	30	5	100	Calculated	0,5	1e-14
	Soil cover	Mohr-Coulomb	0,45	18,5	Drained	20.000	0,3	10	28	0	0	Calculated	0,5305	6e-06

Figure 55 - The FEM model built in SIGMA/W: discretization mesh, applied boundary conditions, and adopted material properties used in the SSR analyses.

3.4.4. Results

As shown in Figure 56, the SSR analyses identified zones of maximum shear strain concentration corresponding to potential sliding surfaces predicted by the LEM analyses.

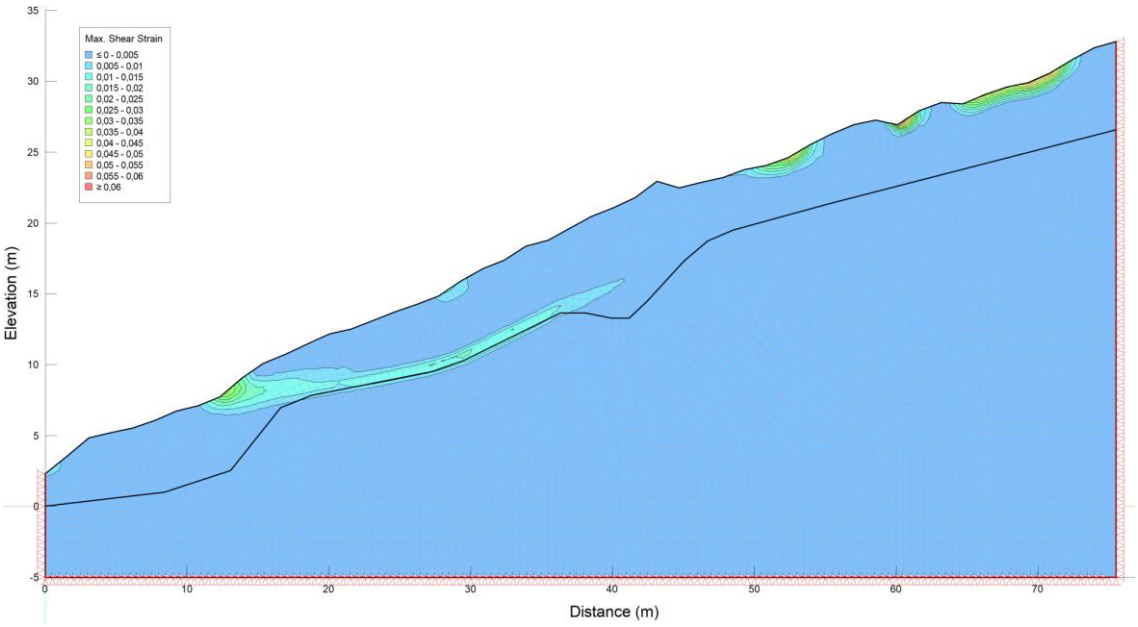

Figure 56 - The results of the SSR analyses in terms of the maximum shear strains.

The predicted failure surfaces are consistent with the stratigraphic contact between the weathered colluvial soil and the underlying bedrock, confirming the mechanical significance of this interface.

3.4.5. Local Toe Stability Analysis

Field evidence of erosion processes affecting the slope toe prompted additional local stability analyses to assess its condition under varying environmental effects. An increase in apparent cohesion under drying conditions (partially-saturated behaviour of porous materials) and a reduction in shear strength during wetting and saturation were considered as the two main mechanisms in the analyses. The results demonstrate that seasonal moisture fluctuations significantly influence shallow stability near the toe region. The base scenario shown in Figure 57 represents dry-period conditions, when increased apparent cohesion is present within the slope.

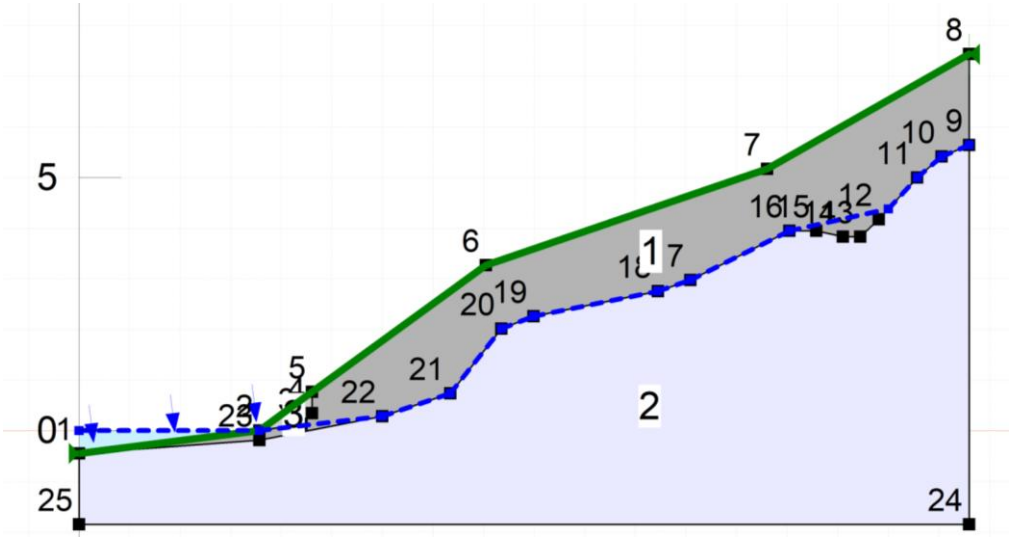

Figure 57 - Base scenario showing piezometric surface and material properties representative of the dry conditions.

3.4.6. Results

The results obtained for the base scenario (Figure 58) suggest stable conditions (FoS=1.46), with the sliding surface corresponding to a minimum FoS typically located at the slope's toe. However, as shown in Figure 59), in case when wetting-induced reduction in apparent cohesion due to groundwater level rise is introduced into the local stability analyses, a small volume of the soil becomes unstable.

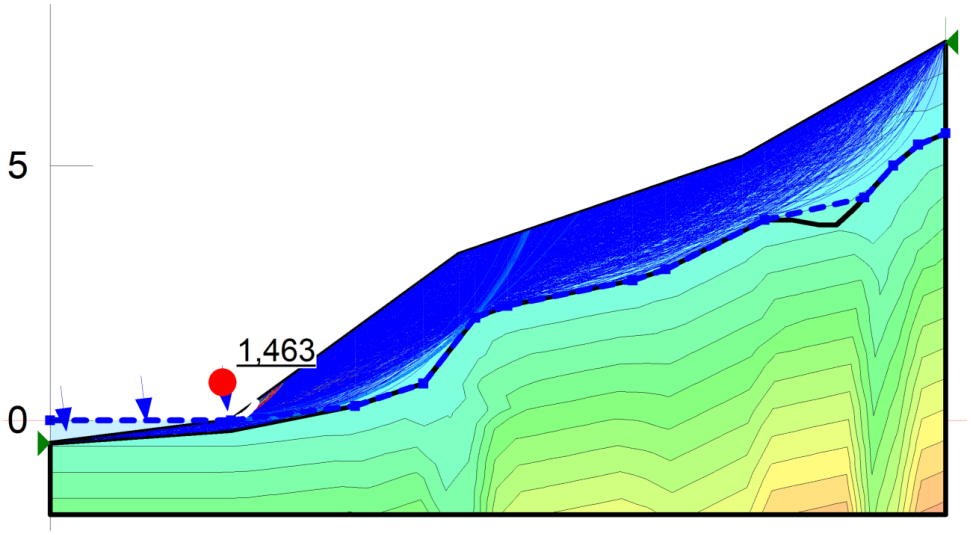

Figure 58 - Base scenario LEM slope stability results indicating stable conditions.

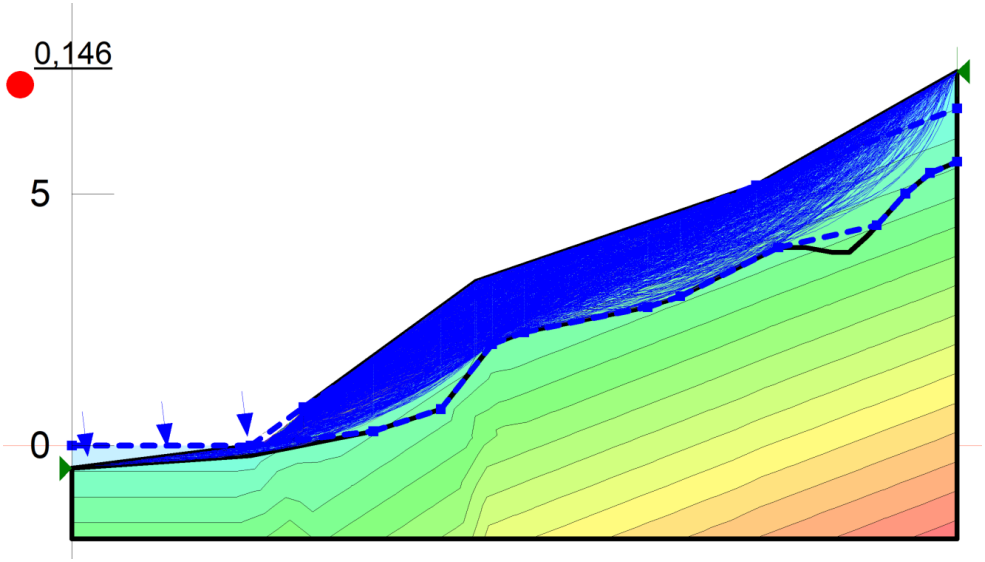

Figure 59 - Shallow instabilities caused by the wetting and the groundwater level rise.

In the next stage, modifications to slope geometry caused by erosion at the toe and wetting-induced reduction in apparent cohesion were incorporated into the model. Progressive removal of support at the toe was simulated to assess its impact on stability. A example is provided in Figure 60.

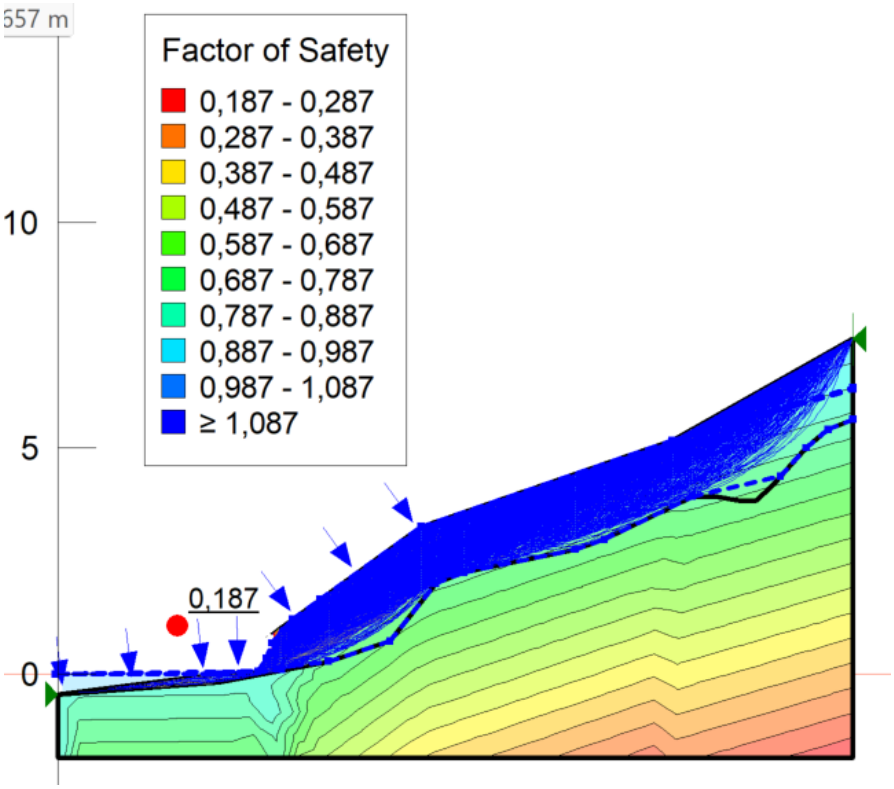

Figure 60 - Slope stability results for the model with modifications to slope geometry simulating the erosion at the toe and wetting-induced reduction in soil strength.

The results indicate that the toe erosion reduces resisting forces, while even minor geometric changes may substantially reduce the local factor of safety. Combined high groundwater levels and toe erosion represent the most critical scenario.

3.4.7. Discussion on the slope stability results

While groundwater level variation represents the dominant controlling factor in the slope stability analyses, the results obtained for the Havišće test site indicate that the slope remains globally stable even under the most adverse hydraulic conditions, including the scenario in which the groundwater level reaches the slope surface. However, the calculated factor of safety for this worst-case condition and working assumptions on material properties—excluding earthquake-induced seismic loading—is very low and only marginally above 1.0, indicating that the stability margin is minimal and that the system is highly sensitive to additional destabilizing influences.

In the context of climate change, which is expected to increase both the intensity and the frequency of climatic forcing and extreme boundary conditions, the stability of the slope may be further challenged. Increased variability in hydrological conditions is likely to accelerate the weathering and degradation of the slope-forming materials, resulting in progressive reductions in their available shear strength. In particular, more frequent dry–wet cycles and larger fluctuations between dry and moist conditions can induce repeated internal stress changes within the material. As indicated by the local slope stability analyses, progressive removal of material from the slope face leads to increasing deviatoric stresses at the slope toe, facilitating further erosion and gradual upslope retreat of the slope face.

Field monitoring data further indicate that the stabilizing effect of previously accumulated eroded material at the slope toe is diminishing due to increasingly frequent extreme sea-level events. When combined with strong wave action capable of reaching progressively higher elevations along the slope face, this process contributes to intensified toe erosion. The interaction of these mechanisms significantly jeopardizes the global stability condition of the slope over the long term.

To evaluate potential mitigation measures, an additional numerical model was developed incorporating a concrete wall constructed at the slope toe together with drainage elements behind the wall, as shown in Figure 61. The structural element is designed to reduce the direct impact of wave action and limit the increase in soil moisture in the toe zone, while the drainage system aims to lower the groundwater level in the lower part of the slope. The modelling results clearly indicate a beneficial structural support effect and a measurable improvement in the stability condition of the slope (Figure 61, right), reflected in increased factors of safety compared to the unprotected scenario.

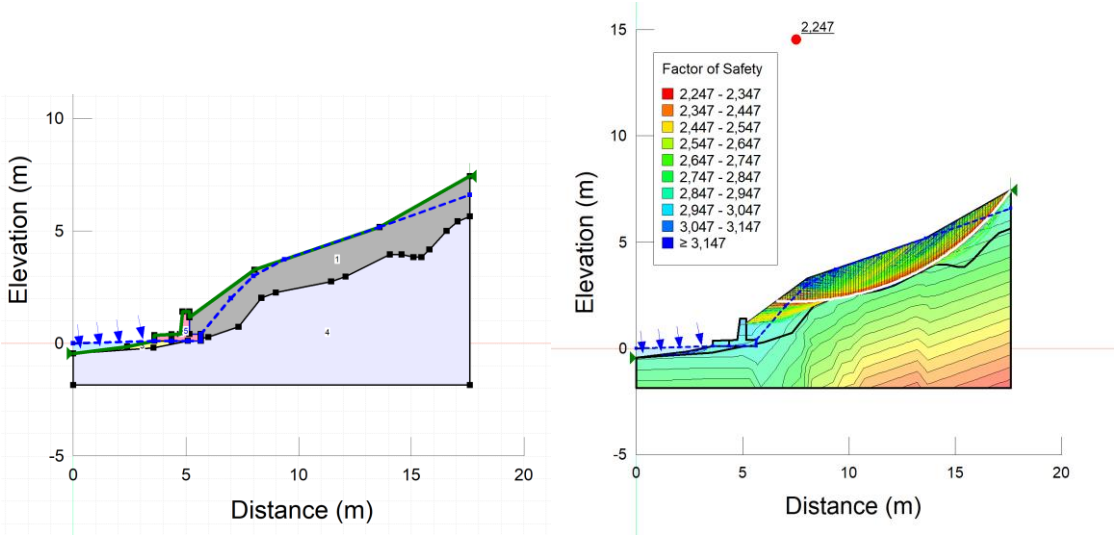

Figure 61 - Numerical model incorporating a concrete wall and drainage elements: geometry (left) and slope stability analysis results (right).

Nevertheless, the analyses also highlight several limitations associated with relying on a single structural measure such as a concrete wall for long-term slope protection. Groundwater level increases, especially in combination with extreme sea-levels may still affect the soil mass behind the wall, reducing shear strength and potentially generating unfavourable pore pressure conditions. Furthermore, projected climatic conditions—characterized by prolonged dry periods followed by extreme rainfall events and cyclone-driven storm surges—are likely to intensify the frequency and amplitude of drying–wetting stress cycles within the slope material. These processes may also increase the erodibility of materials beneath or adjacent to the protective concrete elements, potentially undermining their long-term effectiveness.

Consequently, while the proposed toe protection system provides a significant improvement in slope stability and represents an important mitigation measure, it cannot be considered a fully sufficient solution when implemented in isolation. Addressing the long-term impacts of climate change on coastal slope stability requires a comprehensive and integrated approach that combines structural protection measures, improved drainage management, continuous monitoring, and detailed evaluation of additional stabilization strategies. Further

investigations and more advanced modelling of potential adaptation measures will therefore be essential for developing a robust and sustainable protection concept for the site.

4. Brovinje site

4.1. Introduction

4.1.1. Location and geological context of the Brovinje site

According to the geological map of the Republic of Croatia (CGI, 2009), the pilot area was built in flysch deposits of the middle and upper Eocene (Figure 62). Eocene flysch deposits were discovered in the area of central and northern Istria, in the Croatian coastal area, the islands of Krk, Rab and Pag, and further south in some other areas as far as Dubrovnik and Konavle. The red circle on the map indicates the Brovinje bay.

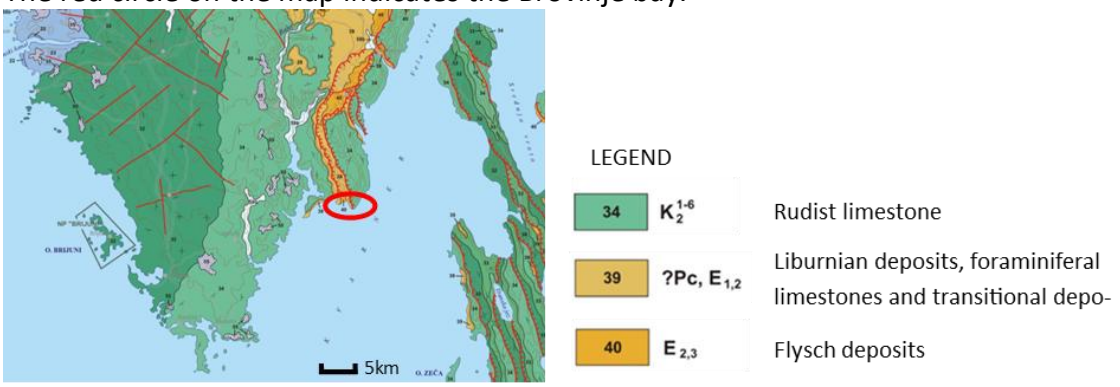

Figure 62 - Brovinje site (red oval) at the geological map (Geological map of the Republic of Croatia Scale 1:300,000, Croatian Geological Institute, 2009).

Homogeneous marls with variable weathering are present at the foot of the slope (Figure 63). These eroded marl layers are exposed to direct wave impact and marine erosion.

Figure 63 - Alteration of differently discoloured layers of marls a t the foot of the slope.

The middle part of the slope consists of the previously mentioned marl layers, covered by thin residual soil and colluvium, which are forested, while the top of the slope is formed by a limestone plate (Figure 64).

Figure 64 - View of the slope at the Brovinje site.

4.1.2. Geophysics input data

The geophysical investigation allowed the characterization, with metric resolution, of the surface portion of the subsoil in terms of thickness and resistivity providing useful subsurface geological information. Geophysical investigation performed in November 2024 involved the acquisition of 4 geoelectrical profiles at the Brovinje site. The geoelectric profiles were acquired using different interelectrode distances (Δx).

According to the Geophysical report-II-semestre-PP2, (CNR-ISPC, 2025), the electrical resistivity tomography (ERT) profile n°4 has shown a heterogeneous subsoil with interruptions caused by fractures. The high resistive layer rests on a low resistive layer and the black dashed line at 38 meters depth could be the limit of a slip surface (Figure 65).

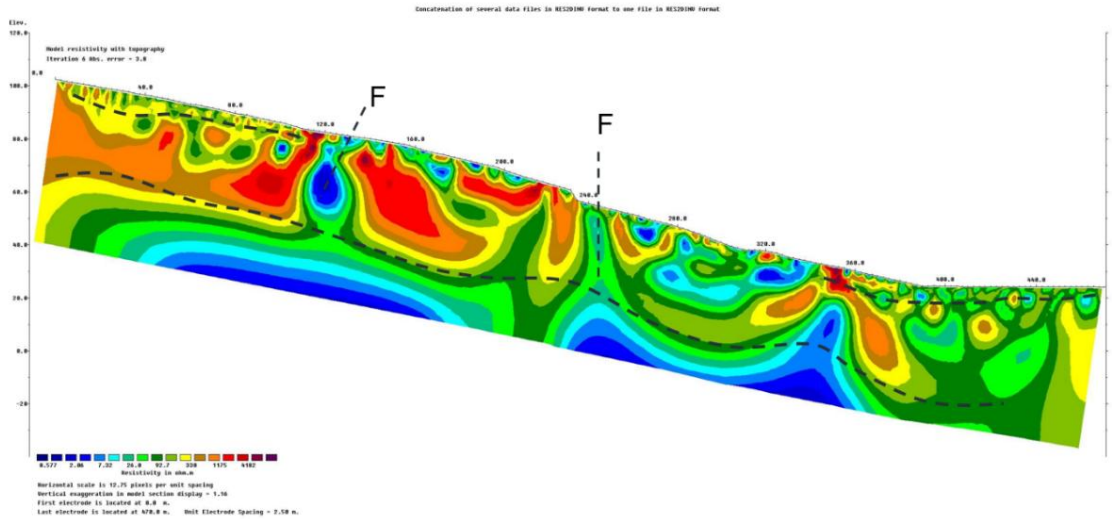

Figure 65 - Position of the geoelectrical profile n°4 at the Brovinje site and 2D distribution of the resistivity.

4.1.3. Laboratory testing input data

Samples at the Brovinje site taken for the laboratory testing present homogeneous marls containing microcrystalline calcite aggregates. Slight discolouration can be seen on major discontinuity surfaces of marl samples, while some marl samples show superficial discolouration indicating the beginning of weathering processes (Figure 63). In the geotechnical laboratory in 2025, Uniaxial Compressive Strength (UCS) testing was carried out on a PLT device and the moisture content of the tested marl samples was determined. PLT testing was carried out on marl samples of natural humidity.

According to geotechnical report on the testing of marl samples on Brovinje site (GRADRI, 2025), mean UCS at natural humidity of the marl samples taken at Location 1 was 39.16 MPa, and of the one taken from Location 2 (superficially changed in colour) was 54.96 MPa. Both groups of samples have similar UCS, regardless the slight superficial discoloration.

4.2. Slope stability analyses

The role of climate change in slope instabilities was applied in terms of the material weathering and increase of sea level in the Slide2 program (Rocscience Inc, Canada, version 9.028), using the Bishop's simplified method of slices (Bishop, 1955).

Slope stability analyses were performed at the surface profile obtained from the digital terrain model (DTM) of Brovinje with 1 m resolution created from UAV photogrammetry through this RESONANCE project or obtained by the Croatian State Geodetic Administration (Figure 66).

Figure 66 - Position of the longitudinal profile on the orthophoto map for slope stability analyses at Brovinje site.

4.2.1. Results of slope stability analyses

Marls that form the Brovinje site and the investigated slope, according to the obtained data and geological rock mass description, were defined using the Generalized Hoek-Brown criteria (Hoek, Carranza-Torres, Corkum, 2002) with the RSData program (Rocscience Inc, Canada, version 1.007). The program provides tables used to estimate the uniaxial compressive strength of an intact rock element (σ_{ci}), the material constant (m_i) and the geological strength index (*GSI*).

The input parameters used for calculating the strength parameters of the marls were used from the location 1 and 2 as follows:

	Location1	Location2
- the uniaxial compressive strength of an intact rock, σ_{ci}	54 MPa	39 MPa
- the material constant, m_i	7	
- geological strength index, *GSI*	35	25
- disturbance factor, *D*	0	

GSI determined for the heterogenous rock mass such as flysch rock mass accruing to Marinos and Hoek (2000) is defined in accordance with Figure 67. It was used the GSI with value of 35 for marls at location 1 and 25 at location 2.

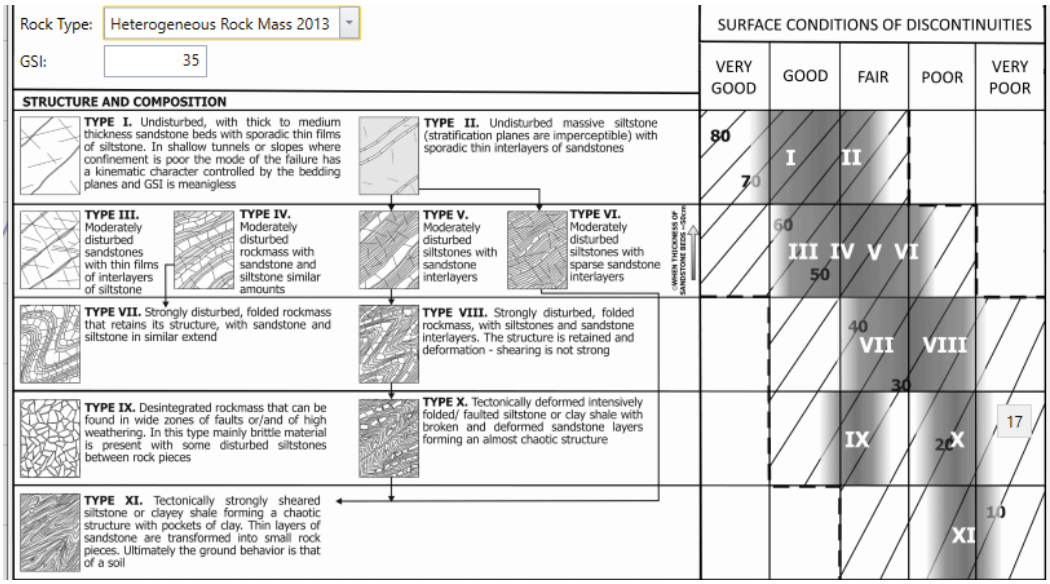

Figure 67 - GSI for heterogeneous rock masses such as flysch (Marinos and Hoek, 2000).

According to Hoek-Brown criterium, equivalent Mohr-Coulomb cohesion and friction angle were calculated in the RocData program, Figure 68.

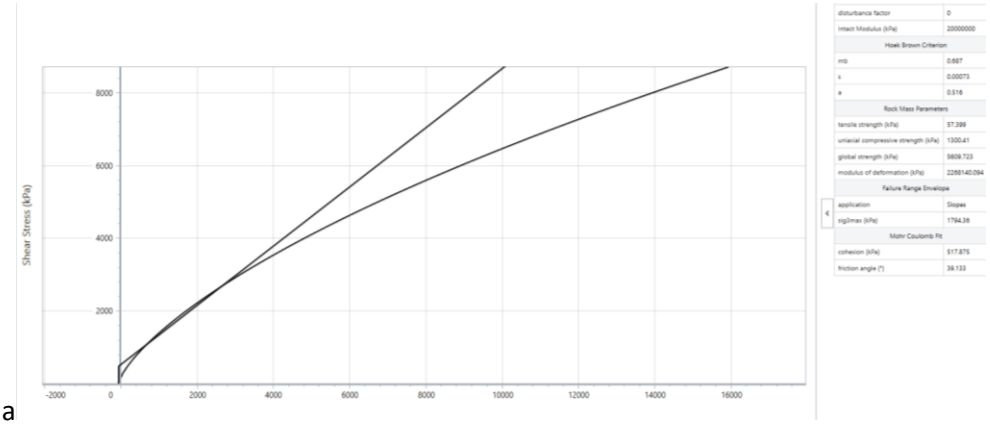

a

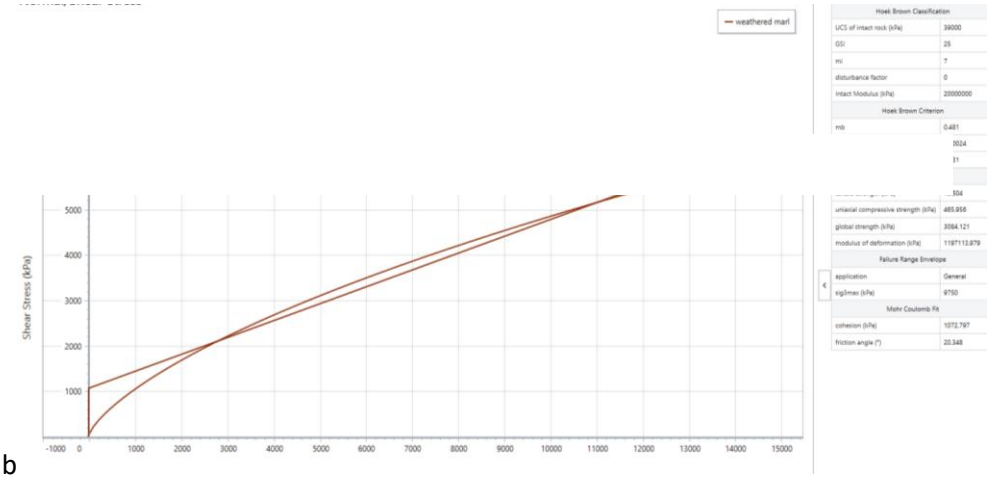

b

Figure 68 - Hoek Brown criterion and fitted Mohr-Coulomb envelope for marls at a) location 1 and b) location 2.

Based on the described input data, results of performed slope stability analyses in Slide2 program, are given below. Figure 69 shows slope model of a slope built in marls with properties at a) location 1 and b) location 2 for overall slope profile.

a

Color	Unit Weight (kN/m3)	Strength Type	UCS (intact) (kPa)	Parameters vary with depth	GSI	mi	D	Water Surface	Hu Type	Hu
	23	Generalized Hoek-Brown	54000	No	35	7	0	Water Table	Custom	1

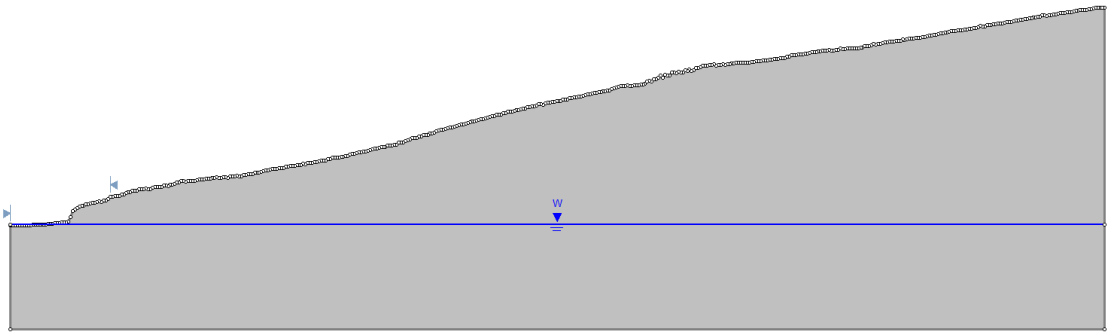

b

Material	Color	Unit Weight (kN/m3)	Strength Type	UCS (intact) (kPa)	Parameters vary with depth	GSI	mi	D	Water Surface	Hu Type	Hu
		23	Generalized Hoek-Brown	39000	No	25	7	0	Water Table	Custom	1

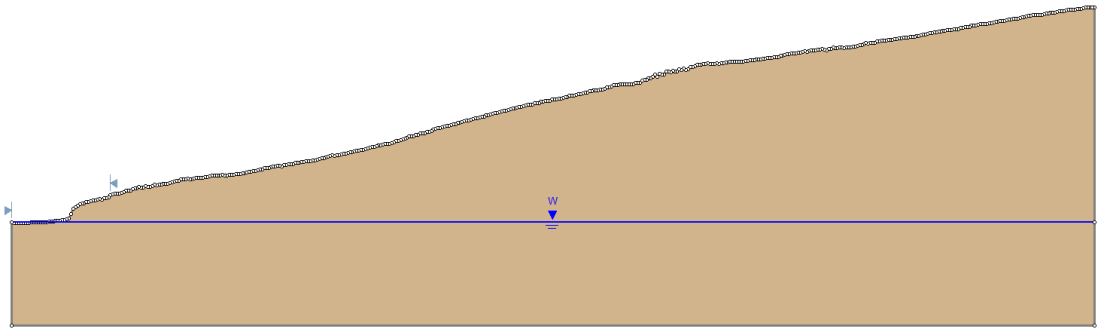

Figure 69 - Slope model with rock mass characteristics in the Slide2 program built in marls of properties at: a) location 1 and b) location 2.

Figures 70 and 71 present the factor of safety for the entire slope and for the foot of the slope in marls of different properties. The factor of safety for the entire slope built in marls with properties at location 1 and location 2 is 6.272 and 4.735 respectively, indicating that the slope is safe regardless of the superficial discoloration. Additionally, the factor of safety at the foot of the slope in marls with properties at location 1 and location 2 is greater than 1, with values of 7.909 and 4.139, respectively, indicating that the slope foot is also stable.

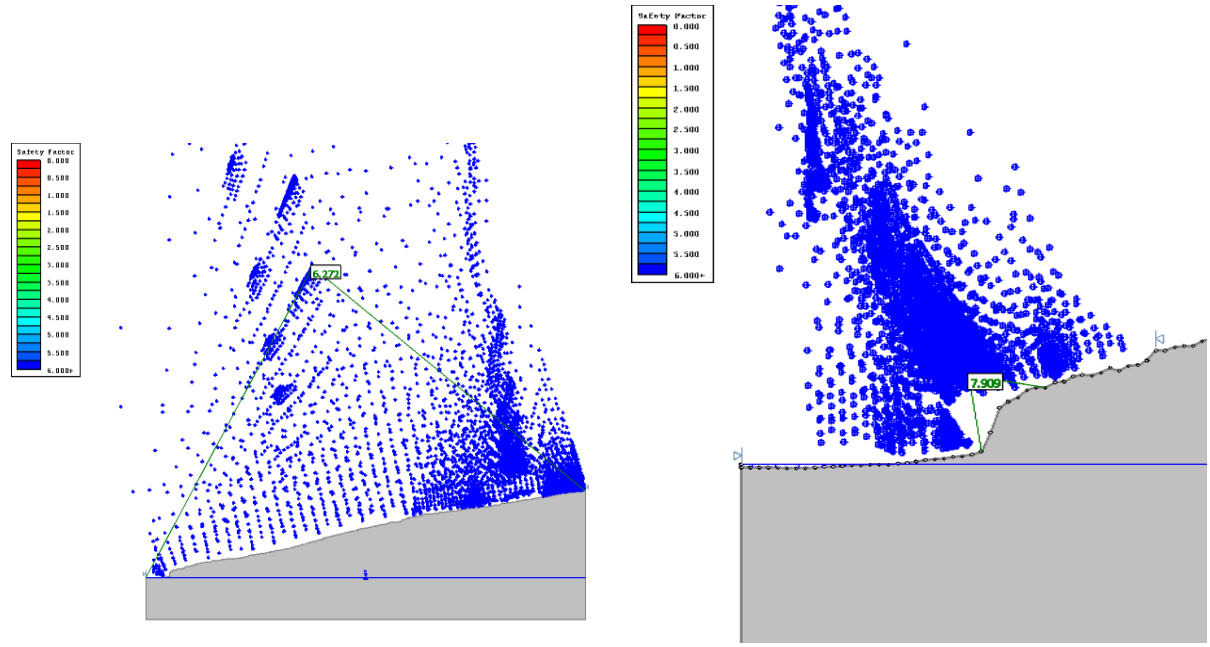

a b

Figure 70 - Factor of safety obtained in the Slide2 program of the slope built in marls with properties at location 1 a) for the entire slope, b) at the foot of the slope.

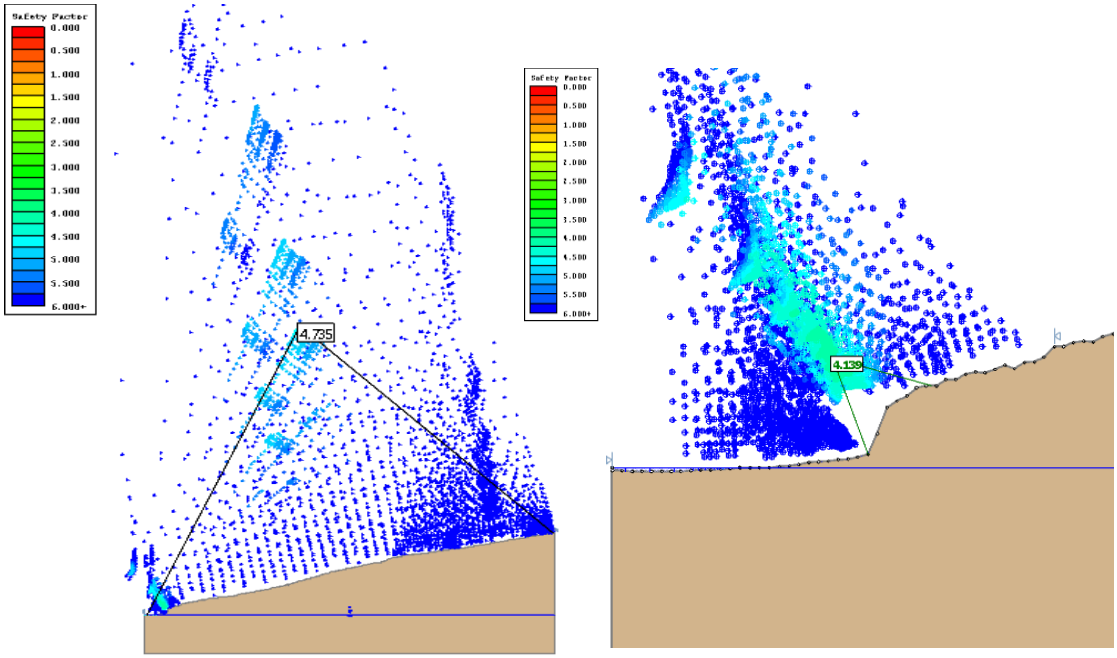

a b

Figure - 71 Factor of safety obtained in the Slide2 program of the slope built in marls with properties at location 2 a) for the entire slope, b) at the foot of the slope.

Slope analysis were also conducted, adopting rock mass with better properties in the deeper part of the slope, while the upper part consists of the marls with lower strength. The predicted boundary between marls of different properties is at 38 metres (Figure 72a), as indicated in the geophysical report for the Brovinje site and the same slope profile. Results of the slope analyses for slopes composed of marls with different properties through depth are shown in

Figure 72b, indicating that the slope with varying strength of marls is also stable, with a factor of safety of 6.814.

Color	Unit Weight (kN/m3)	Strength Type	UCS (intact) (kPa)	Parameters vary with depth	GSI	mi	D
	23	Generalized Hoek-Brown	54000	No	35	7	0
	23	Generalized Hoek-Brown	39000	No	25	7	0

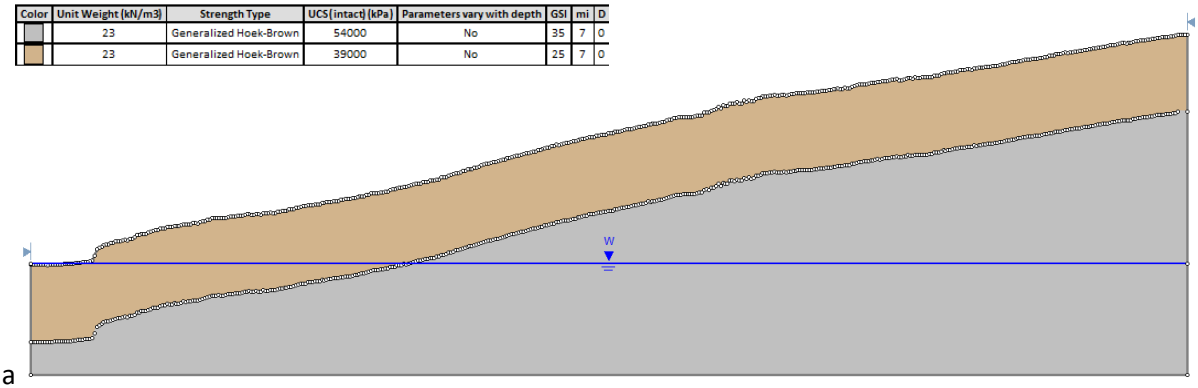

a

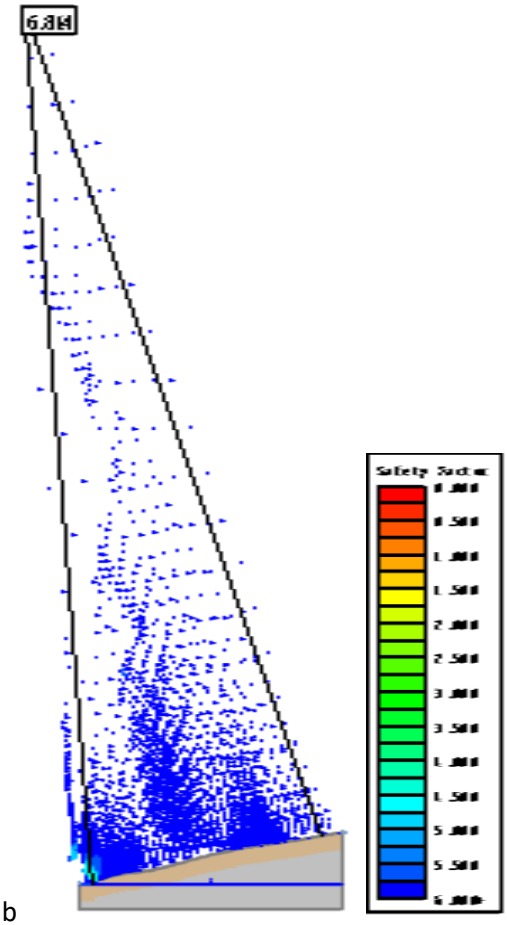

b

Figure 72 - a) Slope model with varying weathering grades of marls and b) factor of safety of the slope obtained in the Slide2 program.

The level of the Adriatic Sea off the coast of Croatia is rising rapidly due to climate change, with estimates of an increase between 40 and 60 cm by the end of the 21st century (https://www.croris.hr/projekti/projekt/5551). Projections for a 1 m sea level rise are provided in further analyses (Figure 73a). The factor of safety is still not affecting on the stability at the slope foot, giving a factor of safety of 4.139 (Figure 73b).

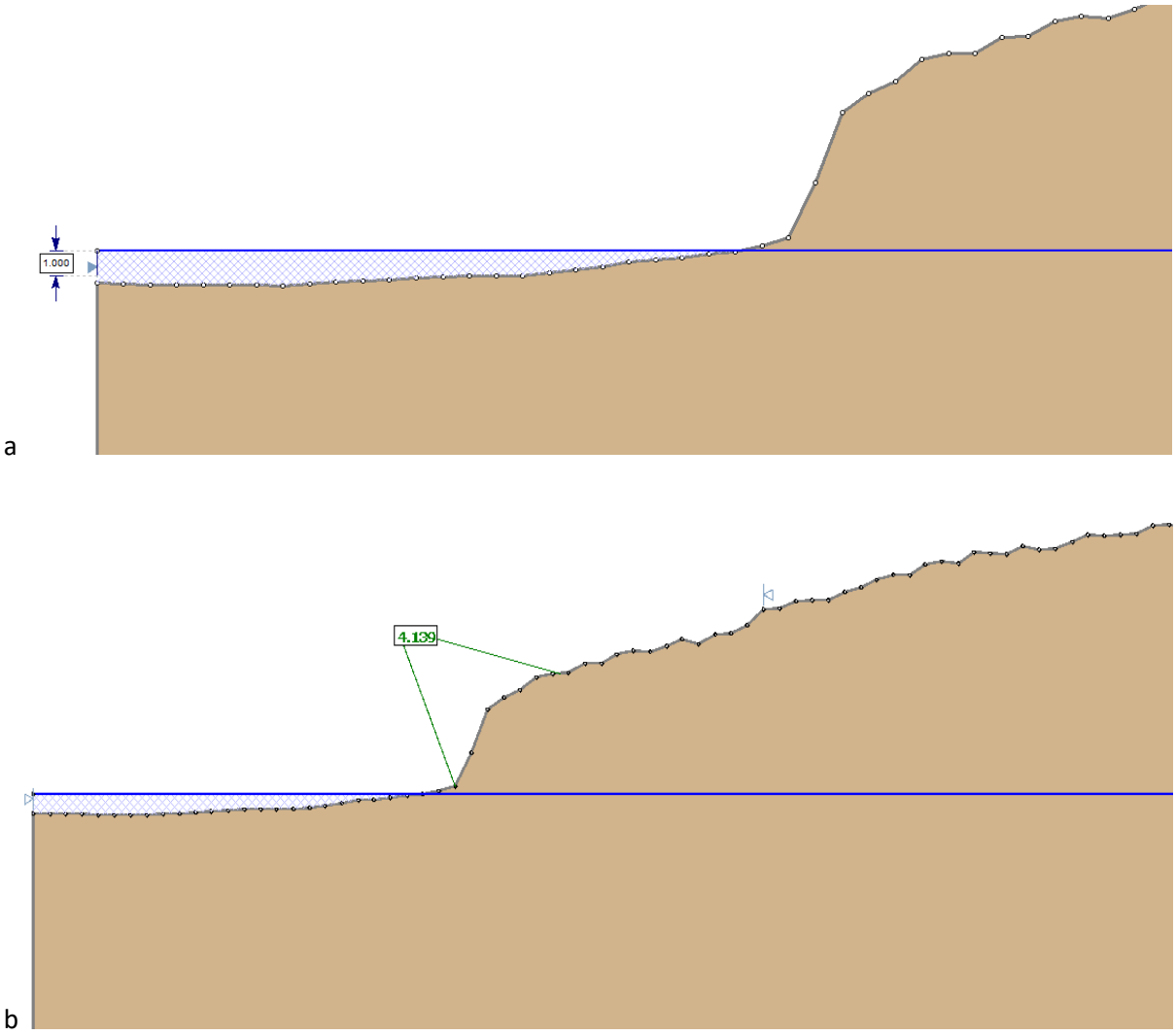

Figure 73 - a) Slope model with increase of sea level for 1 m and b) factor of safety at the foot of the slope obtained in the Slide2 program.

Since the slope stability analyses determined that the slopes built in marls with different properties are stable and there is no risk of sliding, even with a raised sea level, rockfall analyses were conducted and are presented below.

4.3. Rockfall analyses

Blocks of marl, breccia, and limestone are visible at the toe of the slope, on the beach gravel and inside the sea (Figure 74a), as well as in the gully along the slope (Figure 74b), indicating the need to conduct two-dimensional and three-dimensional rockfall analyses.

a 

b 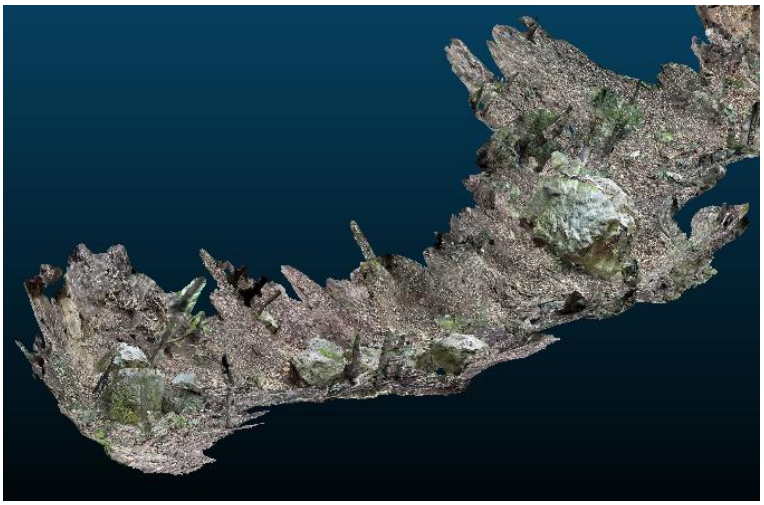

Figure 74 - Marl, breccia and limestone blocks a) at the toe of the slope, b) in the gully along the slope.

Blocks of marl, breccia, and limestone are visible at the toe of the slope, on the beach and inside the sea, posing a high risk of impact to people on the beach, indicating the need to conduct rockfall analyses.

The DTM obtained (Figure 75) with 1 m resolution was used to provide 2D and 3D rockfall analyses in RocFall2 (Rocscience Inc, Canada, version 8.026) and RocFall3 (Rocscience Inc, Canada, version 1.017) software respectively.

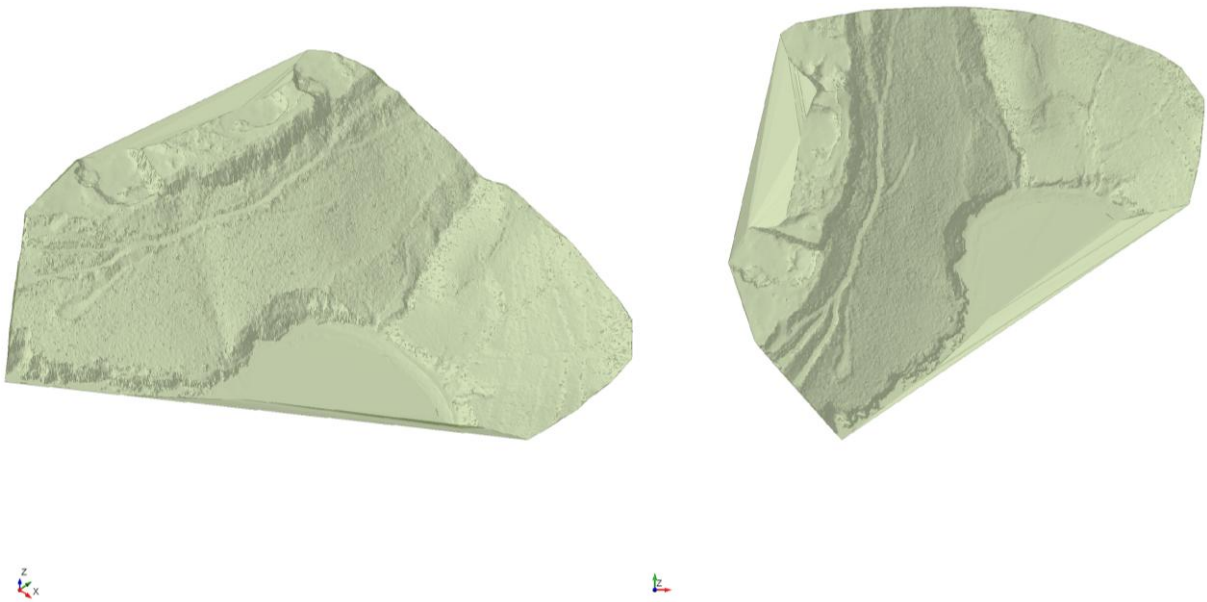

Figure 75 - 3D view of the Brovinje site analysed in the RocFall3 program.

Through seeder definition, the rocks' origin locations and the rocks' initial conditions are specified i.e., velocity, mass, density, and shape. The four types of seeders are available in RocFall3: Point Seeders, Line Seeders, Plane Seeders, and Area Seeders. Line seeders were used to model rocks originating from a line or a polyline. The rock locations were generated with a uniform distribution along the length of the line seeder, i.e., a rock will start falling from any point along the length of the seeder with equal probability. Two types of line seeders were defined in Brovinje model: Seeder1 grouped as limestone blocks falling from the top of the slope (yellow line on Figure 76a) and Seeder 2 grouped as marl blocks falling from the eroded part at the foot of the slope (green line on Figure 76b).

a b

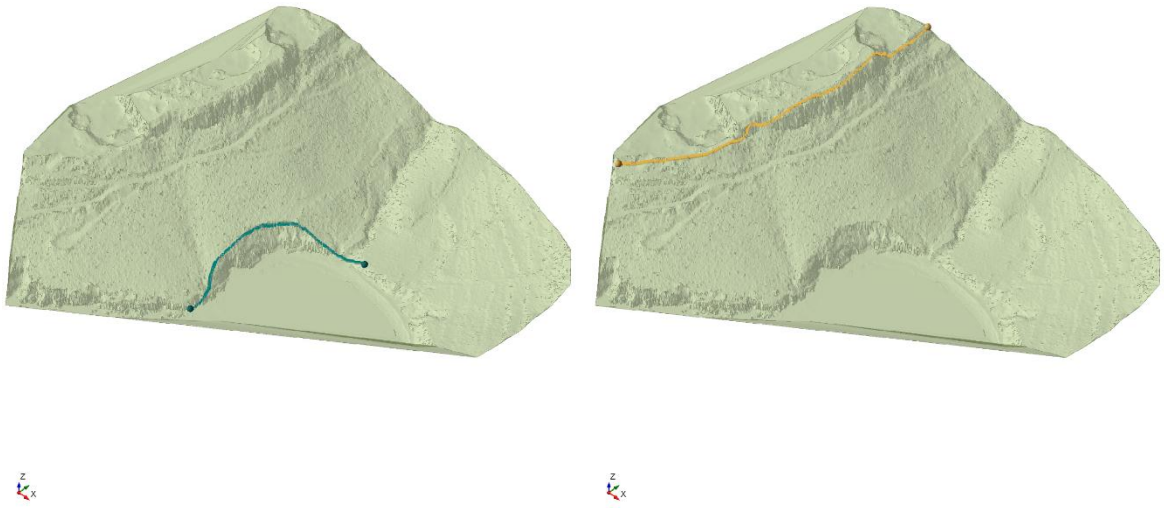

Figure 76 - 3D view of the Brovinje site analysed in the RocFall3 program with two types of seeders: a) Seeder 1 and b) Seeder 2.

One hundred rocks with icosphere shapes and zero initial velocity were specified identically for both rock groups. The following seeder properties: mass and density of the rock, were defined individually for each Seeder group (Table 17).

Table 17 - Seeder properties for two types of seeders: Seeder 1-limestone blocks and Seeder 2-marl blocks.

Seeder n^{o}	Seeder type	Shape	Number of rocks	Initial velocity (m/s)	Mass (kg)	Density (kg/m^{3})
Seeder 1	Limestone blocks	icosphere	100	0	2500	2500
Seeder 2	Marl blocks				1000	2463

Different material properties can be used depending on the or lump mass or rigid body analysis used in program RocFall3. Rigid Body analysis option was used in analysis within the RocFall3 program. The Rigid Body approach considers the impulse reaction of the rock during the instantaneous contact period. The normal and tangential coefficients of restitution are used to calculate the outgoing velocities. From the change in velocity, the impulses at the contact point can be calculated and then the outgoing rotational velocities (Basson, 2012). For Rigid Body analysis, the basic contact parameters are normal restitution and dynamic friction coefficient.

Different material regions (Figure 77) were defined in the model with different normal restitution and dynamic factor coefficients (Figure 78): limestone at the top of the slope, marls covered with vegetation in the middle part of the slope and eroded marls and beach gravel at the foot of the slope and sea.

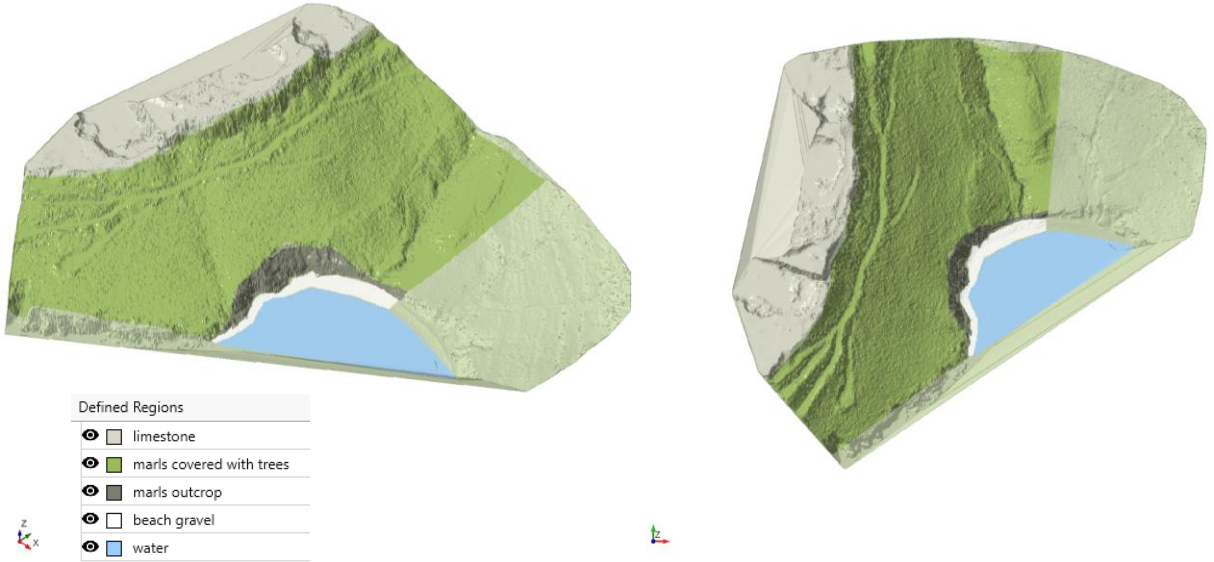

Figure 77 - View of the analysed Brovinje area with different material regions in RocFall3: limestone, marls covered with trees, marls outcrop, beach gravel and water.

Sea, region with water (Figure 78e), is assumed to be fully damping, meaning that any rock contact would immediately cancel the rock's kinetic energy and stop the rock. This is a simplified approach for modelling complete energy loss on rock-slope contact, and no other parameter input was required in the dialog. This option with Lose All Kinetic Energy on Contact may be used to model rock contact with a water body or a highly damping material.

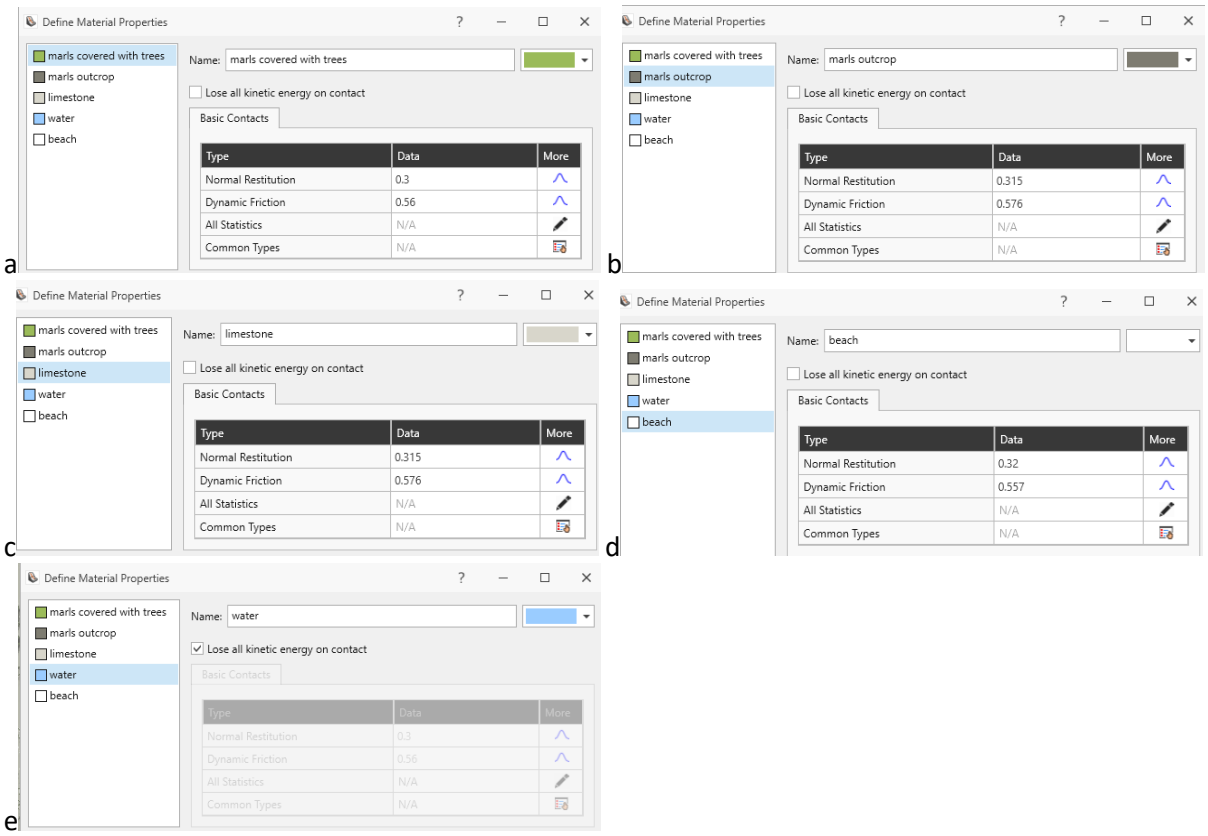

Figure 78 - Material properties in RocFall3 analysis for: a) marls covered with trees, b) marls outcrop, c) limestone, d) beach gravel and e) water.

4.3.1. Results of 3D rockfall analyses

Results of the 3D rockfall analyses for each rock path in both seeders are given below. Rock paths from different seeders are displayed in Figure 79 and are categorized by translational velocity (m/s), total kinetic energy (kJ), runout distance xy (m), and travel time (s). Maximum translational velocity was 27 m/s, kinetic energy exceeded 950 kJ, runout distance was greater than 200 m, and travel time of 30 s was obtained in the analyses.

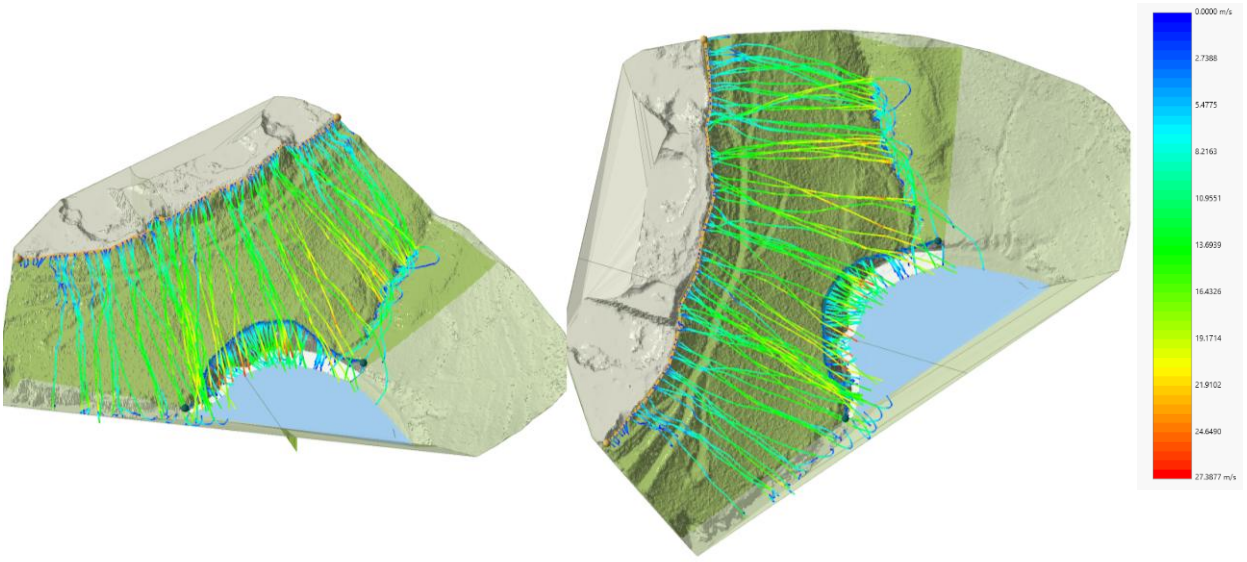
0.0000 m/s
2.7388
5.4775
8.2163
10.9551
13.6939
16.4326
19.1714
21.9102
24.6490
27.3877 m/s

a

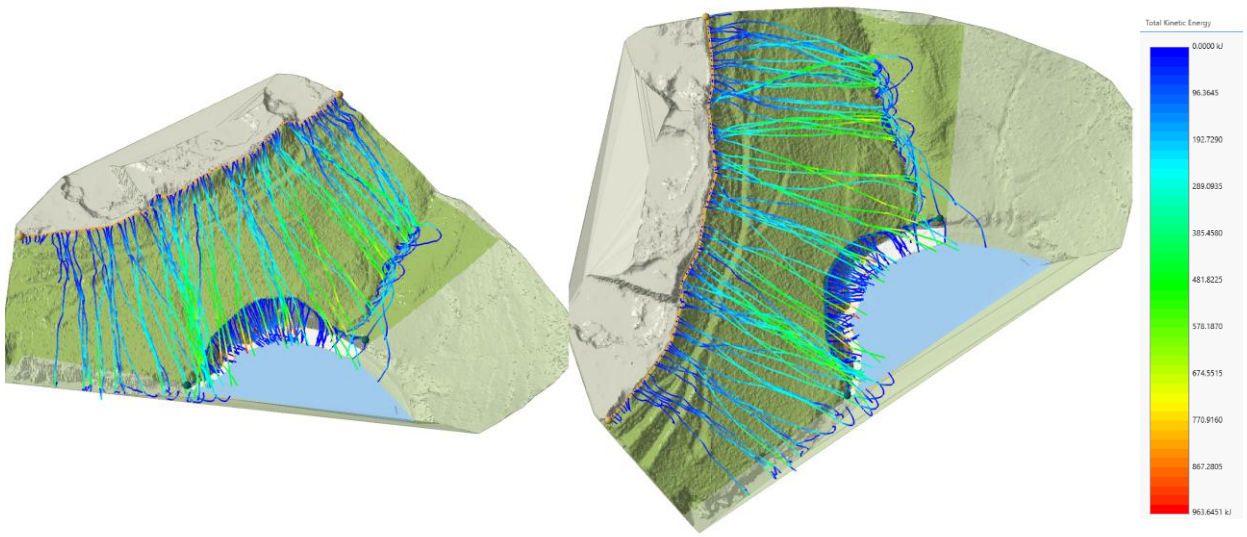
Total Kinetic Energy
0.0000 kJ
96.3645
192.7290
289.0935
385.4580
481.8225
578.1870
674.5515
770.9160
867.2805
963.6451 kJ

b

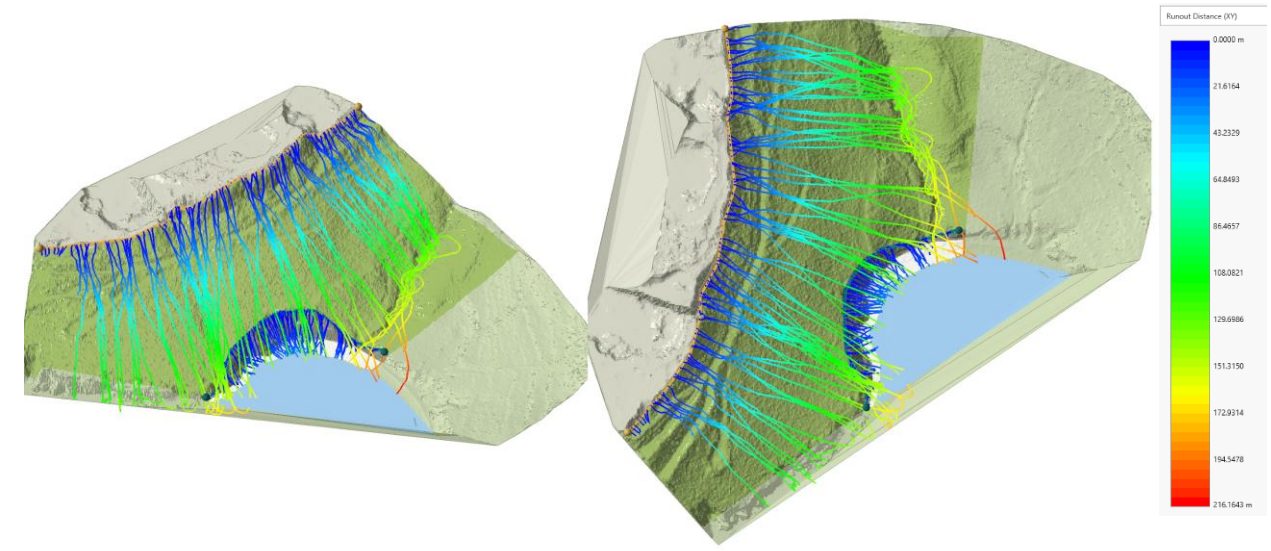

c

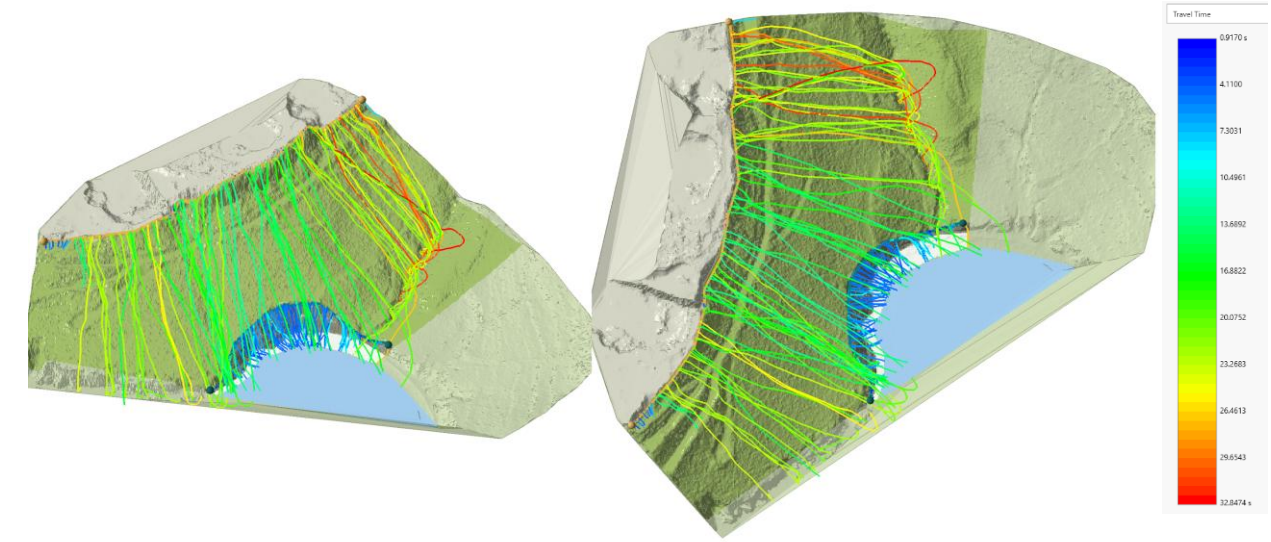

d

Figure 79 - Results of the 3D analyses for each rock path in both seeders with a) different translational velocities (m/s), b) total kinetic energy (kJ), c) runout distance xy, d) travel time.

The heatmap is shown in Figure 80 and is used to quickly identify patterns or trends in a dataset, especially useful when dealing with larger sets of rock paths. The colours of a surface heatmap represent the magnitude of scalar quantities of end points projected onto a slope surface. Each grid displays a colour representing the scalar magnitude of the variable of

interest, in this case the end points (red indicates 28 end points and blue indicates none).

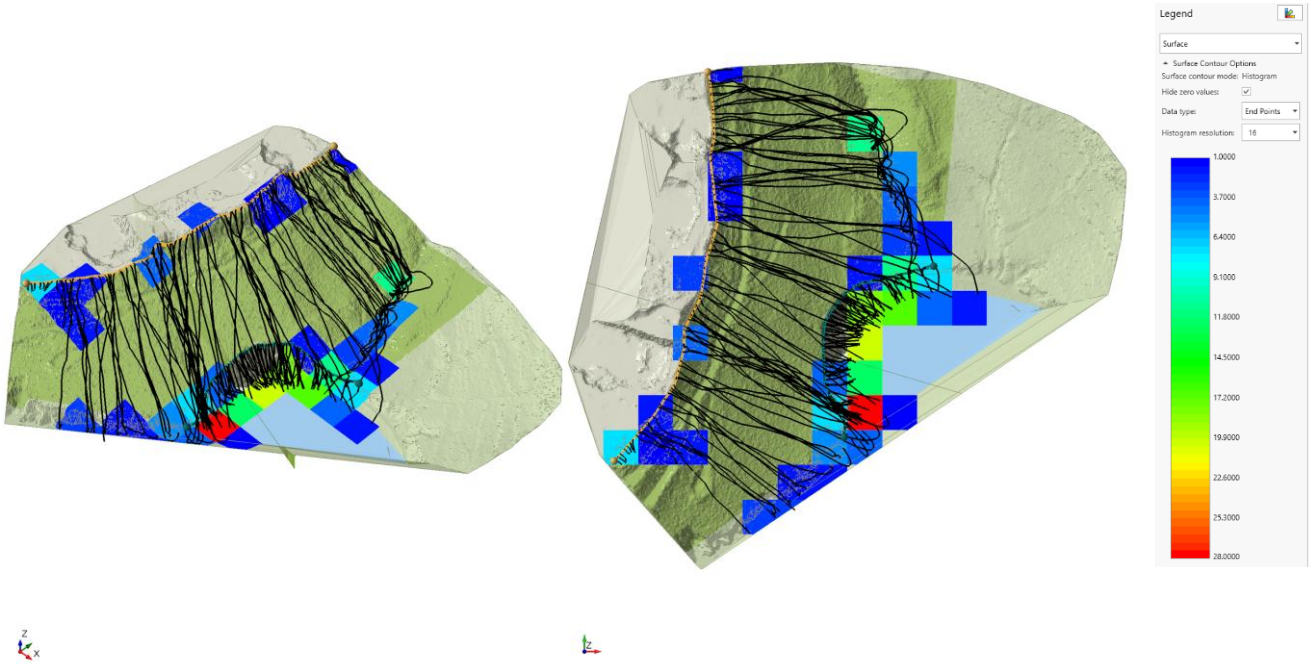

Figure 80 - Heatmap with magnitude of scalar quantities of end points projected on a slope surface.

From the 3D model in RocFall3, a 2D cross section (Figure 81) was extracted and analysed in RocFall2. The model already has three materials (Figure 78) defined in the 3D analysis, as well as seeder properties (Table 17).

Figure 81 - a) 3D model with position of cross section in RocFall3 software, b) cross-section of the model in RocFall2 software showing regions with different material properties and the positions of seeder points.

4.3.2. Results of 2D rockfall analyses

Results of the 2D rockfall analysis for each rock path in both seeders (limestone from the top and marls from the bottom of the slope) are shown in the following figures. Rock paths from different seeders are displayed in Figure 82. Total kinetic energy along the slope is shown in Figure 83, and the rock path end locations are shown in Figure 84a. These results show that the largest percentage of rocks, i.e. 63% of blocks (Figure 84b) have fallen on the beach and in the sea, indicating a significant risk.

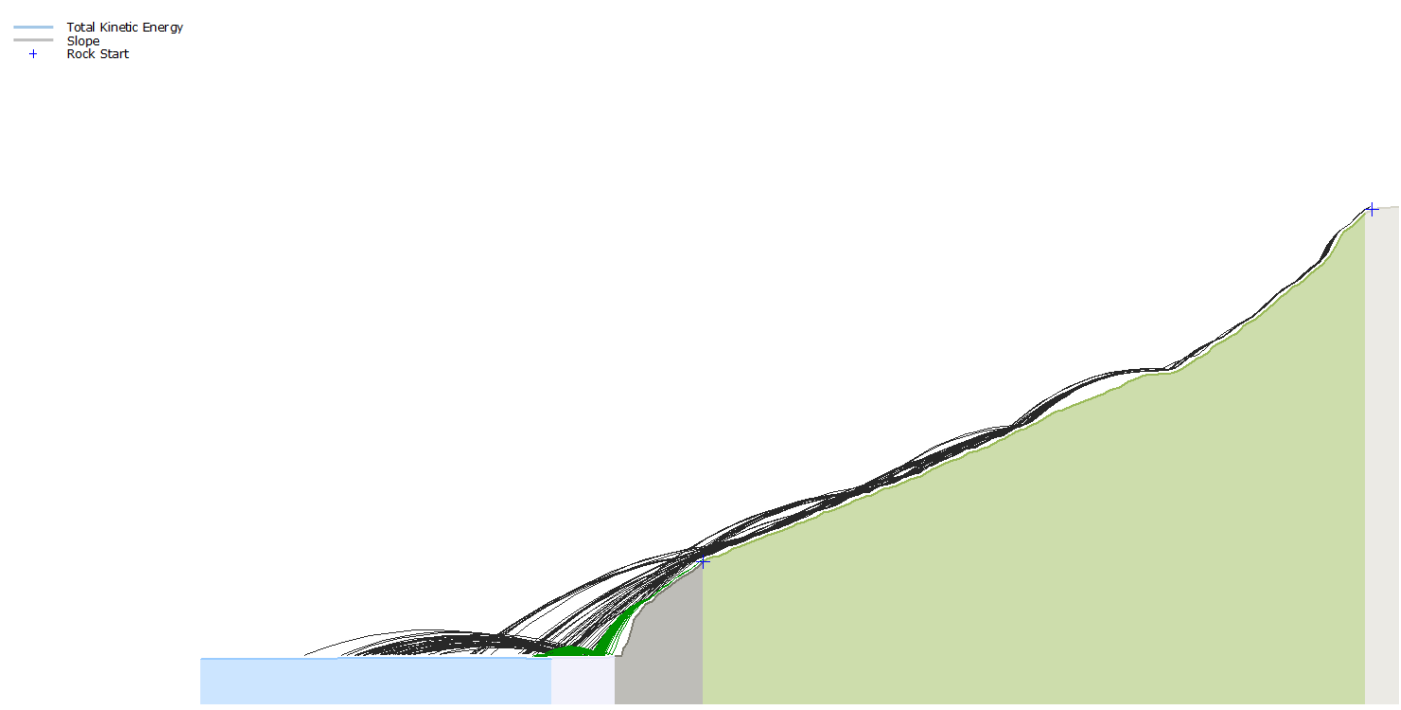

Figure 82 - Rock paths for both seeders in RocFall2 software.

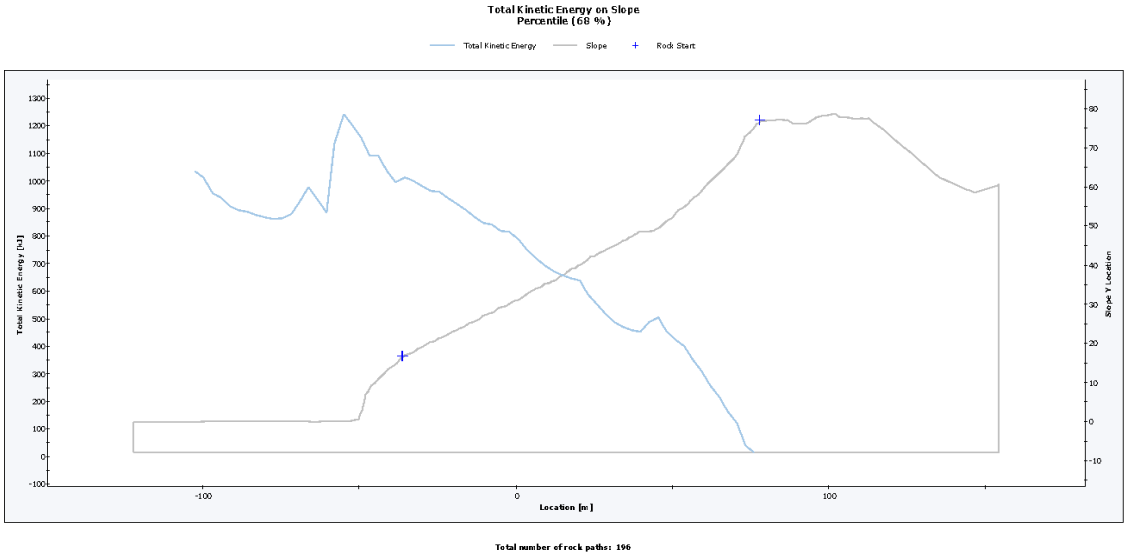

Figure 83 - Distribution of total kinetic energy along the slope in RocFall2 software.

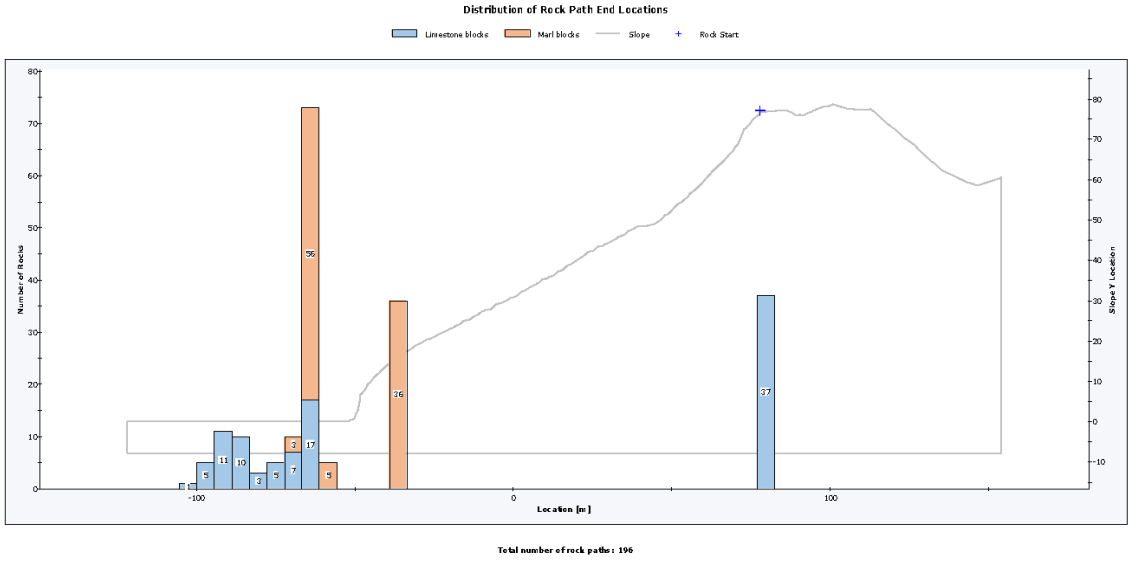

a

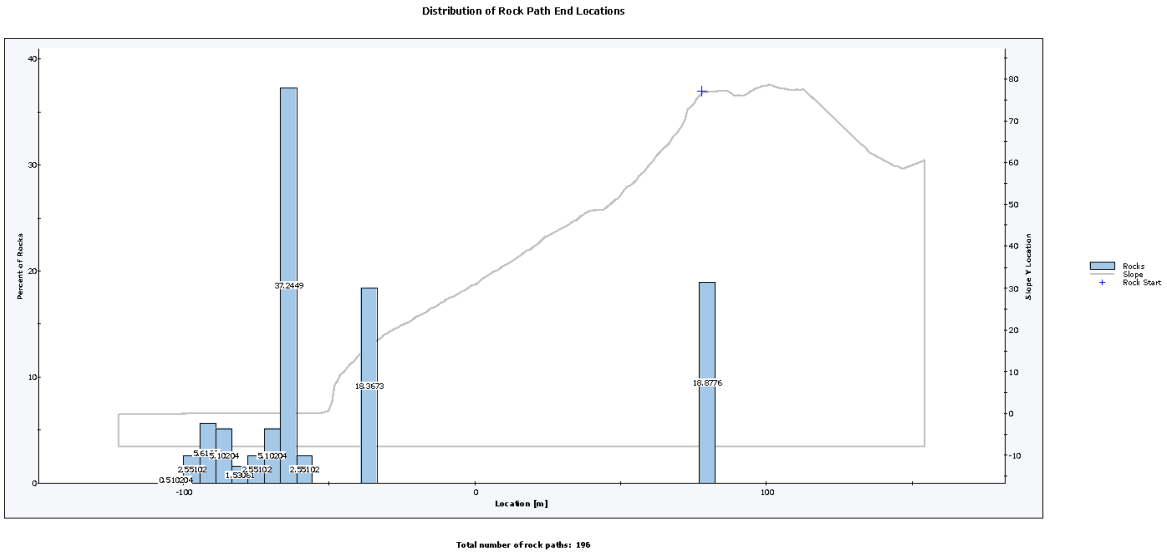

b

Figure 84 - Distribution of rock path end locations along the slope in a) number of rocks, b) percent of rocks in RocFall2 software.

4.4. Risk analyses

Rockfall hazard zones, corresponding to the accumulation areas of fallen rocks identified from the 3D Rockfall analysis (Figure 80) and including the same elements at risk along the beach area below the slope, were identified at the Brovinje site for the assessment of total rockfall risk.

The risk map with zones of different risk levels, created according to rock paths (Figure 79) and the heat map (Figure 80), was calibrated using the large number of blocks at the slope toe and in the gully along the slope identified in the field (Figure 74), as well as rockfall traces visible along the slope on the orthophoto map (Figure 66).

Total risk was categorized in five levels: very low (1), low (2), medium (3), high (4) and very high (5). Rockfall risk map in the Brovinje site is presented in Figure 85.

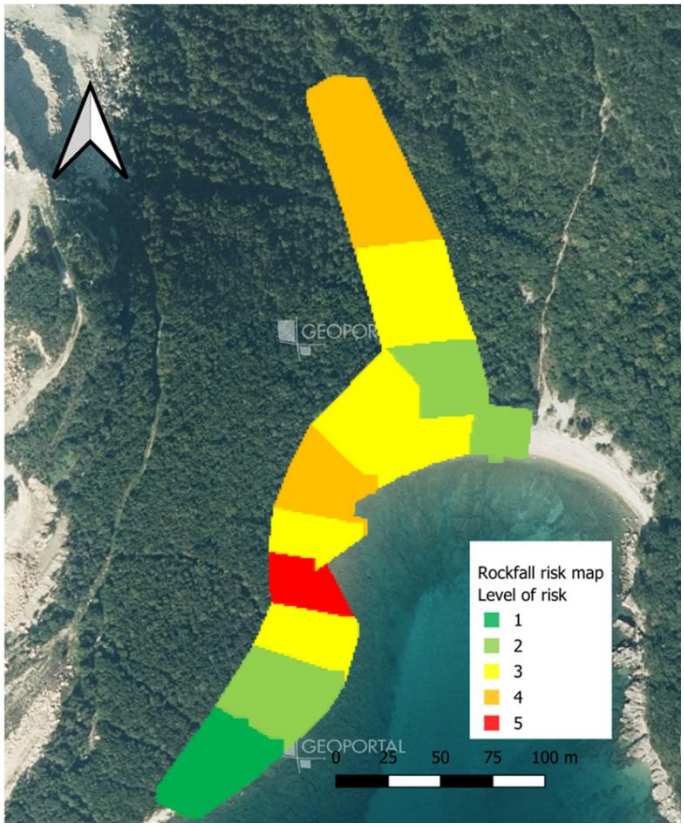

Figure 85 - Rockfall risk map for Brovinje site.

4.5. Conclusions

The slope stability analyses indicate the factor of safety at the Brovinje location, based on UAV measurements and geophysical and geotechnical laboratory investigations conducted during the RESONANCE project. The analyses show that there is no risk of global slope instability or instability at the foot of the slope.

The stability analyses considering rising sea level showed no impact on the global stability of the slope. However, rising sea level will result in stronger and higher wave impacts, which will affect the appearance of the slope, increase material weathering, and could lead to localised instabilities, including sliding and rockfall processes. It would be advisable to consider this influence in more detailed and sophisticated slope stability analyses in the future.

Field observations show that rockfalls from both the eroded marl slope and the top of the slope endanger the beach area below. 3D rockfall analyses using a point cloud model were conducted, identifying major rockfall trajectories and points at the slope toe most affected by rock impacts. The large number of blocks at the slope toe and in the gully along the slope was verified in the field and corresponds to the blocks observed on site.

A risk map with five risk levels was obtained based on the provided 3D rockfall numerical analysis. In future, protection measures could be considered and analysed.

5. References

ASTM International (2005). ASTM D4318-05: Standard test methods for liquid limit, plastic limit, and plasticity index of soils. ASTM International, West Conshohocken, PA, USA.

ASTM International (2023). ASTM D854-23: Standard test methods for specific gravity of soil solids by water pycnometer. ASTM International, West Conshohocken, PA, USA.

Basson, F.R.P. (2012). Rigid body dynamics for rock fall trajectory simulation. In: Proceedings of the 46th US Rock Mechanics/Geomechanics Symposium, Chicago, 24–27 June 2012. American Rock Mechanics Association. Paper ARMA-2012-267.

Bishop, A.W. (1955). The use of the slip circle in the stability analysis of slopes. Géotechnique, 5(1), 7–17.

CNR-ISPC (2025). Geophysical report – II semestre – PP2, pp. 11–19.

Croatian Geological Institute (CGI) (2009). Geological map of the Republic of Croatia, scale 1:300,000. Croatian Geological Institute, Department of Geology, Zagreb.

Croatian Geological Institute (2009). Geological map of the Republic of Croatia, scale 1:300,000. Croatian Geological Institute, Department of Geology, Zagreb. [Duplicate of the previous CGI reference]

Fullin, N., Duo, E., Fabbri, S., Francioni, M., Ghirotti, M. & Ciavola, P. (2023). Quantitative characterization of coastal cliff retreat and landslide processes at Portonovo–Trave cliffs (Conero, Ancona, Italy) using multi-source remote sensing data. Remote Sensing, 15, 4120. https://doi.org/10.3390/rs15174120

GRADRI (2025). Geotechnical report on the testing of marl samples, Brovinje site.

Hoek, E., Carranza-Torres, C. & Corkum, B. (2002). Hoek–Brown failure criterion – 2002 edition. In: Proceedings of the NARMS–TAC Conference, Toronto, vol. 1, pp. 267–273.

International Society for Rock Mechanics Commission on Standardization of Laboratory and Field Tests (1978). Suggested methods for the quantitative description of discontinuities in rock masses. International Journal of Rock Mechanics and Mining Sciences & Geomechanics Abstracts, 15(6), 319–368. https://doi.org/10.1016/0148-9062(78)91472-9

ISRM, Commission on Standardization of Laboratory and Field Tests (1979). Suggested methods for determining water content, porosity, density, absorption and related properties and swelling and slake durability index properties.

ISRM (1985). Suggested method for determining point load strength. International Journal of Rock Mechanics and Mining Sciences & Geomechanics Abstracts, 22(2), 51–60. Pergamon Press, Great Britain.

Mammoliti, E., Fronzi, D., Cambi, C., Mirabella, F., Cardellini, C., Patacchiola, E., Tazioli, A., Caliro, S. & Valigi, D. (2022). A holistic approach to study groundwater–surface water modifications induced by strong earthquakes: The case of Campiano catchment (Central Italy). Hydrology, 9, 97.

Mandaglio, M.C. (2024). Geomechanical characterization of the rock mass along a deep vertical borehole. Geotechnics, 4(1), 209–228. https://doi.org/10.3390/geotechnics4010011

Marinos, P. & Hoek, E. (2000). GSI: a geologically friendly tool for rock mass strength estimation. In: Proceedings of GeoEng2000 International Conference on Geotechnical and Geological Engineering, Melbourne, 19–24 November 2000, pp. 1422–1446.

Montanari, A., Mainiero, M., Coccioni, R. & Pignocchi, G. (2016). Catastrophic landslide of Medieval Portonovo (Ancona, Italy). Geological Society of America Bulletin, 128, 1660–1678.

Velić, I. & Vlahović, I. (2009). Interpreter of geological maps, 1:300,000. Croatian Geological Institute, Zagreb, 147 pp.